



First-Principles Studies of Novel Two-Dimensional Dirac Materials

First-Principles Studies van Nieuwe Tweedimensionale Dirac Materialen

Proefschrift voorgelegd tot het behalen van de graad van doctor in de Wetenschappen aan
de Universiteit Antwerpen te verdedigen door

Linyang Li

Promotor: Prof. Dr. François M. Peeters

Departement Fysica, Faculteit Wetenschappen, Universiteit Antwerpen

Antwerpen, België

Juni, 2019

Members of the Jury:

Chairman

Prof. Dr. Johan Verbeeck, University of Antwerp, Belgium

Supervisor

Prof. Dr. François Peeters, University of Antwerp, Belgium

Members

Prof. Dr. Dirk Lamoen, University of Antwerp, Belgium

Prof. Dr. Bart Partoens, University of Antwerp, Belgium

Prof. Dr. Paul Kelly, University of Twente, Netherlands

Prof. Dr. Hasan Sahin, Izmir Institute of Technology, Turkey

Contact Information:

Linyang Li

G.U. 315

Campus Groenenborger, Groenenborgerlaan 171, 2020 Antwerp, Belgium

linyang.li@uantwerpen.be

Research Units:



Funding Agency:



Fonds Wetenschappelijk Onderzoek
Vlaanderen
Opening new horizons

I dedicate this thesis to my loving mother, Lingzhi Sun.

Acknowledgements

Time flies and I will face a new important moment in my life. Here, I want to thank everyone who has helped me.

Firstly, I would like to express my utmost gratitude to Professor François Peeters for offering me the position to work in the condensed matter theory (CMT) group at the University of Antwerp. He is the greatest professor and it's my honor to be his PhD student. I truly appreciate both his academical and financial support during my PhD study.

Secondly, I would like to thank my collaborator, Dr. Xiangru Kong from Peking University. We worked together to solve many scientific research problems. By cooperating with him, I recognize the importance of cooperation in scientific research, which will inflect my future research.

Thirdly, I would like to thank Dr. Lingfeng Zhang, Dr. Yierpan Aierken, Dr. Longlong Li, Dr. Weiyang Wang, and Dr. Ortwin Leenaerts for their guidance in my study and life. When I just arrived in Antwerp, I faced a completely new environment and I came across many difficulties. They helped and encouraged me in many aspects. I have learned a lot from them.

Finally, I would also like to thank my parents for their support during my PhD study.

Table of contents

List of abbreviations	xi
1 2D Dirac Materials	1
1.1 Overview of Graphene	1
1.2 2D Carbon-Based Materials	3
1.2.1 2D Carbon Allotropes	3
1.2.2 2D Carbon-Nitrogen Structures	5
1.3 2D Topological Insulators	8
1.4 2D Chern Insulators	11
1.5 Outline of the Thesis	12
2 Computational Methods	15
2.1 Density Functional Theory	15
2.1.1 Hohenberg-Kohn Theorems	15
2.1.2 Kohn-Sham Equation	17
2.1.3 Exchange-Correlation Functional	18
2.1.4 Software Packages	19
2.2 Tight-Binding Theory	19
2.3 Spin-Orbit Coupling	21
2.4 Wilson Loop Method and Topological Invariant (Z_2)/Chern Number (C)	23
3 C-Based Material: $H_{4,4,4}$-Graphyne	27
3.1 Introduction	27
3.2 Calculation Method	29
3.3 Results and Discussions	30
3.3.1 Structure	30

3.3.2	Energy and Stability	31
3.3.3	Band Structure	33
3.3.4	Moiré Superstructure	38
3.4	Conclusion	39
4	C-Based Materials: Dumbbell C₄N	41
4.1	Introduction	41
4.2	Calculation Method	43
4.3	Results and Discussions	43
4.3.1	Geometrical Structure	43
4.3.2	Energy and Stability	45
4.3.3	Band Structure	47
4.3.4	TB Model	51
4.3.5	Synthesis and Application	52
4.4	Conclusion	53
5	Bi-Based Topological Insulators: GaBi-X₂ (X = I, Br, Cl)	55
5.1	Introduction	55
5.2	Calculation Method	57
5.3	Results and Discussion	58
5.3.1	Geometrical Structure	58
5.3.2	Energy and Stability	60
5.3.3	Electronic Band Structure	61
5.3.4	Topologically Nontrivial Property	62
5.4	Conclusion	69
6	Bi-Based Topological Insulators: Bi Bilayers with 4,6,8-Atom Rings	71
6.1	Introduction	71
6.2	Computational Method	73
6.3	Results and Discussions	74
6.3.1	Structure and Stability	74
6.3.2	Electronic Band Structure	77
6.3.3	Topological Property	79
6.3.4	Structural Tunability	85
6.4	Conclusions	87

7	Y-Based Chern Insulator: 1T-YN₂	91
7.1	Introduction	91
7.2	Computational Method	94
7.3	Results	95
7.4	Possibility of Experimental Realization	101
7.5	Discussions	107
7.6	Conclusion	109
8	Summary and Outlook	111
8.1	Summary	111
8.2	Outlook	112
9	Samenvatting	115
	Bibliography	117
	Appendix A Curriculum Vitae	149

List of abbreviations

0D zero-dimensional

1D one-dimensional

2D two-dimensional

3D three-dimensional

ARPES angle-resolved photoemission spectroscopy

C₂N-h2D crystal C₂N holey 2D crystal

C₃N 2D Polyaniline

C₃N₃ triazine

C₆N₇ tri-s-triazine/heptazine

CBM conduction band minimum

DFT density functional theory

FBZ first Brillouin zone

g-C₃N₄ graphitic carbon nitride

GGA generalized gradient approximation

HAB hexaaminobenzene trihydrochloride

HF Hartree-Fock

HSE Heyd-Scuseria-Ernzerhof

LDA	local density approximation
MAE	mean absolute error
OER	oxygen evolution reaction
PAW	projected augmented-wave
PDOS	projected density of electronic states
QAH	quantum anomalous Hall
QH	quantum Hall
QSH	quantum spin Hall
QW	quantum well
SOC	spin-orbit coupling
STM	scanning tunneling microscopy
STS	scanning tunneling spectroscopy
TMDs	Transition metal dichalcogenides
TR	time-reversal
VASP	Vienna <i>ab initio</i> Simulation Package
VBM	valence band minimum
vdW	van der Waals
XC	exchange-correlation

Chapter 1

2D Dirac Materials

1.1 Overview of Graphene

Graphene is a monolayer material, which is composed of carbon atoms. As a result of its ($1s^2 2s^2 2p^2$) electronic configuration, the carbon atom can form a number of different hybrid orbitals, sp , sp^2 , and sp^3 , leading to many different kinds of carbon materials with different chemical bond characteristics. Among those, graphene is the most famous material in the past ten years. As shown in Fig. 1.1 [1], graphene is a 2D material composed of sp^2 hybrid carbon atoms. Due to the sp^2 hybridization, the chemical bonds (σ) form a very strong framework, and as a result, graphene exhibits excellent mechanical strength. The p_z atomic orbitals are directed perpendicular to the graphene plane giving rise to a linear relationship between energy and momentum, which results in the Dirac cone band structure. This makes graphene to have excellent electrical conductivity.

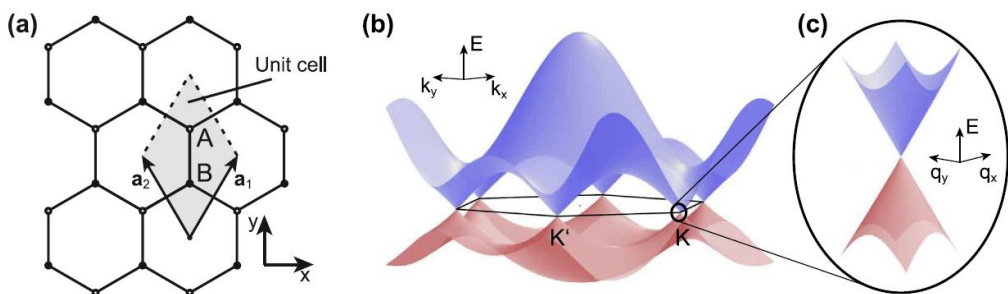


Fig. 1.1 (a) Graphene honeycomb lattice composed of A and B hexagonal Bravais sublattices. (b) Band structure of graphene where CBM and VBM touch each other only at the K and K' points. (c) Approximately linear dispersion around the K and K' points. Image source: Ref. [1]

The successful isolation of a single layer of graphene from graphite was achieved in 2004 by A. K. Geim and K. S. Novoselov at Manchester University using a mechanical exfoliation method [2]. Graphene can become visible in an optical microscope when it is placed on top of a Si wafer with a carefully chosen thickness of SiO₂ [3]. The synthesis of graphene was a great achievement. The excellent properties graphene exhibited excited researchers.

To study its properties, we can start with analyzing its structure. Graphene is a one-atom-thick single crystal, which is composed of carbon atoms. Each carbon atom has the same environment, three nearest neighbors and the two carbon atoms are chemically bonded. The type of chemical bond belongs to covalent bond and graphene has a uniform bond length of 1.42 Å. Due to perfect sp^2 -hybrid carbon atoms, bond angles of 120° are also uniform. All carbon atoms are limited in a hexagonal honeycomb lattice, see Fig. 1.1(a). The gray area is the unit cell of graphene containing two carbon atoms. Because of the special structure, Graphene shows excellent mechanical properties. Graphene has a Young modulus of 1 terapascals and an intrinsic strength of 130 gigapascals [4]. The p_z atomic orbitals in this hexagonal honeycomb lattice makes graphene a semimetal with conduction band minimum (CBM) and valence band maximum (VBM) that touch each other at the K and K' points forming a Dirac point as shown in Fig. 1.1(b) and (c). The energy-momentum dispersion is approximately linear around the K and K' points. The charge carriers can be characterized by massless Dirac fermions that travel at a constant speed of 10^6 m/s (Fermi velocity) and they are governed by the relativistic equation [5]. Due to the high Fermi velocity, graphene has the potential to be applied in high speed electronic nanodevices. Besides, graphene can exhibit many novel physical effects in the presence of external electric field [3] and magnetic field [6].

In addition, graphene exhibits extraordinary thermal conductivity properties and transport properties. Based on the measurements that monolayer graphene on Si/SiO₂ substrate, graphene shows an extraordinary high room temperature thermal conductivity of up to $5.30(0.48) \times 10^3$ W/mK [7]. High carrier mobility is another exciting feature of graphene, which is important for applications of device. The ultraclean suspended graphene has been reported to have a carrier mobility 120,000 cm²/Vs at 240 K, which is higher than that of any known semiconductor [8]. The above properties of graphene make it very promising to be applied in many fields.

1.2 2D Carbon-Based Materials

1.2.1 2D Carbon Allotropes

In nature, there are two major existing carbon allotropes, diamond and graphite. Diamond is composed of sp^3 -hybridized carbon atoms while graphite is composed of sp^2 -hybridized carbon atoms [9]. The discovery of zero-dimensional (0D) fullerenes [10], one-dimensional (1D) nanotubes [11], and 2D graphene [2] greatly expanded the family of carbon materials, as shown in Fig. 1.2 [12]. Those new carbon materials are composed of sp^2 -hybridized carbon atoms. In theory, thousands of carbon structures can be constructed by using different sp^3 -, sp^2 -, and sp -hybridized carbon atoms due to the versatile flexibility of carbon atoms [13–15]. Take sp^2 -hybridized carbon atoms as an example, they can form a number of rings. Graphyne, which is composed of sp - and sp^2 -hybridized carbon atoms, has been given its own name according to specific rules related to its structure [16]. This planar and monolayer material contains triple bonds of carbon and sp^2 -hybridized carbon atoms. Li *et al.* realized graphdiyne films [17], which contains two connected triple bonds between repeating patterns of carbon hexagons, as shown in Fig. 1.2. The networks of graphdiyne and graphyne are contain sp - and sp^2 -hybridized carbon atoms. Graphdiyne is composed of two connected triple bonds of carbon while γ -graphyne is composed of one triple bond. The special carbon networks lead to the graphyne family with uniformly distributed pores, which can be applied for gas separation and energy storage. Some have been realized experimentally.

Among the graphyne family, there are four typical structures, see Fig. 1.3 [18]. Only γ -graphyne exhibits semiconductor characteristic while α -graphyne/ β -graphyne/6,6,12-graphyne shows a Dirac band structure [19]. Although different structures lead to different single bond lengths of carbon, their triple bond lengths of carbon are almost the same, see Table 1.1 [18]. In recent years, there are many theoretical researches on γ -graphyne. With respect to band structure, the electronic structure of γ -graphyne was calculated by density functional theory (DFT), and the band gap of 0.47/2.23 eV depending on different calculation methods, as given in Ref. [20]. The adsorption of gas molecules on γ -graphyne was studied and γ -graphyne was predicted to transform from a semiconductor into a semimetal or metal when particular gas molecules are absorbed [21]. Ruiz-Puigdollers *et al.* showed the tunable band structure of γ -graphyne by using N- and B-doping [22]. Besides its band structure, the chemical properties and energy for applications were studied.

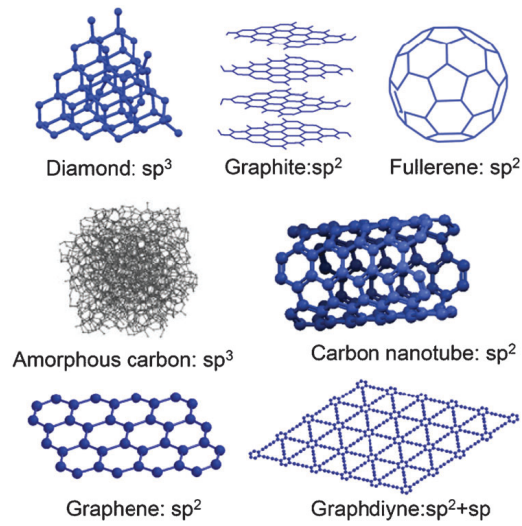


Fig. 1.2 Naturally existing and man-made carbon allotropes. Image source: Ref. [12]

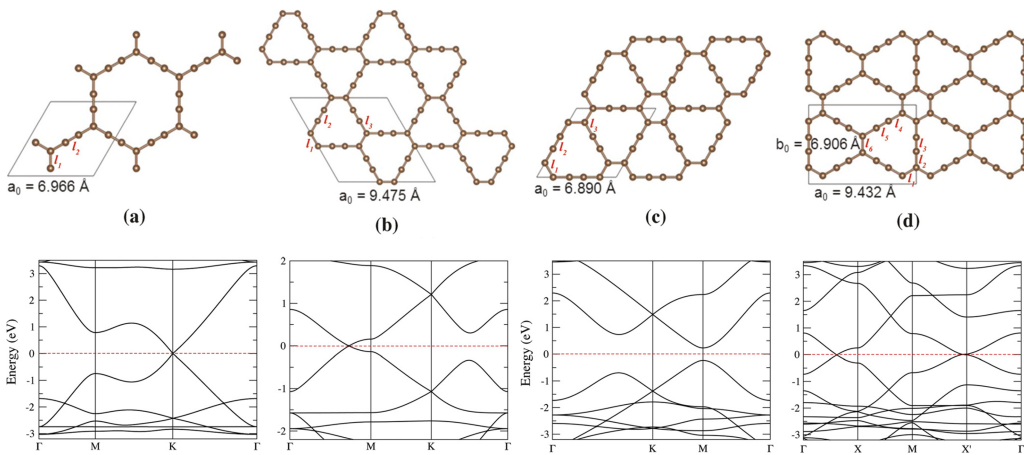


Fig. 1.3 Atomic structure and band structure of α (a)/ β (b)/ γ (c)/6,6,12(d)-graphyne. Image source: Ref. [18]

Table 1.1 Carbon triple bond lengths of the $\alpha/\beta/\gamma/6,6,12$ -graphyne. Date source: Ref. [18]

Graphyne	Bond Length
α -graphyne	$l_2 = 1.230 \text{ \AA}$
β -graphyne	$l_2 = 1.232 \text{ \AA}$
γ -graphyne	$l_2 = 1.232 \text{ \AA}$
6,6,12-graphyne	$l_3 = 1.224 \text{ \AA}$ $l_5 = 1.227 \text{ \AA}$

Although the theoretical and computational research of γ -graphyne is inspiring, the synthesis of γ -graphyne was only recently achieved. It was synthesized by a chemical method, as outlined in Fig. 1.4 [23]. The experimental results including composition, lattice constant, and band gap (2.58 eV) of the as-prepared sample are in good agreement with calculated results [20].

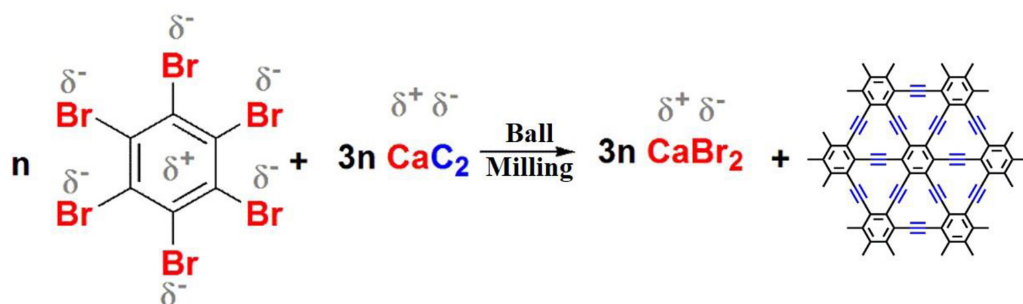


Fig. 1.4 Proposed reaction pathway for the preparation of γ -graphyne by mechanochemical route. Image source: Ref. [23]

1.2.2 2D Carbon-Nitrogen Structures

The history of carbon nitride (C_3N_4) polymers and their precursors could be traced back to 1834 [24, 25]. The application of graphitic carbon nitride (g- C_3N_4) in heterogeneous catalysis started around 2006 [26]. In 2009, Wang *et al.* first found that g- C_3N_4 is a metal-free conjugated semiconductor photocatalyst for H_2 evolution [27, 28]. There are two basic tectonic units to establish allotropes of g- C_3N_4 , which are triazine (C_3N_3) and tri-s-triazine/heptazine (C_6N_7) rings (Fig. 1.5 [29]) [30, 31]. From the view point of the porous structure, there are two aspects that can affect the energetic stability: the size of the pores and the chemical environment of the N atom. Among all phases, tri-s-triazine-based g- C_3N_4 was energetically favored and was the most stable phase of C_3N_4 [32], which

was in good agreement with DFT calculations [33]. In experiment, many newer 2D carbon-nitrogen materials were proposed, such as 2D crystal "C₂N holey 2D crystal" (C₂N-*h*2D crystal) [34] and 2D polyaniline (C₃N) [35]. Since the structure C₃N is the basis of our research, we will introduce the experiment on 2D C₃N.

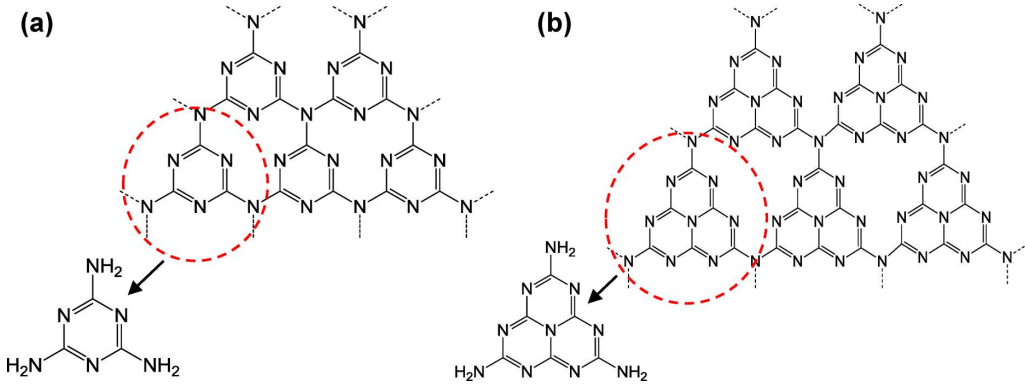


Fig. 1.5 (a) Triazine and (b) tri-s-triazine (heptazine) structures of g-C₃N₄. Image source: Ref. [29]

The synthesis process of 2D C₃N is shown in Fig. 1.6 [35]. The transformation of HAB crystals into a 2D layered polyaniline structure should involve the release of ammonium chloride (NH₄Cl) and ammonia (NH₃) via a concerted mechanism. Actually, 2D C₃N is a graphene-like structure when viewed from the top and a monolayer structure as seen from side. In some special lattice points, the carbon atoms are replaced by nitrogen atoms.

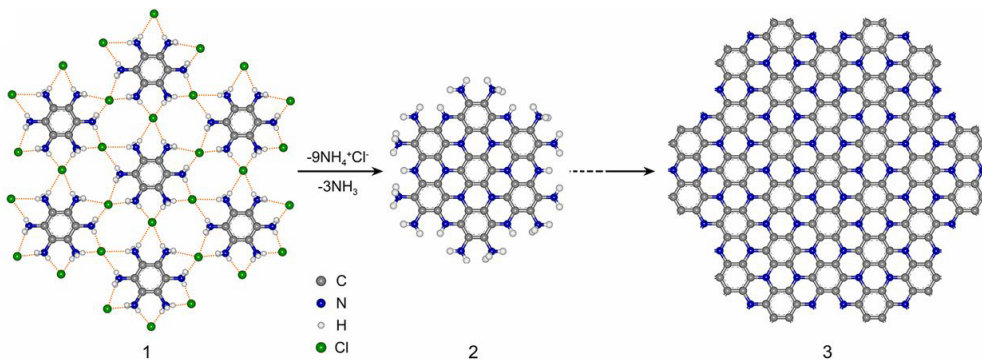


Fig. 1.6 Schematic representation of 2D polyaniline (PANI) formation. (A) Single-crystal packing structure of HAB (structure 1); structure of 2D polyaniline unit with edge groups (C₃NH, structure 2), and the spontaneous transformation of HAB crystal unit into the 2D polyaniline structure (structure 3). Image source: Ref. [35]

To analyze the experimental results, the authors [35] performed first-principles calculations. We focus on its geometrical structure and its band structure. The calculated lattice constant is 4.75 Å (Fig. 1.7(D) [35]), which is in good agreement with experimental result (Fig. 1.7(A)). The band structure along the symmetry points in the first BZ is shown in Fig. 1.7(E), and an indirect band gap at the Fermi level is seen. From the projected density of states (PDOS) (Fig. 1.7(F)), the VBM and CBM both come from the carbon and nitrogen p_z orbitals. Obviously, there is a Dirac point below the Fermi level, which is the motivation of our research.

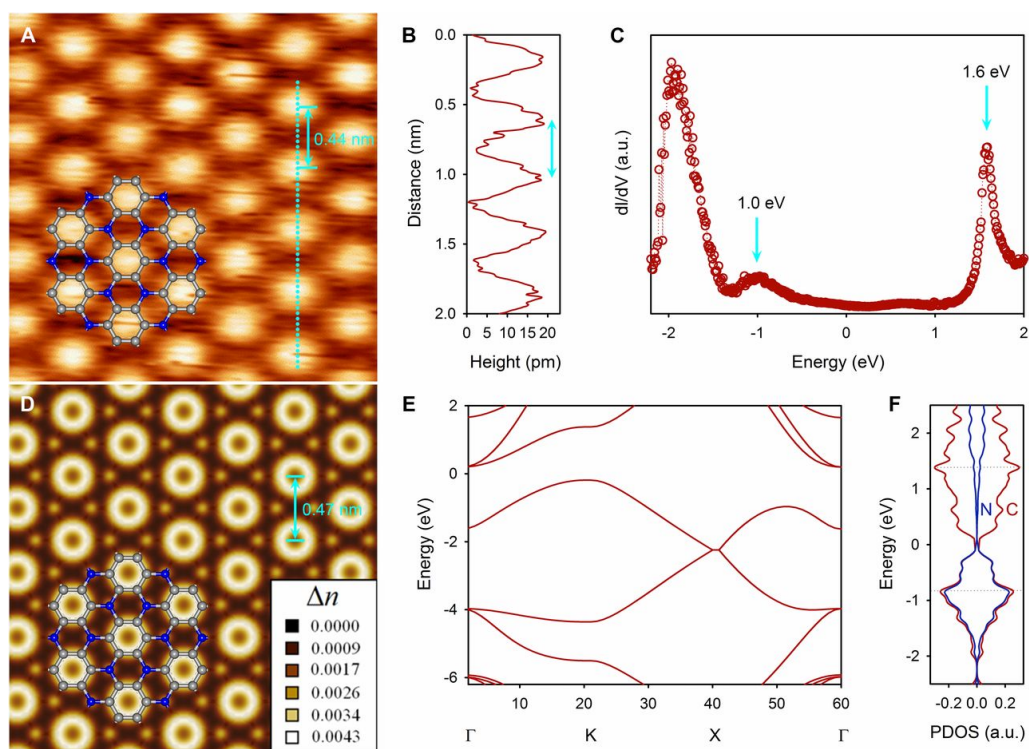


Fig. 1.7 STM and theoretical studies of the 2D polyaniline structure. (A) STM image of a 2D polyaniline framework. Inset structure represents C_3N repeating unit with carbon atom (gray ball) and nitrogen atom (blue ball). (B) Topographic height profile along the cyan dot line marked in (A). (C) Differential conductance (dI/dV) spectrum of a 2D polyaniline framework. (D) Simulated STM image with superimposed structure of C_3N repeating unit. (E) Electronic band structure. (F) Projected density of electronic states (PDOS) of the carbon (dark red) and nitrogen (dark blue) atoms. Image source: Ref. [35]

1.3 2D Topological Insulators

The Hall effect is the result of a voltage difference (the Hall voltage) across an electrical conductor, transverse to an electric current in the conductor and to an applied magnetic field perpendicular to the current. It was discovered by Edwin Hall in 1879 [36]. The effect can be measured by the Hall resistance. About a century later, the Hall resistance showed a ladder-like dependence on the magnetic field in two-dimensional electron systems (Fig. 1.8 [37]), which is called the quantum Hall (QH) effect [37]. The QH was realized in strong magnetic fields and low temperatures. The QH effect was first discovered by K. von Klitzing who received the Nobel prize in physics for it in 1985. In this effect, the electrons in the conductor perform periodic circular motion and therefore do not contribute to electric conduction. The edge electrons will be influenced by the edge where electrons perform semicircular motion onward. In this process, there are no collisions with energy loss. Here, the Hall conductance depends only on the fundamental physical constants e and h , and is entirely independent on the materials' properties, and the geometry of the example, such as, length and width.

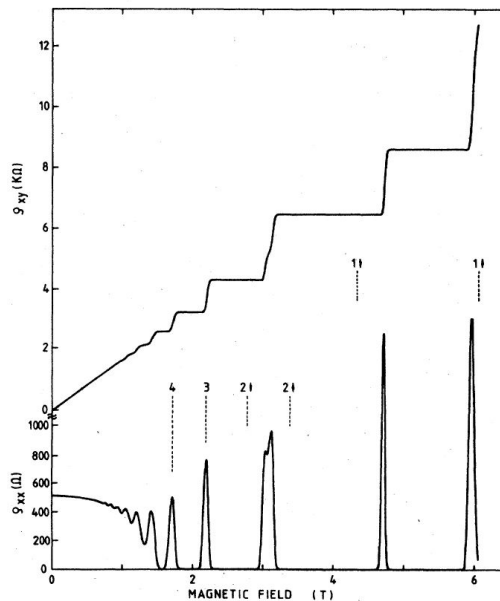


Fig. 1.8 Experimental curves for the Hall resistance $R_H = \rho_{xy}$ and the resistivity $\rho_{xx} \sim R_x$ of a heterostructure as a function of the magnetic field at a fixed carrier density corresponding to a gate voltage $V_g = 0$ V. The temperature is about 8 mK. Image source: Ref. [37]

Due to the explicitly breaking of the time-reversal (TR) symmetry, the QH states belong to a topological class. In contrast to breaking TR symmetry, there is a new topological class which is invariant under TR. In recent years, this new topological class of materials has been not only predicted in theory, but also observed in experiment [38–41]. At the beginning of this class, some important concepts of these new quantum states were proposed [42–46]. In 2D materials, 2D topological insulator/quantum spin Hall (QSH) state was successfully proposed by Kane *et al.* [47]/Bernevig *et al.* [48]. After these theoretical concepts were successfully developed in 2D topological insulators, researchers applied them to 3D topological insulators [49–53]. By a Z_2 topological order parameter, all insulators in nature can be divided into two categories. The $Z_2 = 1$ corresponds to a topological nontrivial state while the $Z_2 = 0$ corresponds to the topological trivial state. With respect to band structure, the topologically nontrivial state includes two important aspects, a full insulating gap in the bulk (2D/3D) and gapless edge or surface states consisting of an odd number of Dirac fermions (1D/2D). Although the topic of our thesis is 2D materials, some theoretical and experimental methods of 3D topological insulators can also be applied into 2D topological insulators. Next, we will introduce the history of the two kinds of topological materials.

The 2D topological insulator material was first theoretically predicted in 2006 [54] and experimentally observed [55, 56] in HgTe/CdTe quantum wells (QWs). Whether the topologically nontrivial state can be realized depends on the thickness of the QWs. In the topologically nontrivial states, the opposite spins propagate in opposite directions and form a pair of edge states, see Fig. 1.9 [57]. The 2D topological insulator is synonymously called the QSH insulator. However, the operating temperature of QWs is quite low due to the small bulk gap arising from weak SOC. To solve this question, hundreds of QSH insulators with a large nontrivial gap have been found from DFT calculations, and many of them were predicted to result in the QSH effect at room temperature. In 2018, QSH effect was realized experimentally in a monolayer 1T'-WTe₂ at the temperature of 100 K [58], which is a breakthrough for QSH effect at room temperature. Before the experimental work, some theoretical works have shown that the monolayer 1T'-WTe₂ is a 2D topological insulator by DFT calculations [59].

For the 3D topological insulator, the heavy elements contributions are very important. In theory, the semiconducting alloys Bi_{1-x}Sb_x were predicted as 3D topological insulators by calculating Z_2 invariants [49]. Besides Bi and Sb elements, Te and Se elements also play an important role for 3D topological insulators. In theory, Bi₂Te₃, Sb₂Te₃, and Bi₂Se₃

[60, 61] compounds were predicted with a large bulk gap and a gapless metal surface state with a single Dirac cone. In experiment, Angle-resolved photoemission spectroscopy (ARPES) measurement is a powerful tool to see the edge states clearly. By ARPES measurements, the above surface states were fully confirmed in experiments [62, 63, 60]. These theoretical and experimental works greatly excited the interest of researchers in the field of topological insulators [38, 64, 65, 39–41]. Beyond the above topological materials mentioned, more new materials have been predicted to be topological insulators [66–69], and some of them have been experimentally observed recently [70, 71].

Without a doubt, the discovery of topological insulators has a great impact on condensed matter physics [72] and many important prizes have given the researchers in this field. The first discovery of the QSH effect in QWs was ranked as one of the top ten breakthroughs by Science Magazine in year 2007. Three scientists, David J. Thouless, F. Duncan M. Haldane and J. Michael Kosterlitz, received the Nobel prize in physics in 2016 due to their contributions to topological theory.

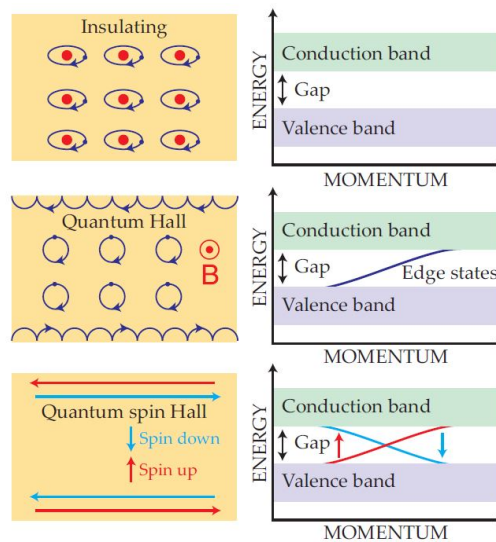


Fig. 1.9 Electronic states have different topologies. In insulators, the outer electrons are pinned by their atoms. A gap is present at all values of momentum. In the quantum Hall regime, a magnetic field pins the outer electrons and opens a gap. The gap is crossed by edge states, which carry current. In the quantum spin Hall regime, a bulk gap is always present. The edge states that cross the gap carry counter propagating currents of spin-up and spin-down electrons. The three states are topologically distinct. No perturbation can transform one state into another unless it's strong enough to collapse and reopen the bulk energy gap. Image source: Ref. [57]

1.4 2D Chern Insulators

In the presence of TR symmetry, insulators can be classified into Z_2 topological insulators and topologically trivial insulators, as described above. Next, we will discuss the case of insulators with broken TR symmetry. Now their topological nontrivial states are usually characterized by the first Chern number C [73, 74]. It is a topologically trivial insulator for $C = 0$, while it is a topologically nontrivial insulator [75] for a nonzero integer C [42], which can realize the quantum anomalous Hall (QAH) effect [75, 42]. The Chern number corresponds to the number of gapless chiral edge states inside the bulk band gap [76].

Before the year 2004, there was only little progress on the theory of QAH effect in materials [77]. The successful synthesis of graphene started the research of 2D materials. However, two independent theoretical works in 2010 changed the situation, and interest was revived by the successful realization of the QAH effect based on magnetic 3D topological insulator thin films [78] and graphene adsorbing magnetic atoms [79]. Here, we can take 3D TI thin films, $(\text{Bi, Sb})_2\text{Se}_3$, as an example [78, 40, 77, 80, 81]. For a 2D topological insulator, its gapless edge states can exist in 1D nanoribbon. Similar to a 2D topological insulator, gapless edge states of a 3D topological insulator can exist on the surface of 3D topological insulator, 2D thin films, where the spins are locked with the momenta preserving the TR invariance [40, 77]. When the film thickness is decreased, the interaction between top and bottom surface states gives rise to in a band gap at the Dirac cone of the surface states, forming a 2D trivial insulator [78], as shown in Fig. 1.10 [78], corresponding to a four-band system which is originally in the topologically trivial phase without band inversion. By magnetic doping, an exchange field, such as a spontaneous ferromagnetic order, can be formed [78]. The exchange field removes the spin-degeneracy, leading to spin splitting. When the exchange field is strong enough, the band inversion between the blue solid line and the red dashed line point will appear at the Γ point. This process is shown in Fig. 1.10 (A). The strong SOC reopens a band gap to induce a topological phase with a Chern number of $C = 1$ [78]. The same situation can be applied in a four-band system which is originally in the topologically nontrivial phase with band inversion, as shown in Fig. 1.10 (B) [78]. In this case, band inversion occurs. The exchange field can increase the band inversion between the blue solid line and the red dashed line at the Γ point, while the exchange field can release the band inversion between the blue dashed line and the red solid line at the Γ point, as shown in Fig. 1.10 (B). The strong SOC opens a band gap to induce a topological phase. Such a mechanism

is general for the 3D topological insulator thin-films with ferromagnetic order. This theoretical prediction was later experimentally confirmed [82–88].

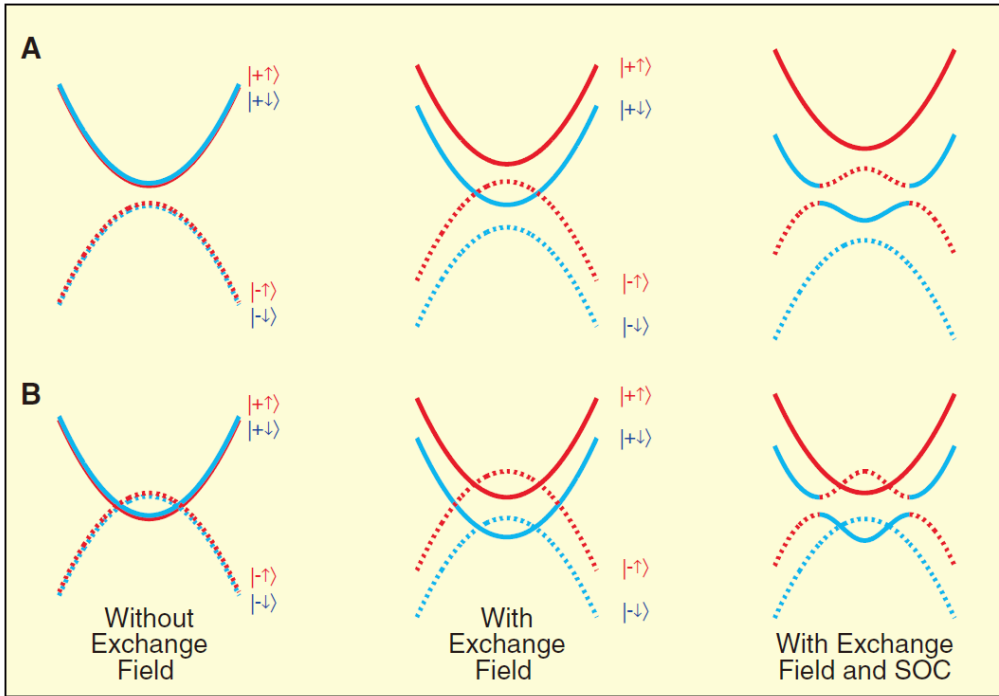


Fig. 1.10 Evolution of the subband structure upon increasing the exchange field. The solid lines denote the subbands that have even parity at Γ point, and dashed lines denote subbands with odd parity at Γ point. The blue color denotes the spin down electrons; red, spin up electrons. (A) The initial subbands are not inverted. When the exchange field is strong enough, a pair of inverted subbands appears (red dashed line and blue solid line). (B) The initial subbands are already inverted. The exchange field releases the band inversion in one pair of subbands (red solid line and blue dashed line) and increase the band inversion in the other pair (red dashed line and blue solid line). Image source: Ref. [78]

1.5 Outline of the Thesis

The thesis is organized as follows.

As discussed above, there are three kinds of 2D materials which are related to the research presented in this thesis. In **Chapter 1**, we present an introduction of these 2D materials, including their theoretical and experimental basis. In **Chapter 2**, we introduce the theory of DFT and the calculations methodology used in the thesis.

In **Chapter 3** and **Chapter 4**, we show our results of C-based Dirac Materials. In these new C-based materials, SOC effect can be neglected, and we stress their high Fermi velocity.

In **Chapter 5** and **Chapter 6**, we show our results of Bi-based Dirac Materials. In these new Bi-based materials, SOC effect plays an important role, and a large nontrivial band gap can be opened at the Dirac point.

In **Chapter 7**, we show our results of Y-based Dirac materials. In this Y-based materials, not only a large nontrivial band gap can be opened at the Dirac point, but also ferromagnetic systems can be realized ferromagnetic systems.

The content of **Chapter 3**, **4**, **5**, **6**, and **7** are based on my research works during my PhD. In **Chapter 8**, I present a summary of the thesis and an outlook for future research.

Chapter 2

Computational Methods

In this chapter, I will introduce relevant theoretical models, approximations and their implementations in commonly used software packages. Density functional theory (DFT) is one of the most widely used quantum mechanical methods to calculate the properties of materials. This method allows total 10^2 simulated atoms with present computer power. Another important calculation method is the tight-binding (TB) method, whose order of magnitude can reach 10^4 or higher. Our following researches are based on those two methods.

2.1 Density Functional Theory

DFT is based on the Hohenberg-Kohn theorems [89] and Kohn-Sham equations [90]. In the following, We will briefly discuss their derivation processes.

2.1.1 Hohenberg-Kohn Theorems

Materials are made from atoms, while atoms contain electrons and nuclei. In quantum mechanics, the nuclei can be treated as classical particles. The electron behaviour is

described by Schrödinger equation. It can be written as follows:¹

$$\begin{aligned}
& \hat{H}\psi_{\alpha}(\vec{r}_1\sigma_1, \dots, \vec{r}_N\sigma_N) \\
&= \left[-\frac{1}{2} \sum_{i=1}^N \nabla_i^2 + \sum_{i=1}^N v(\vec{r}_i) + \frac{1}{2} \sum_{i=1}^N \sum_{j \neq i}^N \frac{1}{|\vec{r}_i - \vec{r}_j|} \right] \psi_{\alpha}(\vec{r}_1\sigma_1, \dots, \vec{r}_N\sigma_N) \\
&= (\hat{T} + \hat{V}_{ext} + \hat{V}_{ee}) \psi_{\alpha}(\vec{r}_1\sigma_1, \dots, \vec{r}_N\sigma_N) \\
&= E_{\alpha} \psi_{\alpha}(\vec{r}_1\sigma_1, \dots, \vec{r}_N\sigma_N).
\end{aligned} \tag{2.1}$$

In the above equation, \hat{H} is the total Hamiltonian, which is equal to three parts: \hat{T} (kinetic energy), \hat{V}_{ext} (interaction between electrons and nuclei), and \hat{V}_{ee} (interaction between electrons). We used the Born–Oppenheimer approximation [91]. Corresponding to the above three parts, the first two terms sum overall N electrons, and the last one sums over all pairs of N electrons. \vec{r} is the electron position, and σ is the z-component of the electron spin. ψ is the N -electron wave function, and α is the complete set of N -electron quantum numbers. E is the total energy. Next, we focus on E .

By the constrained search algorithm [92], the ground-state energy E can be expressed as:

$$E = \min_{\psi} \langle \psi | \hat{H} | \psi \rangle. \tag{2.2}$$

Next we take two steps of minimization. For the first step, We can construct the universal functional $F[n(\vec{r})]$:

$$\min_{\psi \rightarrow n} \langle \psi | \hat{T} + \hat{V}_{ee} | \psi \rangle = \langle \psi_n^{min} | \hat{T} + \hat{V}_{ee} | \psi_n^{min} \rangle = F[n(\vec{r})]. \tag{2.3}$$

For the second step, we can obtain

$$E = \min_n \left\{ F[n(\vec{r})] + \int dr^3 v(\vec{r})n(\vec{r}) \right\}, \tag{2.4}$$

where $v(\vec{r})$ is kept fixed during the minimization. The resulting density is the ground-state density that gives the ground state energy. This is known as the density variational principle, which is also the main idea of the Hohenberg-Kohn theorems, which are:

Theorem 1 *The external potential, $V_{ext}(\vec{r})$, of any system of interacting particles is uniquely determined (up to a constant) by the particle density, $n_0(\vec{r})$, of the ground state.*

¹Equations in this chapter are written using atomic units: fundamental constants \hbar , e and m_e are set to unity.

Theorem 2 *The ground state energy of a system with an external potential $V_{\text{ext}}(\vec{r})$ is given by the minimum value of the energy functional $E_{HK}[n]$ and the density for which this minimum is reached corresponds with the ground state density $n_0(\vec{r})$.*

2.1.2 Kohn-Sham Equation

Now, the main problem is to find an approximate expression for $F[n(\vec{r})]$. The Kohn-Sham equation is a powerful method to solve this question. It considers a non-interacting system, where the kinetic energy can be calculated exactly, and a local external potential $V_{KS}(\vec{r})$ is added. The functional $F[n]$ can be divided into three parts:

$$F[n] = T_s[n] + E_H[n] + E_{XC}[n], \quad (2.5)$$

where $T_s[n]$ is the non-interacting kinetic energy functional and $E_{XC}[n]$ is the exchange-correlation (XC) energy. $E_H[n]$ is the Hartree energy functional, which is

$$E_H[n] = \frac{1}{2} \int d^3r \int d^3r' \frac{n(\vec{r})n(\vec{r}')}{|\vec{r} - \vec{r}'|}. \quad (2.6)$$

Apart from the last term, $E_{XC}[n]$, everything else can be calculated exactly. By $\int n(\vec{r})d\vec{r} = N$, we can obtain

$$\frac{\delta F[n]}{\delta n(\vec{r})} = -v(\vec{r}). \quad (2.7)$$

The effective local potential $V_{KS}(\vec{r})$ becomes

$$V_{KS}(\vec{r}) = v(\vec{r}) + \frac{\delta E_H[n]}{\delta n(\vec{r})} + \frac{\delta E_{XC}[n]}{\delta n(\vec{r})}, \quad (2.8)$$

and the Kohn-Sham equation is

$$\left[-\frac{1}{2}\nabla_i^2 + v(\vec{r}) + \frac{\delta E_H[n]}{\delta n(\vec{r})} + \frac{\delta E_{XC}[n]}{\delta n(\vec{r})} \right] \psi_\alpha(\vec{r}\sigma) = \varepsilon_\alpha \psi_\alpha(\vec{r}\sigma), \quad (2.9)$$

with ground-state electron density given by

$$n(\vec{r}) = \sum_\alpha \sum_\sigma^{occ.} |\psi_\alpha(\vec{r}\sigma)|^2. \quad (2.10)$$

These set of equations can be solved self-consistently. An initial guess of the density $n(\vec{r})$ determines the effective potential $V_{KS}(\vec{r})$, then the wave functions $\psi_\alpha(\vec{r}\sigma)$ can be

calculated from equation (2.9), a new density is calculated through equation (2.10). This procedure is repeated until self-consistency is reached.

2.1.3 Exchange-Correlation Functional

Although the Kohn-Sham method provides an exact expression for the total energy, unfortunately it is still not possible to solve the equation. The XC energy functional is not known exactly and therefore needs to be approximated. The simplest approximation for the exchange-correlation energy is the local density approximation (LDA). However, the generalized gradient approximation (GGA) has become popular in solid state calculations, which is a further upgrade of the LDA. Different constructions for GGA usually named after the corresponding authors, such as GGA-PW91 (Perdew and Wang's construction) [93, 94] and GGA-PBE (Perdew *et al.*'s construction) [95]. They are the most popular GGA approximations for solid state systems. Generally speaking, GGA-PBE is the most popular GGA approximations for solid state systems. However, the problem is that GGA-PBE always estimates the band gap of semiconductor.

The Hybrid Functional: HSE06

To solve the gap problem, the hybrid functionals which incorporate a part of the exact exchange from Hartree-Fock (HF) theory were proposed in calculations, such as PBE0. The PBE0 functional [96] is

$$E_{XC}^{PBE0} = \frac{1}{4}E_X^{HF} + \frac{3}{4}E_X^{PBE} + E_C^{PBE}. \quad (2.11)$$

The HSE06 [97, 98] takes into account the screened Coulomb potential for the exact part:

$$E_{XC}^{HSE} = \beta E_X^{HF,SR}(\omega) + (1 - \beta)E_X^{PBE,SR}(\omega) + E_X^{PBE,LR}(\omega) + E_C^{PBE}, \quad (2.12)$$

where β is the mixing parameter and ω is the parameter to control the screening range which defines the short-range (SR) and long-range (LR) parts. The values $\beta = 0.25$ and $\omega = 0.2$ are typically used in the HSE06 functional which turns out to give accurate band gaps and lattice constants, see the mean absolute error (MAE) of different functionals in Fig. 2.1 [99].

¹The SC40 test set is a collection of 40 elementary and binary solid compounds of various structures having a wide range of band gaps.

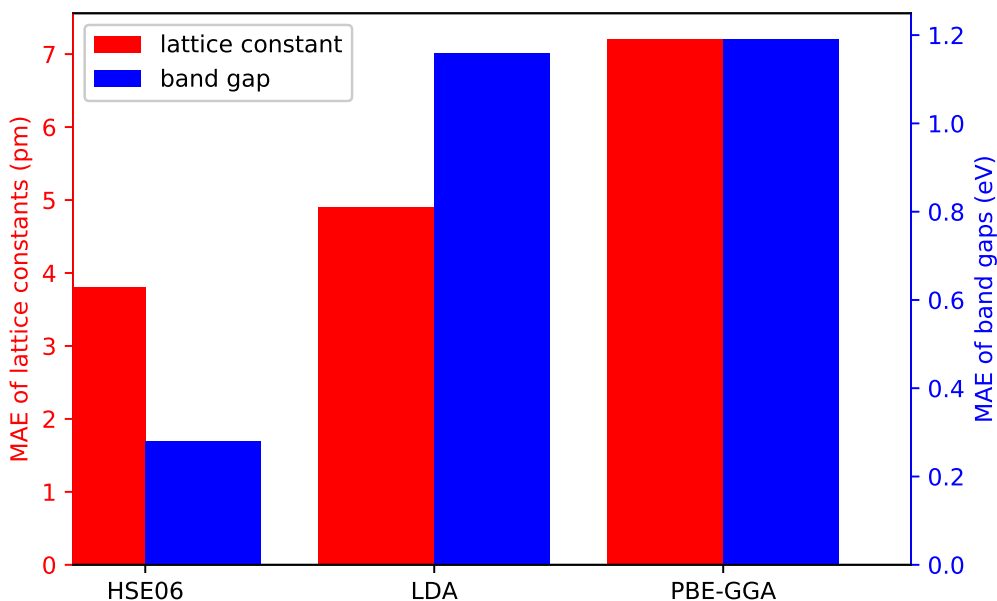


Fig. 2.1 MAE of the equilibrium lattice constants and band gaps of different functionals on SC40 solid test set¹. Data source: [99]

2.1.4 Software Packages

There are many different software packages capable of performing DFT calculations. The Vienna *ab initio* simulation package (VASP) code [100, 101], where the ion-electron interactions were described using projector-augmented-wave (PAW) potentials [102], is one of the most accurate codes that was used in the present thesis. The reason is not only its well-optimized performance on supercomputers gives good results in less time as compared with the others, but also it has a good interface with other softwares. Therefore, this code will be used as the main tool for all the calculations done in this thesis.

2.2 Tight-Binding Theory

With the applications of DFT in all kinds of numerical software packages, researchers who use DFT as a tool study practical materials without accurate knowledge of DFT. Hereby is called "black box". In order to give a more physical explanation of the results of density functional theory, we consider the tight-binding (TB) model. The physical picture of TB model is that there is not much difference between the electronic states in a solid and free atomic states. TB method was first proposed by F. Bloch in 1929 [103].

Its central idea is to use atomic orbitals as basis functions and to solve the Schrödinger equation by expressing the solution as a linear combination of atomic orbitals (LCAO)

For the μ -th atomic orbital of i -th atom located at $\vec{R} + \vec{\tau}_i$:

$$\phi_{\vec{R}m} = \phi_m(\vec{r} - \vec{R}) = \phi_{i\mu}(\vec{r} - \vec{R} - \vec{\tau}_i), \quad (2.13)$$

where \vec{R} is the lattice vector, and $\vec{\tau}_i$ is the atom location in unit cell. m is $i\mu$ (the μ -th atomic orbital of i -th atom). Bloch basis functions can be expressed as LCAO:

$$\phi_{m\vec{k}}(\vec{r}) = \sum_{\vec{R}} e^{i\vec{k}\cdot(\vec{R}+\vec{\tau}_i)} \phi_m(\vec{r} - \vec{R}). \quad (2.14)$$

Bloch eigenstates are

$$\psi_{n\vec{k}} = \sum_m C_m^{\vec{k}} \phi_m(\vec{r} - \vec{R}). \quad (2.15)$$

The Schrödinger equation of a single electron is

$$H\psi_{n\vec{k}}(\vec{r}) = E_{n\vec{k}}\psi_{n\vec{k}}(\vec{r}). \quad (2.16)$$

Using Dirac symbols, it can be rewritten as

$$|\psi_{n\vec{k}}(\vec{r})\rangle = \sum_m C_m^{\vec{k}} |\phi_{m\vec{k}}\rangle. \quad (2.17)$$

Then

$$\langle \phi_{m'\vec{k}} | H | \psi_{n\vec{k}} \rangle = \sum_m C_m^{\vec{k}} \langle \phi_{m'\vec{k}} | H | \phi_{m\vec{k}} \rangle = E_{n\vec{k}} \sum_m C_m^{\vec{k}} \langle \phi_{m'\vec{k}} | \phi_{m\vec{k}} \rangle, \quad (2.18)$$

where the matrix element of Hamiltonian is

$$H_{m'm} = \langle \phi_{m'\vec{k}} | H | \phi_{m\vec{k}} \rangle = \sum_{\vec{R}} e^{i\vec{k}\cdot(\vec{R}+\vec{\tau}_j-\vec{\tau}_i)} H_{m'm}(\vec{R}). \quad (2.19)$$

$H_{m'm}(\vec{R}) = \langle \phi_{m'\vec{k}} | H | \phi_{m\vec{k}} \rangle$ is the TB parameter, which is called the hopping term. Atomic orbital overlap integral can be expressed as

$$S_{m'm} = \langle \phi_{m'\vec{k}} | \phi_{m\vec{k}} \rangle, \quad (2.20)$$

and the Hamiltonian can be simplified as

$$\sum_m C_m^{n\vec{k}} (H_{m'm} - E_{n\vec{k}} S_{m'm}) = 0, \quad (2.21)$$

which is equal to solving the intrinsic equation

$$\det (H_{m'm} - E_{n\vec{k}} S_{m'm}) = 0. \quad (2.22)$$

It should be noted that atomic orbitals satisfy the orthogonality, $\langle \phi_{\vec{R}m} | \phi_{\vec{R}'n} \rangle = \delta_{\vec{R}\vec{R}'} \delta_{mn}$, the $S_{m'm} = 0$.

In 1954, J. C. Slater and G. F. Koster proposed a valuable method that uses a series of parameters replacing the hopping matrix elements, which is called Slater-Koster TB method [104]. This method can be applied in combination with results of DFT and experiment.

Here, we only consider the interaction between two atoms including 4 atomic orbitals ($s, p_x, p_y,$ and p_z) with a position vector \vec{r} . \vec{r} can be expressed as

$$\vec{r} = (r_x, r_y, r_z) = |\vec{r}| (l, m, n), \quad (2.23)$$

where $l/m/n$ is the direction cosine of the \vec{r} . The hopping matrix element, $H_{m'm}(\vec{R})$ can be expressed by corresponding Slater-Koster parameter, as shown in In Table 2.1.

Table 2.1 Slater-Koster parameters: $V_{ss\sigma}$, $V_{sp\sigma}$, $V_{pp\sigma}$, and $V_{pp\pi}$

	ϕ_s	ϕ_{p_x}	ϕ_{p_y}	ϕ_{p_z}
ϕ_s	$V_{ss\sigma}$	$lV_{sp\sigma}$	$mV_{sp\sigma}$	$nV_{sp\sigma}$
ϕ_{p_x}	$-lV_{sp\sigma}$	$l^2V_{pp\sigma} + (1-l^2)V_{pp\pi}$	$lm(V_{pp\sigma} - V_{pp\pi})$	$ln(V_{pp\sigma} - V_{pp\pi})$
ϕ_{p_y}	$-mV_{sp\sigma}$	$lm(V_{pp\sigma} - V_{pp\pi})$	$m^2V_{pp\sigma} + (1-m^2)V_{pp\pi}$	$mn(V_{pp\sigma} - V_{pp\pi})$
ϕ_{p_z}	$-nV_{sp\sigma}$	$ln(V_{pp\sigma} - V_{pp\pi})$	$mn(V_{pp\sigma} - V_{pp\pi})$	$n^2V_{pp\sigma} + (1-n^2)V_{pp\pi}$

2.3 Spin-Orbit Coupling

The spin angular momentum of an electron is $S_z = \hbar/2$, and its relationship to magnetic moment is

$$\vec{\mu} = -\frac{|e|\hbar}{mc} \vec{S} = -\frac{|e|\hbar}{mc} \frac{\vec{S}}{2}. \quad (2.24)$$

The origin of spin-orbit coupling (SOC) is the spin angular momentum and magnetic moment. The magnetic field strength for an electron is

$$\vec{H}_B = -\frac{\vec{v}}{c} \times \vec{E}. \quad (2.25)$$

The strength of SOC after relativistic effect correction is

$$H_{soc} = -\frac{1}{2} \vec{u} \cdot \vec{H}_B = \frac{1}{2m^2c^2} (\nabla V \times \vec{p}) \cdot \vec{S}. \quad (2.26)$$

For the electron in an atom, it can be written as

$$\vec{H}_{soc}^a = \xi(\vec{r}) \vec{L} \cdot \vec{S}, \quad (2.27)$$

where \vec{L} is the orbital angular momentum. The orbital angular momentum and spin angular momentum can be coupled by SOC, which is

$$\vec{J} = \vec{L} + \vec{S}. \quad (2.28)$$

Due to

$$\vec{J} \cdot \vec{J} = \vec{L} \cdot \vec{L} + \vec{S} \cdot \vec{S} + (\vec{L} \cdot \vec{S} + \vec{S} \cdot \vec{L}), \quad (2.29)$$

the relationship of quantum number $j/l/s$ becomes

$$j(j+1) = l(l+1) + s(s+1) + 2\langle \vec{L} \cdot \vec{S} \rangle / \hbar^2. \quad (2.30)$$

We can conclude that $\langle \vec{L} \cdot \vec{S} \rangle$ is the expected value of $\vec{L} \cdot \vec{S}$, and it is

$$\langle \vec{L} \cdot \vec{S} \rangle = \frac{\hbar^2}{2} [j(j+1) - l(l+1) - s(s+1)]. \quad (2.31)$$

We can see that $\langle \vec{L} \cdot \vec{S} \rangle$ can have two different values due to $j = 3/2$ or $1/2$ for p atomic orbital ($l = 1, s = 1/2$), which is the energy level splitting origins from SOC. It is generally accepted that the strength of SOC is related with the atomic number Z .

In the analysis of the low energy effective model, the new Hamiltonian can be written as

$$H = H_0 + H_{soc}, \quad (2.32)$$

where H_0 can be obtained by Slater-Koster parameters, and H_{SOC} can be obtained by a SOC parameter λ and a matrix. As we discussed above, we only consider s , p_x , p_y , and p_z atomic orbitals, and then the matrix elements of SOC can be express in Table 2.2.

Table 2.2 TB parameters of SOC

	s	p_x	p_y	p_z
s	0	0	0	0
p_x	0	0	$-is_z$	is_y
p_y	0	is_z	0	$-is_x$
p_z	0	$-is_y$	is_x	0

In real materials, SOC is very complex. It is a relativistic effect. Generally speaking, the larger atomic number, the more obvious SOC, but it is not absolute. Take the graphene as an example, its SOC effect is too small that no experiment can detect it. Many previous studies focused on this question [105–109]. Using first-principles calculation and TB model, Yao *et al.* show a gap of 0.8×10^3 meV, which is due to the C_3 symmetry of graphene. The Dirac point of graphene comes from p_z atomic orbitals of carbon atoms. The atomic number of carbon element is the same to that of nitrogen element. However, for the Dirac point coming from p_{xy} atomic orbitals of carbon/nitrogen, its SOC effect can be obvious, which can reach 5 meV [110]. By above analysis, the SOC effect in real materials is relationship to element, atomic orbitals, and structure symmetry.

2.4 Wilson Loop Method and Topological Invariant (Z_2)/Chern Number (C)

Many ways are proposed for calculating topological invariants [111]. One of the simplest way is the Fu-Kane parity criterion [49], which only involves the parity eigenvalues of the energy bands at the time-reversal invariant momentas in the inversion symmetry systems. However, not all the real systems are inversion symmetry systems, and we need much efforts to search the inversion symmetry system that is topological equivalent to inversion symmetry breaking system. Other proposals for calculating topological invariants involve very complicated numerical calculations [112]. Therefore, the most efficient and common way to calculate topological invariants is called as Wilson loop or Wannier charge centers methods [113, 114].

For a 2D system, we can choose a two parameter space such as (k_x, k_y) space in BZ in Fig. 2.2. If we let k_y be fixed, then a 1D subsystem could be defined in the k_x direction. For the 1D subsystem with discretized points $k_{x,i} (i = 1 \cdots N_x)$, we need to calculate the discretized non-Abelian Berry connection

$$F_{i,i+1}^{mn}(k_y) = \langle m, k_{x,i}, k_y | n, k_{x,i+1}, k_y \rangle. \quad (2.33)$$

Here, $|n, k_x, k_y\rangle$ is the cell periodic part of Bloch eigenstate. $U(2N)$ Wilson loop could be constructed by the discretized non-Abelian Berry connection $F_{i,i+1}^{mn}(k_y)$,

$$D(k_y) = F_{0,1} F_{1,2} \cdots F_{N_x-2, N_x-1} F_{N_x-1, 0}. \quad (2.34)$$

Then, we can diagonalize the matrix $D(k_y)$ to obtain the eigenvalues $\lambda_n(k_y)$. The phase angles for the Wilson loop method could be obtained by

$$\theta_n(k_y) = \text{Im}[\log \lambda_n(k_y)]. \quad (2.35)$$

We can also notice that θ_n is related with the Hybrid Wannier charge centers

$$\bar{x}_n = \frac{a}{2\pi} \int_0^{2\pi/a} \langle u_{nk} | i \partial_k u_{nk} \rangle dk = a \frac{\theta_n}{2\pi}, \quad (2.36)$$

where a is the lattice constant. So Wilson loop method is also called as Wannier charge centers methods.

The physical picture of Wilson loop method is that the evolution of phase angles θ_n in k_y parameter space, which indicates the winding of phase angles along the torus of BZ. For a Chern insulator (C), we need to observe the evolution of θ_n along $k_y \in [-\pi, \pi]$, as shown in Fig. 2.3. For the trivial case, we can see that θ winds the torus zero times, thus gives Chern number $C = 0$. For the nontrivial case, θ winds the torus one times, thus gives Chern number $C = 1$. For Z_2 insulator with time reversal symmetry, we need only consider $k_y \in [-\pi, 0]$, and there are two phase angles due to TR symmetry. We can conclude that the trivial case of $Z_2 = 0$ and nontrivial case $Z_2 = 1$, both are similar to the Chern insulator, as shown in Fig. 2.4.

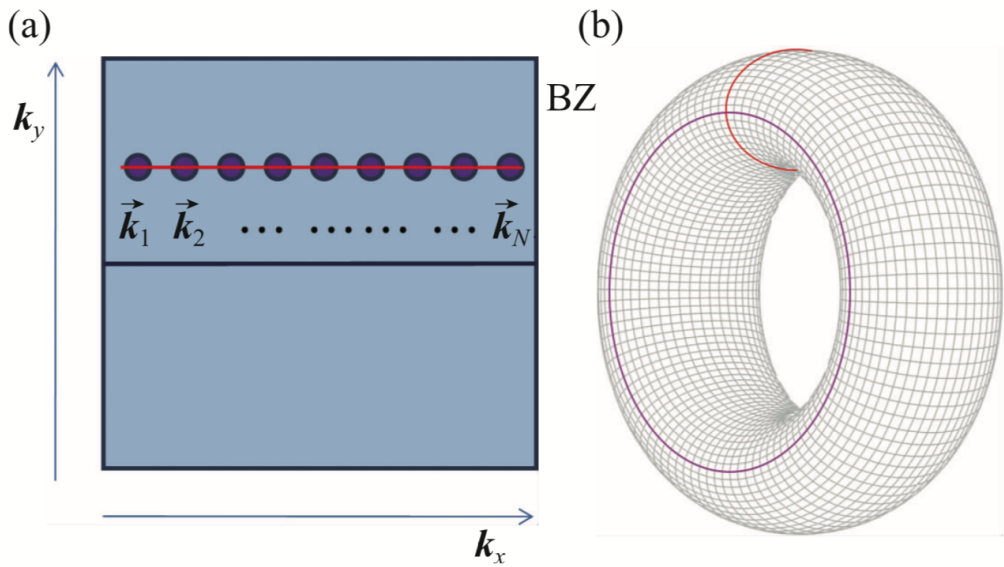


Fig. 2.2 Schematic representations of 2D BZ. (a) Periodic extension along the direction of k_x/k_y . (b) Torus surface. Image source: Ref. [115]

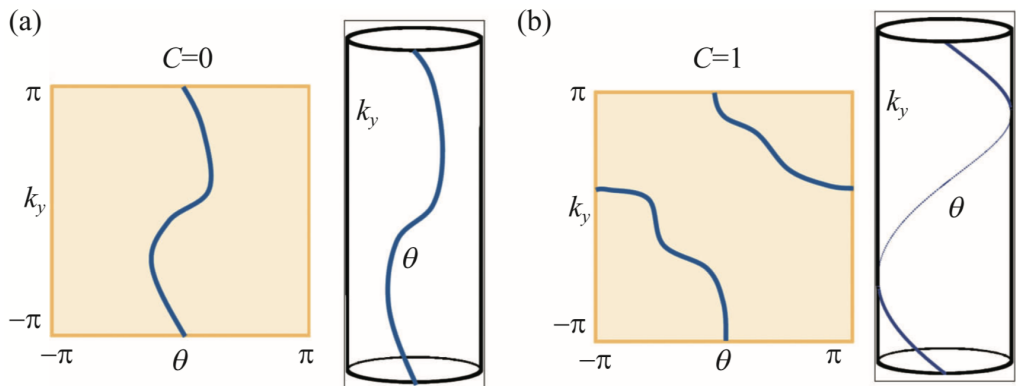


Fig. 2.3 Schematic representations of phase angle $\theta_n(k_y)$ evolution. (a) $C = 0$. (b) $C = 1$. Image source: Ref. [115]

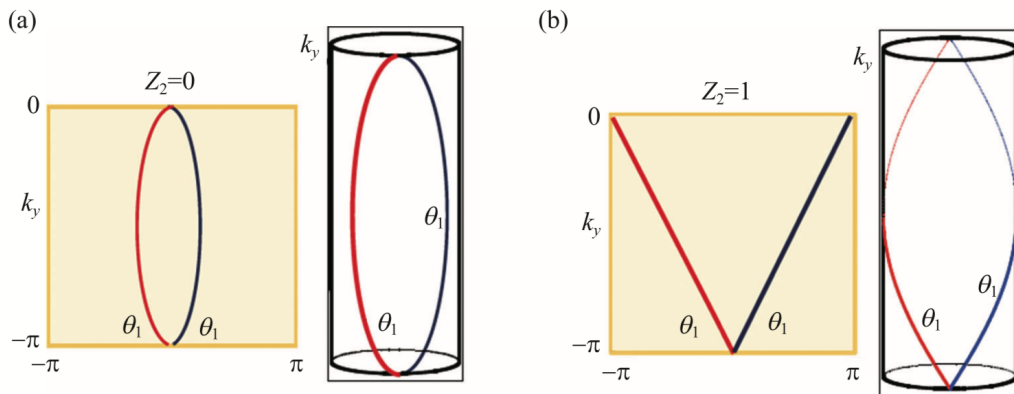


Fig. 2.4 Two different topological systems of band phase evolution under TR symmetry. (a) $Z_2 = 0$. (b) $Z_2 = 1$. Image source: Ref. [115]

Chapter 3

C-Based Material: H_{4,4,4}-Graphyne

¹Two-dimensional (2D) carbon materials play an important role in nanomaterials. We propose a new carbon monolayer, named hexagonal-4,4,4-graphyne (H_{4,4,4}-graphyne), which is a nanoporous structure composed of rectangular carbon rings and triple bonds of carbon. Using first-principles calculations, we systematically studied the structure, stability, and band structure of this new material. We found that its total energy is lower than that of experimentally synthesized β -graphdiyne and it is stable at least up to 1500 K. In contrast to the single Dirac point band structure of other 2D carbon monolayers, the band structure of H_{4,4,4}-graphyne exhibits double Dirac points along the high-symmetry points and the corresponding Fermi velocities ($1.04 \sim 1.27 \times 10^6$ m/s) are asymmetric and higher than that of graphene. The origin of these double Dirac points is traced back to the nodal line states, which can be well explained by a tight-binding model. The H_{4,4,4}-graphyne forms a moiré superstructure when placed on top of a hexagonal boron nitride substrate. These properties make H_{4,4,4}-graphyne a promising semimetal material for applications in high-speed electronic devices.

3.1 Introduction

Monolayer graphene was first realized in 2004 [2] and since then two-dimensional (2D) carbon material research has played a crucial role in nanomaterials. Many kinds of 2D carbon allotropes have been proposed due to the huge flexibility of the carbon bonding. Graphdiyne [17], a special structure of graphyne, has been realized experimentally.

¹The results of this chapter were published as: L. Li, X. Kong, and F. M. Peeters, Carbon **141**, 712 (2019).

Topological defects [116–118], which include non-hexagonal carbon rings, have been observed in graphene. Many newer 2D carbon allotropes have been predicted theoretically with novel crystal structures that can be classified into two general classes. The first are carbon monolayers that include some non-hexagonal carbon rings [119–121], such as Haeckelite $H_{5,6,7}$ [122]/phagraphene [123]/ Ψ -graphene [124] (5-6-7 rings), T graphene [125] (4-8 rings), and penta-graphene [126] (5 rings). These structures exhibit sp^2/sp^3 hybridization of the carbon atom. The second one are the carbon monolayers that have the triple bonds of carbon ($-C\equiv C-$) due to the sp hybridization of the carbon atom, such as $\alpha/\beta/\gamma/\delta/6,6,12$ -graphyne [127–129], in which the carbon atoms (sp^2 hybridization)/hexagonal carbon rings are connected by $-C\equiv C-$. These 2D carbon allotropes show different fundamental physical and chemical properties. Not only their band structure changes from metal/semimetal to semiconductor, but also they can be used in many energetic and environmental applications, such as for gas separation [130], and for water desalination [131]. The abundant new 2D carbon structures also provide efficient inspiration for structural predictions of other elements [132], leading to many more new lattice structures with excellent properties. Although many 2D carbon allotropes have been predicted, combining structural properties of the above two classes have been scarce up to now [133–135].

The topologically nontrivial materials, such as topological semimetals, have attracted broad interest. There are three distinct kinds of topological semimetals: Dirac, Weyl, and nodal line semimetals [136]. For the nodal line semimetals, the band crossing points form a continuous Dirac loop with a relatively higher density of states at the Fermi level [137], which is an advantage for high-speed electronic devices. Many kinds of three-dimensional (3D) nodal line bulk materials, such as $PtSn_4$ [138], $PbTaSe_2$ [139], and $ZrSiS$ [140, 141], have been realized experimentally. Theoretically, $TiTaSe_2$ [142], 3D-honeycomb graphene networks [143], Ca_3P_2 [144, 145], LnX ($Ln = La, Gd$; $X = Cl, Br$) [146], Cu_3PdN [147], and body-centered orthorhombic C_{16} [148], have been predicted to show nodal line states [149]. In contrast to the extended literature on 3D nodal line semimetals, the study of semimetal nodal line states in 2D materials is still in its infancy. This has only been confirmed experimentally in a Cu_2Si monolayer [150] and theoretical predictions of a nodal line band structure have been made for several 2D materials, such as Be_2C/BeH_2 [151], MX ($M = Pd, Pt$; $X = S, Se, Te$) [137], and A_3B_2 compound (A is a group-IIIB cation and B is a group-VA anion, such as Hg_3As_2) [152].

Therefore, there is a need for more predictions of new 2D nodal line semimetals that are stable and can be realized experimentally.

In this work, we constructed a new graphyne monolayer with a hexagonal lattice using rectangular carbon rings and triple bonds of carbon. According to the naming rule of graphyne and its lattice feature, $H_{4,4,4}$ -graphyne is obtained. Using first-principles calculations, we systematically investigated the structure, energy, stability, and electronic band structure of the $H_{4,4,4}$ -graphyne monolayer. This monolayer shows a nanoporous structure and its total energy is almost equal to that of β -graphyne. The phonon spectrum provides convincing evidence for the dynamical stability of $H_{4,4,4}$ -graphyne and our molecular dynamics (MD) calculations show that the monolayer is stable up to a high temperature. Different to the band structure with a single Dirac point as found in most other carbon monolayers, $H_{4,4,4}$ -graphyne owns a band structure consisting of double Dirac points along the high-symmetry points with high Fermi velocities, which we confirm using different calculation methods. From an analysis of the orbital-projected band structure, we found that the p_z atomic orbitals of the carbon atoms are responsible for the double Dirac points in the $H_{4,4,4}$ -graphyne monolayer. Using the p_z atomic orbitals, a tight-binding (TB) model is constructed, which not only reproduces the double Dirac points, but also shows that the physical origin of the double Dirac points can be traced back to the nodal line states. Finally, we show that the $H_{4,4,4}$ -graphyne/hexagonal boron nitride (h-BN) moiré superstructure is a possible way of realizing the $H_{4,4,4}$ -graphyne monolayer experimentally.

3.2 Calculation Method

Our first-principles calculations were performed using the Vienna *ab initio* simulation package (VASP) code [100, 101], implementing density functional theory (DFT). The ion-electron interactions were described using projector-augmented-wave potentials (PAW) [102]. The electron exchange-correlation functional was treated by using the generalized gradient approximation (GGA) in the form proposed by Perdew, Burke, and Ernzerhof (PBE) [153]. The atomic positions and lattice vectors were fully optimized using the conjugate gradient (CG) scheme until the maximum force on each atom was less than $0.01 \text{ eV}/\text{\AA}$. The energy cutoff of the plane-wave basis was set to 520 eV with an energy precision of 10^{-5} eV . The Brillouin zone (BZ) was sampled by using a $9 \times 9 \times 1$ Γ -centered Monkhorst-Pack grid. The vacuum space was set to at least 15 \AA in all the

calculations to minimize artificial interactions between neighboring slabs. The phonon spectrum was calculated using a supercell (4×4) approach within the PHONOPY code [154].

3.3 Results and Discussions

3.3.1 Structure

The investigated graphyne monolayer is shown in Fig. 3.1(a). Its hexagonal framework structure is composed of rectangular carbon rings, connected by the triple bonds of carbon. The carbon atoms in the rectangular carbon rings are close to sp^2 hybridization, because the angle of the two neighboring single bonds of carbon (-C-C-) is not equal to 120° while the carbon atoms in the -C \equiv C- are close to sp hybridization, because the four carbon atoms (-C-C \equiv C-C-) are not located in a strict straight line. According to the naming rule of graphyne [16], the new graphyne should be named as 4,4,4-graphyne. To distinguish the rectangular graphyne (R-graphyne) [155], which can also be called as 4,4,4-graphyne using the naming rule of graphyne, we call our proposed graphyne hexagonal-4,4,4-graphyne (H_{4,4,4}-graphyne). Most new predicted graphyne structures are based on the hexagonal graphene structure by inserting triple bonds of carbon, such as 6,6,12-graphyne [129], 14,14,14-graphyne [156], and α -graphyne (α -2/ α -3/ α -4 graphyne) [157, 158], while those with non-hexagonal carbon rings are rather exceptional [133–135, 155]. Here, we provide a novel structure model in which the rectangular carbon rings and triple bonds of carbon can coexist, providing a novel structure model for new stable carbon monolayers.

The lattice of the H_{4,4,4}-graphyne is not only a hexagonal lattice, but also a kagome lattice [152], which is formed by all the centers of the rectangular carbon rings. Its lattice constant is 11.82 Å. There are four kinds of bond lengths, which are labeled l_1 , l_2 , l_3 , and l_4 , as shown in Fig. reffig:3-1(a). The $l_1 = 1.247$ Å is the length of the carbon triple bond, which is formed by two carbon atoms close to sp hybridization and the value of l_1 is close to that of the other graphyne structures [127]. All the other carbon atoms are close to sp^2 hybridization with bond lengths, $l_2 = 1.351$ Å, $l_3 = 1.453$ Å, and $l_4 = 1.489$ Å. Since H_{4,4,4}-graphyne can be regarded as inserting -C \equiv C- into the -C-C- of graphenylene that are shared by 6 and 12 carbon rings [130], the graphenylene bond lengths (1.367/1.474/1.473 Å) are close to those of our structure ($l_2/l_3/l_4$). The nanoporous

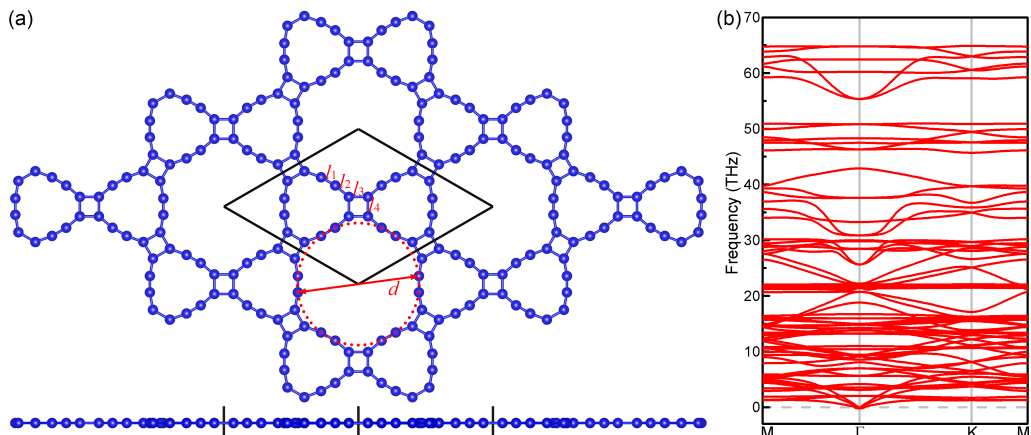


Fig. 3.1 Schematic representations (top and side views) of $H_{4,4,4}$ -graphyne (a) and its phonon spectrum along the high-symmetry points in the BZ (b). The blue dots are the carbon atoms. The four kinds of bond lengths are labeled l_1 , l_2 , l_3 , and l_4 , and the diameter of the circumcircle (red dotted line) of the 24 carbon ring is labeled d . The black box is the unit cell.

graphenylene membrane has been theoretically predicted to achieve efficient $^3\text{He}/^4\text{He}$ separation for industrial applications [130], while the graphyne membrane has been proposed for water desalination [131]. Besides these carbon monolayers, the C_2N - $h2D$ [159] and g - C_3N_4 [160] membranes have also been proposed for separation applications, depending on their nanoporous structure. The diameter $d = 9.30 \text{ \AA}$ of the circumcircle (red dotted line in Fig. 3.1(a)) of the 24 carbon ring of $H_{4,4,4}$ -graphyne is much larger than the one of other monolayers (5.49 \AA for graphenylene [130], 6.90 \AA for graphyne-3 [131], 5.51 \AA for C_2N - $h2D$ [159], and 4.76 \AA for g - C_3N_4 [160]) and is comparable to that of the well-known covalent organic frameworks, which have been shown to have potential for a wide range of applications in gas/liquid separation [161].

3.3.2 Energy and Stability

Introducing sp -hybridized carbon atoms can increase the system total energy (E_t in units of eV per carbon atom) of carbon allotropes. Graphene shows the lowest E_t in all the carbon allotropes while the graphyne structures have a higher E_t due to the presence of sp -hybridized carbon atoms [128]. Setting n (N) as the number of sp -hybridized carbon atoms (total carbon atoms) in the unit cell, we calculated the ratio n/N . For γ -graphyne, β -graphyne, and α -graphyne, E_t increases with the value of this ratio (Table 3.1). However, $H_{4,4,4}$ -graphyne shows the same ratio (0.50) as γ -graphyne, but its

E_t is higher than that of γ -graphyne and comparable to that of β -graphyne. This can be ascribed to the special structure of H_{4,4,4}-graphyne. In contrast to fully sp^2 -hybridized carbon atoms of γ -graphyne in which the three angles of the two neighboring single bonds are all 120° [127], the three angles in our structure are 140.1° (belonging to the 24 carbon ring), 129.9° (belonging to the 12 carbon ring), and 90° (belonging to the 4 carbon ring), which leads to an increase of E_t . Similar situations can apply to the sp -hybridized carbon atoms, where the angle between single bond and triple bond of H_{4,4,4}-graphyne becomes 170.1° (belonging to the 12 carbon ring) instead of 180° of γ -graphyne. Although H_{4,4,4}-graphyne shows a higher E_t as compared to graphene, it is still energetically preferable over some experimentally investigated carbon nanostructures, such as the β -graphdiyne film [162, 163] and the T-carbon nanowire [164]. The calculated E_t of β -graphdiyne/T-carbon is $-8.31/-7.92$ eV/atom [165], which is less favorable than the -8.37 eV/atom of the proposed H_{4,4,4}-graphyne structure, implying that there is a possibility that H_{4,4,4}-graphyne can be realized experimentally.

Table 3.1 Calculated ratio of sp -hybridized carbon atoms (n) to the total carbon atoms (N) in the unit cell and total energy E_t (eV/atom) of different 2D carbon allotropes.

2D carbon allotropes	Ratio (n/N)	E_t (eV/atom)
Graphene	0 (0/2)	-9.22
H _{4,4,4} -graphyne	0.50 (12/24)	-8.37
γ -graphyne	0.50 (6/12)	-8.58
β -graphyne	0.67 (12/18)	-8.38
α -graphyne	0.75 (6/8)	-8.30

Here we propose a possible chemical route to realize our new carbon material using the cyclobutadiene molecule (C₄H₄) [166, 167] and acetylene molecule (C₂H₂). Our calculated energy results confirm that the dehydrogenation process of C₄H₄ and C₂H₂, $3 \text{ C}_4\text{H}_4 + 6 \text{ C}_2\text{H}_2 \rightarrow \text{H}_{4,4,4}\text{-graphyne (24 carbon atoms per unit cell)} + 12\text{H}_2$, is an exothermic reaction (-4.76 eV/ unit cell of H_{4,4,4}-graphyne), implying that the chemical method is thermodynamically allowed [168]. Besides, many recent experiments clearly indicate that the members of the 2D carbon family are continuously increasing day by day. The successful syntheses of γ -graphyne (one triple bond between two hexagonal rings) [169] and graphtetrayne (four triple bonds between two hexagonal rings) [170] enrich the graphyne family while the successful synthesis of 4-6 carbophene (graphenylene) [130, 171] consisting of 4-carbon and 6-carbon rings in 1:1 ratio confirms the existence

of rectangular carbon rings in 2D carbon materials. The above experimental progresses of the syntheses of novel 2D carbon materials indicate that the $H_{4,4,4}$ -graphyne structure with rectangular carbon rings and triple bonds of carbon will have a very good chance to be synthesized in the future. Next, we studied the stability of $H_{4,4,4}$ -graphyne from dynamical and thermal aspects. The phonon spectrum of $H_{4,4,4}$ -graphyne is shown in Fig. 3.1(b). The phonon spectrum is free from imaginary frequency modes, which indicates that the $H_{4,4,4}$ -graphyne monolayer is dynamically stable. Then we confirm the thermal stability of the $H_{4,4,4}$ -graphyne monolayer by first-principles MD simulations. The MD simulations were performed by adopting the canonical ensemble with a Nose thermostat. We used a 2×2 supercell to perform MD simulations at 500 K, 1000 K, and 1500 K for 10 ps with a time step of 1 fs. The fluctuations of the total energy with time at the three temperatures are shown in Fig. 3.2(a), (b), and (c), and the corresponding snapshot of the atomic configuration after the MD simulations (10 ps) is given at the bottom of Fig. 3.2(a)/(b)/(c). The total energy of the system converges within this time scale. The final geometrical framework of the $H_{4,4,4}$ -graphyne structure containing the 4-12-24 carbon rings is well preserved and no structure reconstruction is found to occur in all the three cases. The three different temperatures have little influence on the nanoporous structure, implying that $H_{4,4,4}$ -graphyne monolayer is robust. The above dynamical and thermal results indicate that the $H_{4,4,4}$ -graphyne monolayer is stable at least up to 1500 K, which shows its great potential for applications in a high temperature environment.

3.3.3 Band Structure

The electronic band structure of the $H_{4,4,4}$ -graphyne monolayer is shown in Fig. 3.3. The red lines indicate the band structure at the PBE level (Fig. 3.3(a)), which shows two Dirac points at the P ($M-\Gamma$) and Q ($\Gamma-K$) points along the high-symmetry points in the BZ. An enlarged view of the bands at the P/Q point near the Fermi level is presented in Fig. 3.4(a)/(b), which shows that two bands cross linearly at the Fermi level and thus the charge carriers can be characterized by massless Dirac fermions. To fully confirm the existence of the double Dirac points, we used the more sophisticated Heyd-Scuseria-Ernzerhof (HSE06) [97, 98] hybrid functional method to calculate the band structure of $H_{4,4,4}$ -graphyne monolayer, which is shown in Fig. 3.3(b) (blue lines). Similar double Dirac points at P' ($M-\Gamma$) and Q' ($\Gamma-K$) points can also be clearly seen. From the enlarged view of the bands at the P'/Q' point near the Fermi level (Fig. 3.4(c)/(d)), we confirm

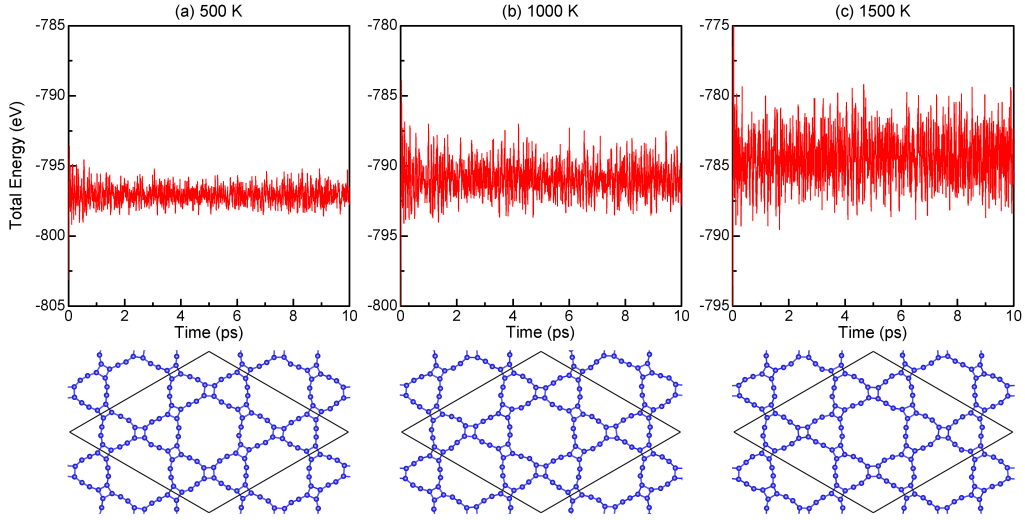


Fig. 3.2 Fluctuations of total energy as function of simulation time and the corresponding snapshots of the atomic configuration (top view) after the MD simulations (10 ps) at the temperature of 500 K (a), 1000 K (b), and 1500 K (c).

that the two bands cross linearly at the Fermi level, which is similar to the result of PBE. Although the PBE method typically underestimates the band gap of semiconductors, the fact that the HSE06 method gives the same Dirac points [172, 173] strengthens us in the validity of the band structure around the Fermi level. A few 2D carbon structures exhibit a Dirac point at the K point with a high velocity, such as α -graphyne [127], δ -graphyne [128], and graphene. Phagraphene [123] and β -graphyne [174] have a distorted Dirac point, which is not located in one of the high-symmetry points. In contrast to the above band structures with a single Dirac point, 6,6,12-graphyne [129] and buckled T graphene [125] show a band structure with double Dirac points along the high-symmetry points. Although $H_{4,4,4}$ -graphyne and buckled T graphene have similar double Dirac points around the Γ point, there is a major difference. The two Dirac points of $H_{4,4,4}$ -graphyne are at the same energy ($|E(P) - E(Q)| < 0.05$ meV and $|E(P') - E(Q')| < 0.09$ meV), which is different from that of buckled T graphene where the two Dirac points are separated by an energy of 25 meV [125].

From the Dirac point with linear bands, we can calculate the Fermi velocity (v_F) by a linear fitting of the first-principles calculations data. Because the Dirac points are not at the high-symmetry points, the double Dirac points can be regarded as two distorted Dirac points, which is similar to that in phagraphene [123]/distorted GaBi- X_2 monolayers ($X = I, Br, Cl$) [175]/1T- YN_2 [176]. In general, the distorted Dirac point has two different Fermi

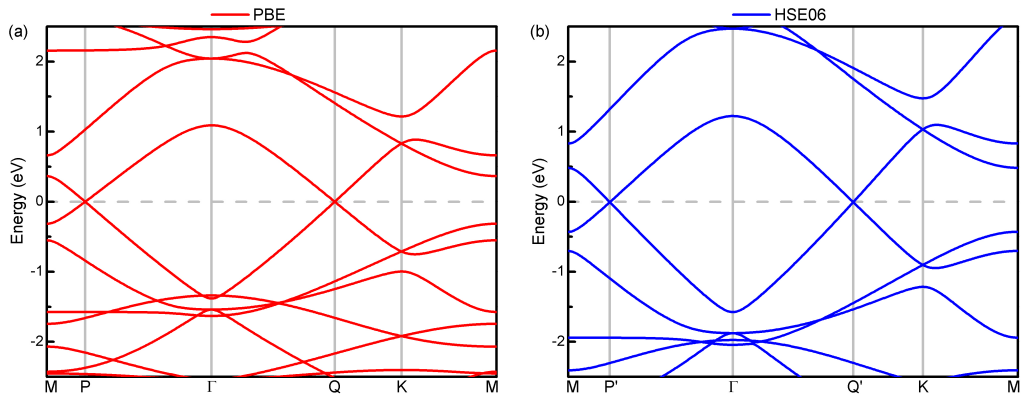


Fig. 3.3 Band structures of the $H_{4,4,4}$ -graphyne monolayer from PBE calculations (red lines, (a)) and HSE06 calculations (blue lines, (b)). The Dirac point in reciprocal space is labeled as P/Q/P'/Q'. The energy at the Fermi level was set to zero.

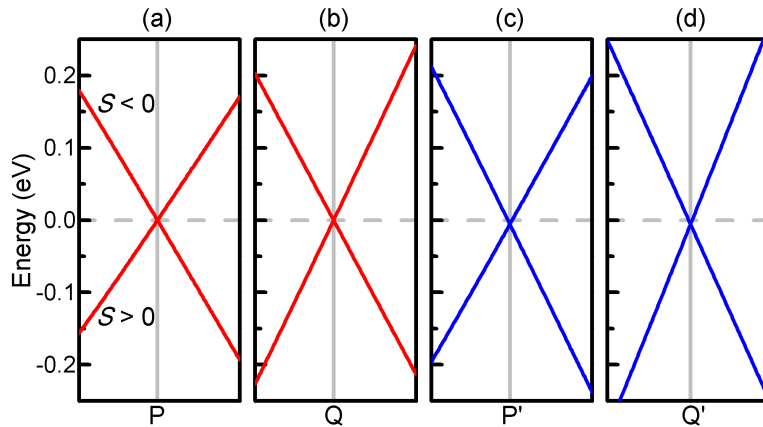


Fig. 3.4 An enlarged view of the bands at the P(a)/Q(b)/P'(c)/Q'(d) point near the Fermi level along the direction of M- Γ / Γ -K/M- Γ / Γ -K. Corresponding to Fig 3.3, the red/blue lines are the band structures from PBE/HSE06 calculations. The slope of the band close to the Dirac point P is indicated by S and a similar label can be applied to Q/P'/Q'.

velocities along the high-symmetry line directions. Setting the slope of the bands close to the Dirac point along the M- Γ (Γ -K) direction as S (Fig. 3.4(a)), we obtain two kinds of slopes ($S > 0$ and $S < 0$) at each Dirac point, and thus two different Fermi velocities can be obtained. For the band structures at the PBE level (red lines, Fig. 3.4(a) and (b)), the Fermi velocities of the two distorted Dirac points are $v_F(P, S > 0) = 0.87 \times 10^6$ m/s, $v_F(P, S < 0) = 0.99 \times 10^6$ m/s, $v_F(Q, S > 0) = 1.07 \times 10^6$ m/s, and $v_F(Q, S < 0) = 0.95 \times 10^6$ m/s. Comparing these results with that of graphene at the PBE level, $v_F(K) = 0.83 \times 10^6$ m/s, the Fermi velocities of H_{4,4,4}-graphyne ($0.87 \sim 1.07 \times 10^6$ m/s) are slightly high. It is well known that there are many kinds of 2D carbon structures with a Dirac point, but their Fermi velocities are lower than that of graphene [123], such as α -graphyne (0.687×10^6 m/s) [158] and δ -graphyne (0.696×10^6 m/s) [128]. To our knowledge, the Fermi velocities of H_{4,4,4}-graphyne are the highest Fermi velocities among all the 2D carbon structures. To further confirm the superiority to graphene, we also calculated the four Fermi velocities at the HSE06 level (blue lines, Fig. 3.4(c) and (d)). The Fermi velocities are $v_F(P', S > 0) = 1.04 \times 10^6$ m/s, $v_F(P', S < 0) = 1.19 \times 10^6$ m/s, $v_F(Q', S > 0) = 1.27 \times 10^6$ m/s, and $v_F(Q', S < 0) = 1.13 \times 10^6$ m/s. These results ($1.04 \sim 1.27 \times 10^6$ m/s) are also slightly higher than the result for graphene at the HSE06 level, $v_F(K) = 1.01 \times 10^6$ m/s. From the above results obtained within different calculations methods, we confirm the ultrahigh Fermi velocity of H_{4,4,4}-graphyne, which is advantageous for building high-speed electronic devices, such as field effect transistor.

To investigate the origin of the double Dirac points, we calculated the orbital-projected band structure along the high-symmetry points in the BZ at the PBE level as shown in Fig. 3.5(a). It is clear that the bands (red dots) including the double Dirac points close to the Fermi level originate from the p_z atomic orbitals of the carbon atoms. This is similar to most other 2D carbon structures having a Dirac point, such as phagraphene [123], δ -graphyne [128], and α -graphyne [158] and the interaction between the p_z atomic orbitals leads to the formation of a π -conjugated framework. The $s + p_x + p_y$ atomic orbitals only contribute to the bands (blue dots) located in the region around 1.2 eV (valence band) and 2.4 eV (conduction band) away from the Fermi level.

For most 2D carbon structures, their low energy band structures can be well reproduced by a TB model. To further illustrate the band structure with the double Dirac points of H_{4,4,4}-graphyne monolayer, we propose a TB model involving only the p_z atomic orbitals of the twenty-four carbon atoms in the unit cell. The effective Hamiltonian is

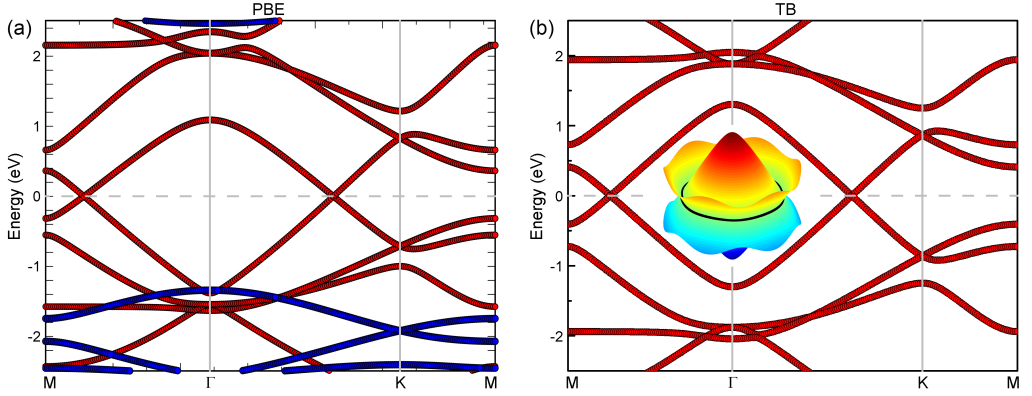


Fig. 3.5 Orbital-projected band structure of $H_{4,4,4}$ -graphyne monolayer from PBE calculations (a) and band structure of $H_{4,4,4}$ -graphyne monolayer from TB calculations (b). In figure (a), the red (blue) dots represent the contributions from the p_z ($s+px+py$) atomic orbitals of the carbon atoms. The red dots in figure (b) correspond to those in figure (a). The 3D band structure from TB calculations around the nodal line is presented as an insert in figure (b).

taken as [128]

$$H = \sum_{\langle ij \rangle} (t_{ij} c_i^\dagger c_j + h.c.), \quad (3.1)$$

where c_i^\dagger and c_j represent the creation and annihilation operators of an electron at the i -th atom, respectively. Since all atoms are carbon atoms, we can neglect the on-site energy difference of these carbon atoms and set it as zero. To get a better understanding for the appearance of the double Dirac points, we only consider the hopping of the p_z atomic orbitals between the nearest-neighboring carbon atoms. Corresponding to the four bond lengths (l_1 , l_2 , l_3 , and l_4), there are four hopping parameters $t(l_1)$, $t(l_2)$, $t(l_3)$, and $t(l_4)$. The distance-dependent hopping energy is determined by the formula $t(l_m) = t_0 \exp[q(1 - l_m/l_0)]$ [123], where $t_0 = 2.7$ eV, $q = 2.2$, $l_0 = 1.5$ Å, and $m = 1, 2, 3, 4$. We can obtain the band structure of $H_{4,4,4}$ -graphyne by diagonalizing a 24×24 matrix in reciprocal space along the high-symmetry points and the result is shown in Fig. 3.5(b). Corresponding the red dots representing the contributions from the p_z atomic orbitals of the carbon atoms in Fig. 3.5(a), the TB bands that are also indicated by the red dots are in good agreement with the PBE results; in particular, the double Dirac points at the Fermi level are very accurately reproduced.

Double Dirac points in 2D carbon structures can have two kinds of origins. One is the double Dirac cones as shown in cp-graphyne [133] and 6,6,12-graphyne [174], where the

two Dirac points come from the two Dirac cones. Another one is that the linear dispersion relation near the Fermi level exists in each direction forming a Dirac loop, which is called a nodal line band structure, such as in buckled T graphene [125]. To further distinguish the two kinds of origins in $H_{4,4,4}$ -graphyne, we calculated the 3D band structure (insert of Fig. 3.5(b)) around the double Dirac points. Notice that the two band lines forming the double Dirac points become two band surfaces, which cross at the Fermi level forming a Dirac loop (black line in insert of Fig. 3.5(b)). This kind of band structure should obviously be a Dirac nodal line band structure, which implies that $H_{4,4,4}$ -graphyne is a 2D Dirac nodal line semimetal [137, 150–152, 177–179].

3.3.4 Moiré Superstructure

H-BN is an appealing substrate material, because it has an atomically smooth surface that is relatively free of dangling bonds and charge traps [180]. It has been a standard substrate for graphene, as confirmed experimentally and theoretically [181, 182]. Different from the simple stacking models, such as AA and AB, the graphene/h-BN heterostructure results in a moiré superstructure stacking model, where the interaction between the two planer layers is due to van der Waals (vdW) force [181, 182]. In theoretical calculations and experimental syntheses, since h-BN substrate can well preserve the hexagonal honeycomb structure of graphene [181, 182], it has been a preferential substrate for other 2D monolayer structures, such as silicene [183]/germanene [184] and β -graphdiyne [163]/graphdiyne [185]. Here, we constructed a $H_{4,4,4}$ -graphyne/h-BN heterostructure with the moiré superstructure stacking model. The superstructure is shown in Figure 6(a), in which we used the $\sqrt{21} \times \sqrt{21}$ h-BN supercell to match the 1×1 $H_{4,4,4}$ -graphyne. In the PBE calculations of the superstructure, the vdW interaction is included (DFT-D3) [186]. Similar to other moiré superstructures, such as graphene/h-BN [182], silicene/h-BN [183], germanene/h-BN [184], and silicene/MoS₂ [187], an obviously rotation angle between the lattices of $H_{4,4,4}$ -graphyne and h-BN substrate can be seen. The corresponding band structure is shown in Fig. 3.6(b). It is clear that the bands from the h-BN substrate are far away from the Fermi level and the double Dirac points are still located at the Fermi Level. Due to the effect of h-BN substrate, a small band gap will be opened in the two Dirac points, which is similar to the experiment of graphene/h-BN [188]. We therefore propose that the h-BN substrate may be an ideal substrate for $H_{4,4,4}$ -graphyne, which contributes to the stabilization of the monolayer.

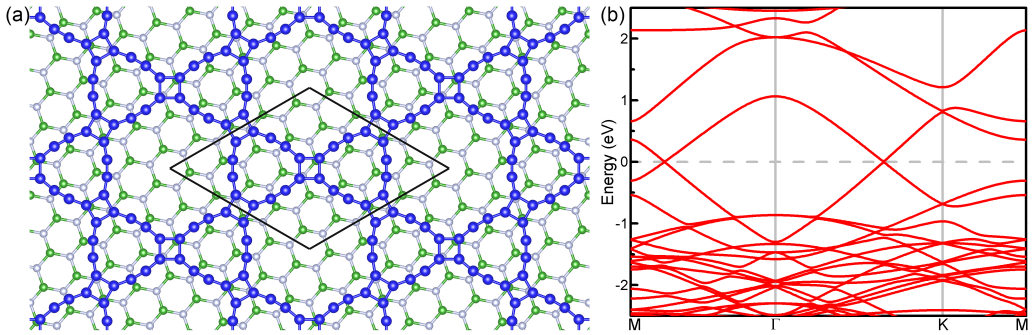


Fig. 3.6 Schematic representation (top view) of $H_{4,4,4}$ -graphyne/h-BN moiré superstructure (a) and corresponding band structure from PBE + vdW calculations (b). The blue/green/silver dots are carbon/boron/nitride atoms.

3.4 Conclusion

In summary, using first-principles calculations combined with a TB model, we predict that the new carbon monolayer, $H_{4,4,4}$ -graphyne, is a nodal line semimetal with: 1) a nanoporous structure, 2) high stability, 3) band structure with double Dirac points, and 4) ultrahigh Fermi velocities. The nanoporous structure shows potential applications for gas/liquid separation. The value of the total energy, phonon calculations, and MD simulations fully confirm its energetic, dynamical, and thermal stability. The double Dirac points with ultrahigh Fermi velocities make $H_{4,4,4}$ -graphyne a promising material for high-speed electronic devices. A simple TB model was constructed and shows that the origin of the double Dirac points is the nodal line states. At last, we pointed out that the $H_{4,4,4}$ -graphyne/h-BN moiré superstructure shows a possible way of realizing $H_{4,4,4}$ -graphyne monolayer experimentally.

Chapter 4

C-Based Materials: Dumbbell C₄N

¹Two-dimensional (2D) carbon nitride materials play an important role in energy-harvesting, energy-storage and environmental applications. Recently, a new carbon nitride, 2D polyaniline (C₃N) was proposed [PNAS 113 (2016) 7414-7419]. Based on the structure model of this C₃N monolayer, we propose two new carbon nitride monolayers, named dumbbell (DB) C₄N-I and C₄N-II. Using first-principles calculations, we systematically study the structure, stability, and band structure of these two materials. In contrast to other carbon nitride monolayers, the orbital hybridization of the C/N atoms in the DB C₄N monolayers is sp^3 . Remarkably, the band structures of the two DB C₄N monolayers have a Dirac cone at the K point and their Fermi velocities ($2.6/2.4 \times 10^5$ m/s) are comparable to that of graphene. This makes them promising materials for applications in high-speed electronic devices. Using a tight-binding model, we explain the origin of the Dirac cone.

4.1 Introduction

Monolayer graphene was first realized in 2004 [2] and since then the group IV elemental monolayers have played a crucial role in the field of two-dimensional (2D) materials. In experiments, silicene, germanene, and stanene were all synthesized on different substrates [189–197], such as heterostructures of silicene(germanene)/MoS₂ [193, 195] and stanene/Bi₂Te₃ [197], which preserve the hexagonal honeycomb structure of the isolated monolayers. Without spin-orbit coupling (SOC), silicene, germanene, and stanene all have a zero electronic band gap with two bands crossing linearly at the

¹The results of this chapter were published as: L. Li, X. Kong, O. Leenaerts, X. Chen, B. Sanyal, and F. M. Peeters, Carbon **118**, 285 (2017).

Fermi level and their extremely large Fermi velocity (v_F) makes them ideal materials for high-speed electronic devices [198, 199]. Taking SOC into account, they all show a nontrivial band gap at the K point which can reach up to 73.5 meV (stanene), making them promising to realize quantum spin Hall (QSH) effect at room-temperature [199]. Besides the buckled hexagonal honeycomb structure, another stable structure model of Si/Ge/Sn, known as the dumbbell (DB) structure, was proposed in previous studies [200–202]. Different to the band structure of stanene, the DB structure of Sn shows a band inversion at the Γ point due to SOC and was predicted to be a 2D topological insulator [200]. By functionalization, Sn/Ge DB structures show nontrivial band gaps that can reach up to 235 meV [203–206] while the Si DB structure can also become a 2D topological insulator under external strain [207]. In contrast to the extended literature on DB structures of Si/Ge/Sn, studies on the DB structure of C have been scarce up to now [208].

Besides the group IV elemental monolayers and their allotropes, carbon nitride materials are another important set of 2D materials. Many 2D carbon nitride materials can be applied in some important physical and chemical processes. Among these, graphitic carbon nitride (g-C₃N₄) has been studied for a long time [209] and it can be used in many energetic and environmental applications, such as hydrogen generation [210], efficient energy storage [211], and photocatalytic degradation of pollutants [212]. Nanoporous carbon nitride materials, such as the C₂N monolayer [34], can be applied in gas separation [213, 214, 160] or water desalination [215]. The carbon nitride materials not only have a huge potential in applications but also exhibit many interesting physical effects, including QSH [216], quantum anomalous Hall (QAH) [217, 218], and spin-polarization [219, 220] effects. More and more new 2D carbon nitride materials have been produced in experiment. Recently, an interesting new 2D carbon nitride material, called polyaniline (C₃N), was synthesized [35]. Its monolayer shows a similar structure as graphene and its band structure is semiconducting with an indirect band gap, in contrast to the Dirac band structure of graphene.

Based on the C₃N monolayer structure and the DB structure of Si/Ge/Sn, we propose two new C₄N monolayers with a DB structure (DB C₄N). According to the positions of the raised C/N atoms, two configurations, DB C₄N-I and DB C₄N-II, can be obtained. Using first-principles calculations, we investigated systematically the structure, energy, stability, and electronic band structure of these two DB C₄N monolayers. Different to other carbon nitride monolayers, all the C and N atoms in the DB C₄N monolayers have

sp^3 hybridization. Although the two DB C_4N monolayers have a different structure and ground state energy, the phonon spectra provide convincing evidence for their thermal and dynamical stability. Similar to the Dirac cone band structure of graphene, the two DB C_4N monolayers both show a Dirac cone at the K point with a large Fermi velocity. An analysis of the projected electron density of states (PDOS) and the electron wave functions of the Dirac cones shows that four p_z atomic orbitals are responsible for the Dirac cone in these two C_4N monolayers. This is also supported by our tight-binding (TB) model including four p_z atomic orbitals that reproduces the first-principles results quite well.

4.2 Calculation Method

Our first-principles calculations were performed using the Vienna *ab initio* simulation package (VASP) code [100, 101], implementing density functional theory (DFT). The ion-electron interactions were described using projector-augmented-wave potentials (PAW) [102]. The electron exchange-correlation functional was treated by using the generalized gradient approximation (GGA) in the form proposed by Perdew, Burke, and Ernzerhof (PBE) [153]. The Brillouin zone (BZ) was sampled by using a $17 \times 17 \times 1$ Γ -centered Monkhorst-Pack grid. The vacuum space was set to at least 20 Å in all the calculations to minimize artificial interactions between neighboring slabs. The phonon spectra were calculated using a supercell approach within the PHONOPY code [154]. Other settings of calculation are the same to Chapter 3.2.

4.3 Results and Discussions

4.3.1 Geometrical Structure

The two investigated DB C_4N monolayers are shown in Fig. 4.1(a) and (b). They are based on the C_3N monolayer (Fig. 4.1(c)), which was recently synthesized in experiment [35]. By adsorbing C atoms on all the N atom positions of the C_3N monolayer, we obtain two different DB C_4N monolayers. The two patterns are classified as follows: (1) If the raised N/C atoms are on one side of the monolayer, as shown in Fig. 4.1(a), we call it DB C_4N -I; (2) If the raised N/C atoms are on two opposite sides of the monolayer, as shown in Fig. 4.1(b), we call it DB C_4N -II. In the following, we will analyze the three

monolayers (DB C₄N-I, DB C₄N-II, and C₃N) from the points of view of symmetry, orbital hybridization style, and bond length.

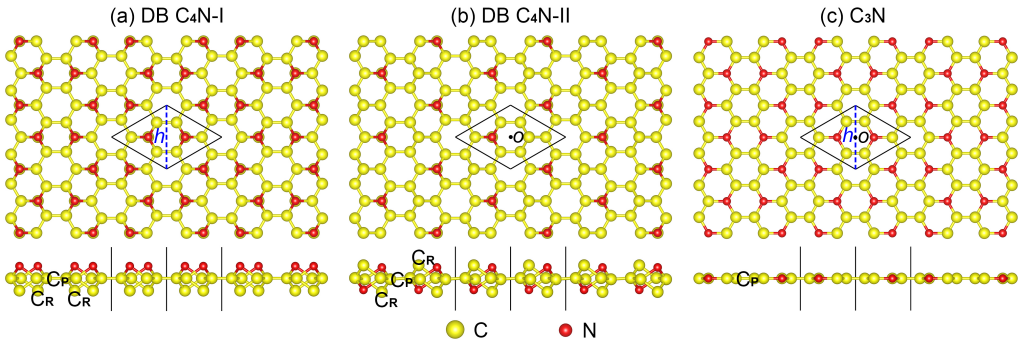


Fig. 4.1 Schematic representations (top and side views) of the DB C₄N-I (a), DB C₄N-II (b) and C₃N (c). The raised C atoms are labeled as C_R and the planar C atoms are labeled as C_P. The yellow (red) symbols are the carbon (nitrogen) atoms.

Considering symmetry first, the C₃N monolayer has higher symmetry than the C₄N monolayers. For the C₃N monolayer, the C/N atoms are not only center symmetric about the point *o* (black point, Fig. 4.1(c)), but also mirror symmetric about the plane *h* (blue dashed line, Fig. 4.1(c)) parallel to the *z* axis. However, the C/N atoms of the DB C₄N-I are only mirror symmetric about the plane *h* (blue dashed line, Fig. 4.1(a)) parallel to the *z* axis while the C/N atoms of the DB C₄N-II are only center symmetric about the point *o* (black point, Fig. 4.1(b)). Next, let us take a look at the hybridization of the atoms. The C/N atoms in the C₃N monolayer have *sp*² hybridization, similar to the atoms in graphene or g-C₃N₄. On the other hand, all the C/N atoms in the DB C₄N monolayers have *sp*³ hybridization, similar to the C atoms in diamond.

Corresponding to the change in hybridization, their bond lengths are very different. There are three kinds of atoms in the DB C₄N monolayers, N atoms, raised C (C_R) atoms, and planar C (C_P) atoms, while there are only N atoms and C_P atoms in the C₃N monolayer. In the following, we will discuss the bonds between the different atoms. Considering the N–C_P bond, one N atom can form a bond with three C_P atoms and the lengths of the three bonds are the same, labeled as *L*. For the DB C₄N-I and C₄N-II, *L* = 1.558 Å and *L* = 1.545 Å, respectively, which is larger than the *L* = 1.403 Å in C₃N. Between the C atoms, only C_P–C_P bonds are found in the C₃N monolayer and we label them as *M* (*M* = 1.404 Å). Similar bonds are also found in the DB C₄N monolayers. The C_P atoms of the DB C₄N-I are all in the same *xy* plane. However, there is a little

buckling (0.095 Å) along the z axis between the C_P atoms in the DB C_4N -II due to the inequivalence of the N and C_R atoms. The M of the DB C_4N -I and C_4N -II is 1.491 Å and 1.488 Å, respectively. There is also another C–C bond in the DB C_4N monolayers between the C_P atom and the C_R atom, which is labeled as M' . The M' of the DB C_4N -I (C_4N -II) is 1.567 Å (1.583 Å). From the above data of bond lengths, we can summarize that all the bond lengths in the two DB C_4N monolayers are 1.49 ~ 1.58 Å, which is much larger than the 1.40 Å in the C_3N monolayer. A similar difference is also found in the C–C bond length of diamond (1.54 Å) [221] and graphene (1.42 Å) [222], which comes from the different hybridization of the C atoms (sp^3 and sp^2). In most experimental and predicted carbon nitride monolayers, the C and N atoms have sp^3/sp hybridization, while the carbon nitride monolayers with sp^3 -hybridized C/N atoms are rarely studied [223]. Here, we provide a novel structure model for new stable carbon nitride monolayers. Although there is much difference in bond length, the lattice constants of the C_3N (4.861 Å) and the DB C_4N (4.775 Å (C_4N -I) and 4.768 Å (C_4N -II)) are almost the same. The optimized geometrical structure data are summarized in Table 4.1.

Table 4.1 Structure parameters and formation energies of the DB C_4N and C_3N monolayers. α is the lattice constant. L , M , and M' are the lengths of the N– C_P , C_P – C_P , and C_P – C_R bonds, respectively. The unit of α , L , M , and M' is Å. The formation energy ΔE corresponds to the energy release of the C_3N monolayer adsorbing isolated magnetic C atoms (eV/C atom).

Three monolayers	α	L (N– C_P)	M (C_P – C_P)	M' (C_P – C_R)	ΔE
C_4N -I	4.775	1.558	1.491	1.567	–3.272
C_4N -II	4.768	1.545	1.488	1.583	–3.379
C_3N	4.861	1.403	1.404	–	–

4.3.2 Energy and Stability

We calculated the formation energy of the DB C_4N monolayers as $\Delta E = [E(C_4N) - E((C_3N)) - 2 \times \mu_C]/2$, where $E(C_4N)/E((C_3N))$ is the total energy of the DB C_4N/C_3N monolayer. The chemical potential of the adsorbed C atoms (μ_C) is highly dependent on the carbon resources. Using graphene as a carbon resource, we will get positive formation energy (4.707 eV/C atom and 4.600 eV/C atom), which is similar to that of incorporating C atoms into g- C_3N_4 [224]. Using isolated magnetic C atoms as the carbon resource, the formation energy ΔE of the DB C_4N -I (C_4N -II) is –3.272 eV/C atom

(-3.379 eV/C atom), which is of the same magnitude as adsorbed C atoms on graphene [225]. The negative formation energy suggests the stability and feasibility of the DB C₄N. In experiment, carbon atoms and carbon atomic chains have been observed on graphene using transmission electron microscope (TEM) and TEM studies demonstrated that individual carbon atoms can be adsorbed on graphene surfaces with a stable structure at room-temperature [225–227]. Since 2D C₃N has been realized in experiment, the DB C₄N monolayers are probably also suited for experimental synthesis. Considering the two DB C₄N monolayers, the energy of the DB C₄N-II is lower than that of the DB C₄N-I. This can be ascribed to the differences in their structures. The DB C₄N-I monolayer exhibits a polarized structure due to the absence of inversion symmetry while the DB C₄N-II has no dipole moment. From the views of energy and symmetry, the DB C₄N-II is more stable than the DB C₄N-I. Although the two DB C₄N monolayers have different ground state energies, their phonon spectra (Fig. 4.2) are both free from imaginary frequency modes, which indicates that they are dynamically stable.

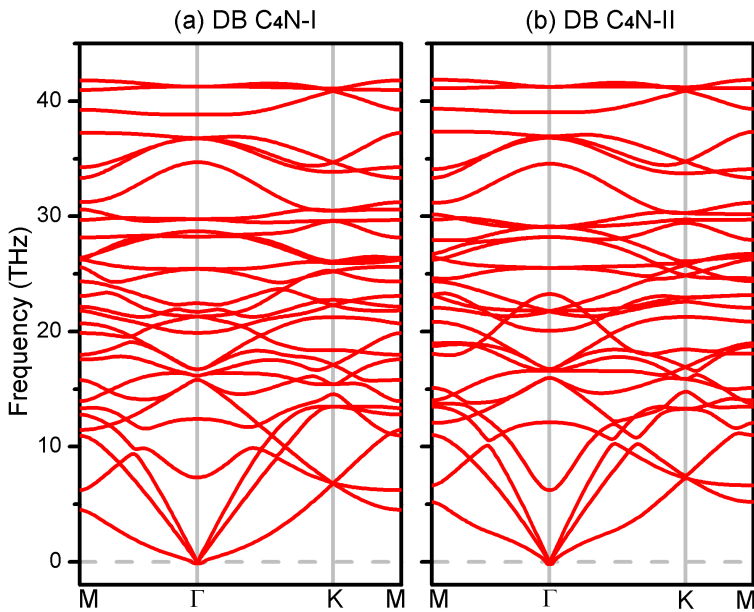


Fig. 4.2 Phonon spectra of DB C₄N-I (a) and DB C₄N-II (b) along the high-symmetry lines in the BZ.

4.3.3 Band Structure

The C₃N monolayer shows a band gap close to the Fermi level and a Dirac point below the Fermi level (Fig. 4.3), in agreement with a previous study [35]. The electronic band structures of the DB C₄N-I and C₄N-II monolayers are shown in Fig. 4.4. For both cases, a zero band gap at the K point is seen. Two bands cross linearly at the Fermi level and the charge carriers can be characterized by massless Dirac fermions, similar to the band structure of graphene (silicene/germanene/stanene) at the K point [198, 199]. To confirm the existence of the Dirac cones, we used the more sophisticated Heyd-Scuseria-Ernzerhof (HSE06) [97, 98] hybrid functional method to calculate the band structures of the DB C₄N monolayers (Fig. 4.5) and the Dirac cones at the K point can be clearly seen. By a linear fitting of the first-principles calculations data, we can obtain the Fermi velocity of the DB C₄N. For the DB C₄N-I (C₄N-II), the Fermi velocity is 2.6×10^5 m/s (2.4×10^5 m/s), which is comparable to that of the group IV elemental monolayers ($4.70 \sim 8.46 \times 10^5$ m/s) [199]. The extremely large Fermi velocity makes the DB C₄N monolayers ideal materials for building high-speed electronic devices, such as field effect transistor (FET). It is well known that there are many kinds of Dirac carbon monolayers in experiment and theory, such as graphene [228], $\alpha/\beta/\gamma/6,6,12$ -graphyne [174, 158, 128], phagraphene [123], etc. However, the 2D carbon nitride materials in experiment, such as g-C₃N₄, C₂N, and g-C₆N₆ monolayers, all show semiconductor behavior with a band gap of 2.73 eV [229], 1.96 eV [34], and 1.53 eV [216], respectively. Dirac cone band structures for carbon nitride materials are rarely predicted and only the g-C₁₄N₁₂ and g-C₁₀N₉ were proposed as spin-polarized Dirac materials [217, 218]. To our knowledge, the two DB C₄N monolayers are the first predicted Dirac carbon nitride materials without spin-polarization. In contrast to the g-C₆N₆ monolayer proposed by Wang *et al.* [216] and the C₃N monolayer [35], the Dirac cone of the DB C₄N is right at the Fermi level, which is advantageous for experiments and applications.

To investigate the origin of the Dirac cones, we calculated the PDOS for different atomic orbitals and the Kohn-Sham wave functions at the Dirac points, as shown in Fig. 4.6. From the PDOS analysis of the two DB C₄N monolayers, it is clear that the summed states of the s , p_x , and p_y atomic orbitals around the Fermi level are far less than the PDOS corresponding to the p_z atomic orbitals. Although the C/N atoms are sp^3 -hybridized, the states close to the Fermi level mainly come from the p_z atomic orbitals, which is similar to graphene/graphyne [174, 158, 128, 123]. As for phagraphene where

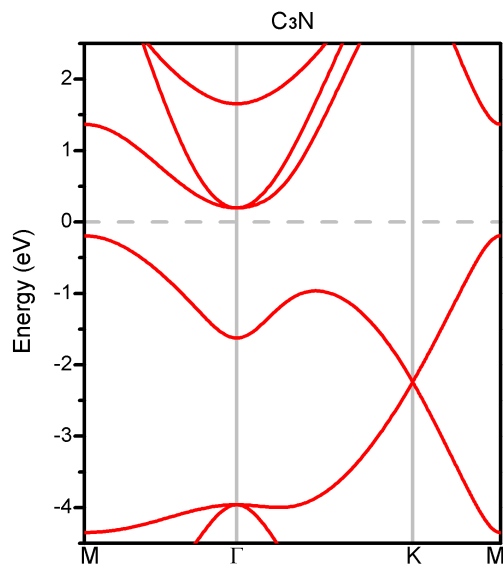


Fig. 4.3 Band structure of C₃N monolayer from DFT (PBE) calculations.

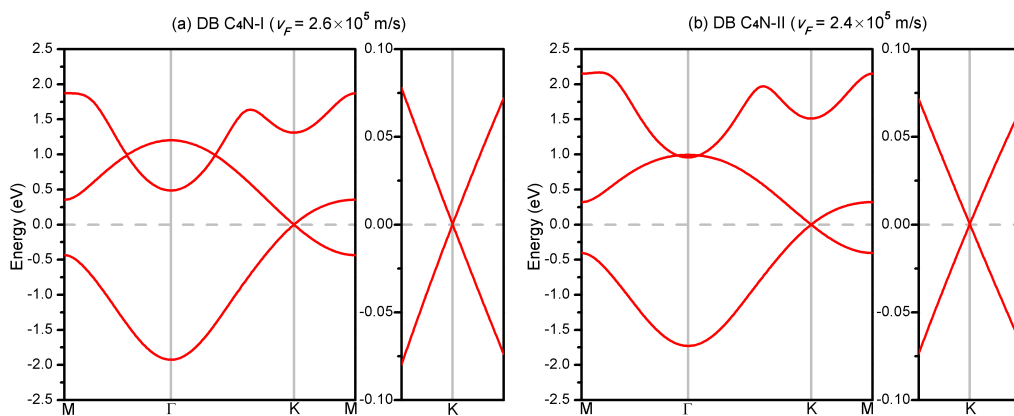


Fig. 4.4 Band structures of DB C₄N-I (a) and DB C₄N-II (b) monolayers from DFT (PBE) calculations. v_F is the Fermi velocity of the Dirac cone. The energy at the Fermi level was set to zero. An enlarged view of the band lines at the K point near the Fermi level is presented to the right of the figures.

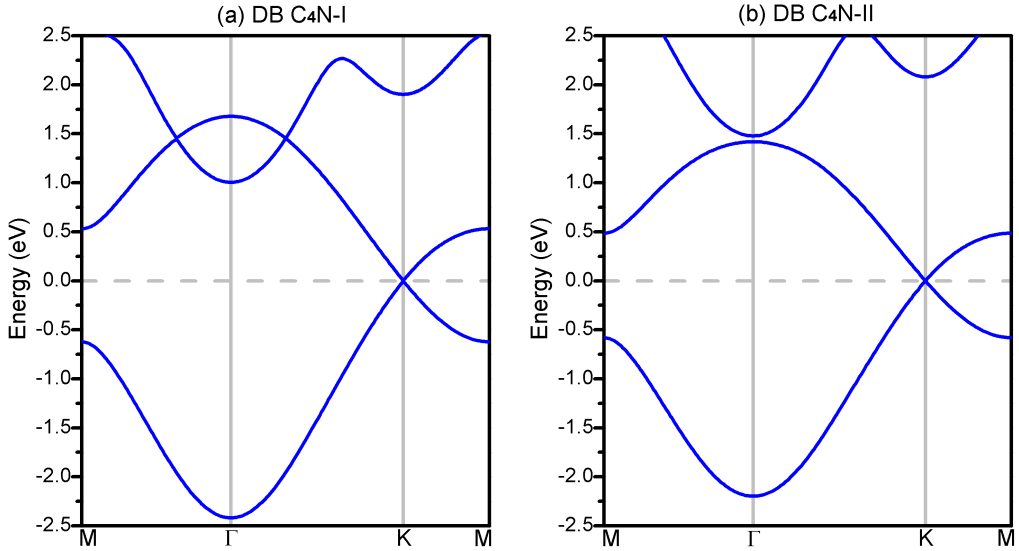


Fig. 4.5 Band structures of DB C₄N-I (a) and DB C₄N-II (b) monolayers from HSE calculations.

only the p_z orbitals of eight out of twenty C atoms in the unit cell are responsible for the formation of the Dirac cone [230], not all ten atoms in the unit cell of the DB C₄N contribute to the Dirac cone. Only the two C_R and the two N atoms play an important role in the formation of the Dirac cone, which is clearly shown in the corresponding Kohn-Sham wave functions at the Dirac point (Fig. 4.6(a) and (b)).

We also investigated the SOC effect on the band structures of the DB C₄N monolayers. For the DB C₄N monolayers, the SOC effect is very small with a band gap at the K point below 0.25 meV. This will be difficult to be detected in a real experiment because of the possible presence of disorder. We can understand the weak SOC effect from two aspects. First, the SOC effect is related to the element type: the heavier the element, the more pronounced the SOC effect becomes. Structures including heavy elements, such as Bi, can have a large SOC effect [231, 175]. Second, the SOC effect is also related to the atomic orbitals forming the Dirac cone. For the g-C₆N₆ monolayer, the SOC band gap of the Dirac cone at the K point (below the Fermi level) can reach 5.50 meV [216]. In this case the Dirac cone is formed by the p_x and p_y atomic orbitals of the N atoms and the SOC gap originates directly from the onsite term. According to the PDOS and the corresponding Kohn-Sham wave functions of the Dirac point, the four p_z atomic orbitals of the C_R and N atoms in the DB C₄N are responsible for the formation of the Dirac cone, which is the main reason for the weak SOC effect. The band gap values of the DB

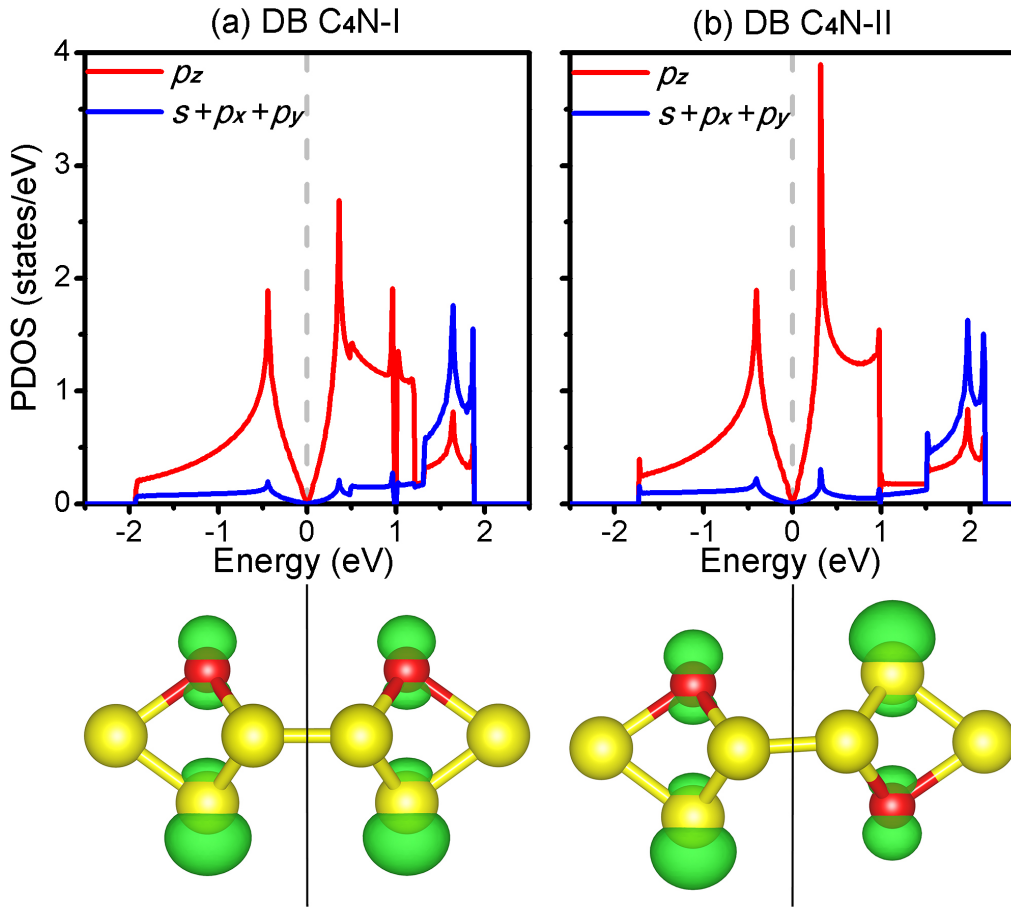


Fig. 4.6 The PDOS for the summed states of the s , p_x , and p_y/p_z atomic orbitals of all the atoms in the unit cell and the corresponding Kohn-Sham wave functions at the Dirac points ((a) DB C₄N-I and (b) DB C₄N-II). The isosurface values of the Kohn-Sham wave functions were set to 0.02 \AA^{-3} .

C_4N monolayers are between the 0.0008 meV of graphene [199] and the 0.59 meV of -graphyne [128], where the Dirac cones are formed by the p_z atomic orbitals of the C atoms. Since SOC opens up a small band gap at the Dirac cone and SOC effect is more obvious in DB C_4N -II than that in DB C_4N -I, we investigated the topological properties of the DB C_4N -II. Due to the inversion symmetry of the DB C_4N -II structure, the work of Fu and Kane showed that the inversion symmetry can simplify the calculations of the Z_2 topological invariant (ν), which can be determined from the knowledge of the parity eigenvalues for the occupied states at the time-reversal invariant points in the BZ [232]. For the DB C_4N -II monolayer, there are four time-reversal invariant points: one Γ point and three M points. The parity eigenvalue is -1 at the Γ point and $+1$ at the three M points, which indicates a nontrivial topological invariant, $\nu = 1$. This shows that the DB C_4N -II is a 2D topological insulator.

4.3.4 TB Model

Although the two C_R and the two N atoms all contribute to the Dirac cone, it is clear that the Kohn-Sham wave functions of the C_R atoms are much larger than those of the N atoms for both DB C_4N monolayers (Fig. 4.6). We can understand the origin of the Dirac cone from a simple TB model by only including the p_z atomic orbitals of the two C_R atoms without the two N atoms. The two DB C_4N monolayers can be regarded as to consist of two C_R atoms in one unit cell. Setting \vec{a}_1 and \vec{a}_2 as the primitive vectors, the positions of the two C_R atoms in the xy plane can be expressed as $1/3 \times (\vec{a}_1 + \vec{a}_2)$ and $2/3 \times (\vec{a}_1 + \vec{a}_2)$, similar to graphene/silicene. The DB C_4N -I can be regarded as a graphene structure because the two C_R atoms are in the same xy plane while the DB C_4N -II can be regarded as a silicene structure due to the buckling along the z axis between the two C_R atoms. The two C_R atoms in the unit cell can be labeled as A and B atoms. The TB Hamiltonian that describes the electronic structure near the Fermi level of such a system can be written as [187, 233],

$$H = \begin{pmatrix} \varepsilon & \hbar v_F(k_x - ik_y) \\ \hbar v_F(k_x + ik_y) & -\varepsilon \end{pmatrix} \quad (4.1)$$

where k is the wave vector relative to the Dirac point and v_F is the Fermi velocity. Similar to graphene/silicene, the difference of the onsite energy between the two C_R atoms is zero ($\varepsilon = 0$) because they have the same chemical environment [183, 234]. Thus we obtain a

linear dispersion relation $E = \pm\hbar|k|$, which is the origin of the Dirac cone. Although the above simple model leads to a direct understanding of the Dirac cone, the two N atoms still have contributions in the formation of the Dirac cone. We further confirm these results by a TB model including the p_z atomic orbitals of the two C_R and two N atoms in the unit cell [230]. We resorted to maximally localized Wannier functions (MLWFs) [235] using the Wannier90 code [236]. Starting from the bands of the first-principles calculations, we used the four p_z atomic orbitals of the C_R and N atoms. Minimizing the MLWF spread, the band structures obtained using the Wannier90 interpolation method and the DFT calculations are in excellent agreement, as shown in Fig. 4.7.

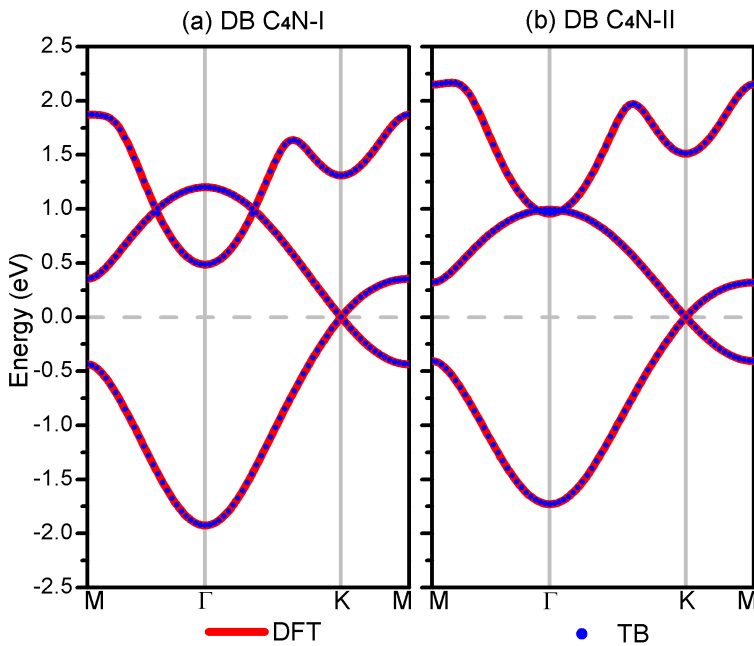


Fig. 4.7 Band structures of DB C₄N-I (a) and DB C₄N-II (b) from DFT (PBE) and TB calculations. The red lines represent the results of DFT calculations and the blue dotted lines represent the results of TB calculations.

4.3.5 Synthesis and Application

At last, we comment on the possible routes for synthesizing the DB C₄N monolayers and their applications. It is noteworthy that the carbon self-doped g-C₃N₄ has been achieved experimentally, which can increase the C : N value [237]. Although the synthetic route of the substitution pattern is different from that of the adsorption pattern, under carbon-

rich environment, we expect that the C atoms can be adsorbed on C_3N forming DB C_4N monolayer, because it is almost barrierless as atomic carbon resources are supplied [224, 238]. Similar to graphene or other 2D Dirac materials [239], the band structures of the two monolayers have a zero band gap, which will limit their applications in high-speed electronic devices. Many theoretical methods have been proposed to open a band gap in graphene. Among them, hydrogenated graphene has been achieved in experiment [240]. We also investigated the hydrogenation of the proposed DB C_4N by the adsorption of an H atom on each C_R atom. In this way, we obtain two hydrogenated DB C_4N monolayers (DB C_4NH -I and DB C_4NH -II). Their band structures are shown in Fig. 4.8. It is clear that a band gap can be opened close to the Fermi level, which is beneficial for the applications in electronic devices and other aspects [241].

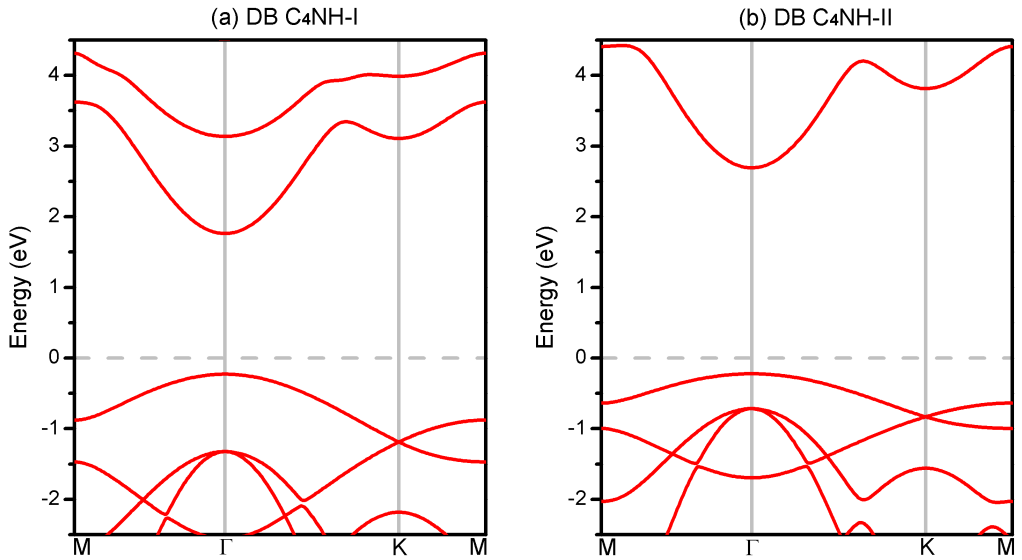


Fig. 4.8 Band structures of DB C_4NH -I (a) and DB C_4NH -II (b) monolayers from DFT (PBE) calculations. On each C_R atom, an H atom is adsorbed. The direction of the $CR-H$ bond is parallel to the z axis.

4.4 Conclusion

In summary, using first-principles calculations, we predict the first Dirac carbon nitride monolayers without spin-polarization. In contrast to the existing 2D carbon nitride materials that have been realized in experiments, they have a dumbbell structure and all the C and N atoms are sp^3 -hybridized. Their formation energies compared to C_3N and

the phonon calculations fully confirm their energetic and dynamical stability. The Dirac cone band structure and large Fermi velocity are comparable to graphene and make the DB C₄N monolayers promising materials for high-speed electronic devices. A simple TB model was constructed in order to understand the origin of the Dirac cone which is helpful for further investigations of the massless Dirac fermions. The here proposed DB C₄N monolayer structures provide a new way to search for Dirac cone band structures in 2D group IV-V elemental materials.

Chapter 5

Bi-Based Topological Insulators: GaBi-X₂ (X = I, Br, Cl)

¹Quantum Spin Hall (QSH) insulators with a large topologically nontrivial bulk gap are crucial for future applications of the QSH effect. Among these, group III-V monolayers and their halides with a chair structure (regular hexagonal framework, RHF) were widely studied. Using first-principles calculations, we propose a new structure model for the functionalized group III-V monolayers, which consist of rectangular GaBi-X₂ (X = I, Br, Cl) monolayers with a distorted hexagonal framework (DHF). These structures have a much lower energy than the GaBi-X₂ monolayers with a chair structure. Remarkably, the DHF GaBi-X₂ monolayers are all QSH insulators, which exhibit sizeable nontrivial band gaps ranging from 0.17 eV to 0.39 eV. Those band gaps can be widely tuned by applying different spin-orbit coupling (SOC) strengths, resulting in a distorted Dirac cone.

5.1 Introduction

Monolayer graphene was first realized in 2004 and since then two-dimensional (2D) materials play a crucial role in the field of nanomaterials [2]. In the meantime, more and more 2D materials with unusual electronic and spintronic properties have been synthesized, that are promising for applications in quantum devices. For example, the group IV element monolayers, silicene [242–244, 189, 190, 245, 191, 246, 247, 192, 248, 193], germanene [249–251, 194], and stanene [197] were all successfully synthesized on differ-

¹The results of this chapter were published as: L. Li, O. Leenaerts, X. Kong, X. Chen, M. Zhao, and F. M. Peeters, *Nano Research* **10**, 2168 (2017).

ent substrates. Besides graphene and its analogs, layered transition-metal dichalcogenides (TMDs) are another family of 2D materials that have been realized experimentally [252–254]. All these 2D materials can be regarded as being composed of a regular hexagonal framework (RHF), which is usually called the chair structure. Most predictions of new 2D materials are also based on the RHF model, such as the silicon-germanium monolayer [255], HgSe/HgTe monolayer [256], III-Bi monolayer [257], and organic metal frameworks [258–261]. A natural question arises: Can we find other stable structure models for those 2D materials?

Quantum spin Hall (QSH) insulators are another important set of 2D materials [262, 263, 48]. The QSH effect has been observed in HgTe/CdTe and InAs/GaSb quantum wells [264, 55, 265], but the operating temperature is limited due to their small bulk gap arising from weak spin-orbit coupling (SOC). The necessary low temperature also limits its applications. For the synthesis of the QSH insulators with a large gap, Bi (111) bilayer has been realized in experiment and its time-reversal symmetry-protected edge states have been observed, but there is still experimental discrepancy regarding its topological nature [88, 266, 267]. Therefore, searching for newer QSH insulators with a large bulk gap will provide more choices for experiment and application. Starting from graphene [268], many kinds of QSH insulators have been predicted, including graphene with a sandwich structure [269, 270], silicene (germanene/stanene) with RHF [198, 199], stanene with a dumbbell structure [200, 271, 203], MoS₂ allotropes [272, 273, 232, 274–277], and monolayers containing heavy metal atoms (Bi/Sb/Hf) [257, 278–281]. In the case of particular substrates [282], applying an external field [283], or using hydrogenation/functionalization [284–298, 231, 299–302], the size of those nontrivial bulk gaps can be further increased. Currently, the largest nontrivial bulk gap is 1.0 eV found in Bi₂F₂ monolayer [284, 285], which shows that chemical functionalization is a very powerful way to obtain a large nontrivial bulk gap. Using first-principles calculations, some group III-V monolayers were predicted to be QSH insulators with a large bulk gap [257] and it was found that this gap can be enlarged via hydrogenation/functionalization [296–298, 231, 299–302]. After functionalization, their structures can all be regarded as being composed of RHF. However, similar as the different ways of functionalization of graphene, one may ask if there are other ways of functionalization of group III-V monolayers that simultaneously retain their topologically nontrivial properties?

In order to tackle the above questions, we propose a new functionalization model, called distorted hexagonal framework (DHF), for iodization, bromization, and chloriza-

tion of gallium bismuth monolayer (GaBi-X_2 , $X=\text{I, Br, Cl}$). We find that the ground state energy of the DHF GaBi-X_2 monolayers is less than that of the RHF GaBi-X_2 monolayers, which were widely studied in previous works [296–298, 231, 299–302]. Using first-principles calculations, we investigated systematically the structure, stability and electronic property of the DHF GaBi-X_2 monolayers. The GaBi framework is robust against different ways of functionalization for the three DHF GaBi-X_2 monolayers. Phonon spectra provide convincing evidence for the thermal and dynamical stabilities of those DHF GaBi-X_2 monolayers. Remarkably, we find a distorted Dirac cone in the band structure without SOC of the DHF GaBi-I_2 monolayer and a large nontrivial bulk gap (0.39 eV) in the band structure with SOC, which is large enough to achieve the QSH effect at room-temperature. Both GaBi-Br_2 and GaBi-Cl_2 have indirect band gaps without and with SOC. However, we find that a distorted Dirac cone appears when changing the strength of the SOC. Furthermore, the topologically nontrivial property of the bulk gaps is confirmed by the nonzero Z_2 topological invariant and the appearance of a gapless Dirac state from the edges.

5.2 Calculation Method

Our first-principles calculations were performed using the Vienna *ab initio* simulation package (VASP) code [100, 101], implementing density functional theory (DFT). The ion-electron interactions were described using projector-augmented-wave potentials (PAW) [102]. The electron exchange-correlation functional was treated by using the generalized gradient approximation (GGA) in the form proposed by Perdew, Burke, and Ernzerhof (PBE) [153]. For the 2D structure relaxation, the Brillouin zone (BZ) was sampled by using a $11 \times 11 \times 1$ Γ -centered Monkhorst-Pack grid, while a $15 \times 15 \times 1$ grid was used for the static calculations. A $1 \times 11 \times 1$ grid was used for the nanoribbon calculations. The vacuum space was set to at least 15 Å in all the calculations to minimize artificial interactions between neighboring slabs. Other settings of calculation are the same to Chapter 3.2. SOC was included by a second variational procedure on a fully self-consistent basis. The phonon spectra were calculated using a supercell approach within the PHONON code [303].

As our systems preserve time-reversal symmetry and break space-inversion symmetry, we can obtain the Z_2 topological invariant by calculating Wannier Charge Centers (WCCs) [113]. In the concept of time-reversal polarization [304], the integer Z_2 invariant (Δ) can

be written as

$$\Delta = p_{\theta}(T/2) - p_{\theta}(0) \bmod 2, \quad (5.1)$$

where $p_{\theta}(t)$ is the total charge polarization with the cyclic parameter t and T is the period of cyclic adiabatic evolution. The above equation can be rewritten in terms of WCCs (\bar{x}_{α}):

$$\Delta = \sum_{\alpha} [\bar{x}_{\alpha}^I(T/2) - \bar{x}_{\alpha}^{II}(T/2)] - \sum_{\alpha} [\bar{x}_{\alpha}^I(0) - \bar{x}_{\alpha}^{II}(0)], \quad (5.2)$$

where I and II indicate the Kramers pairs. In explicit numerical implementations, a more straightforward and more easily automated approach is to track the largest gap in the spectrum of the WCCs. Let Δ_m be the number of WCCs that appear between neighboring gap centers and M is the total number of changes in Δ_m . The Z_2 invariant is then given by:

$$\Delta = \sum_{m=0}^M \Delta_m \bmod 2, \quad (5.3)$$

Therefore, the Z_2 invariants can be obtained easily by numerical computations with *ab initio* codes together with the Wannier90 code [235, 236].

5.3 Results and Discussion

5.3.1 Geometrical Structure

The three investigated DHF GaBi-X₂ monolayers exhibit a similar structure. Fig. 5.1(a) and (b) show the optimized geometrical structure of the DHF GaBi-X₂. From the top view, the framework of GaBi is DHF, which is totally different from the previous chair models [296–298, 231, 299–302], which are RHF with a three-fold rotation symmetry like silicene/germanene [198, 199], as shown in Fig. 5.1(c) and (d). To obtain the DHF structure, we used a larger rectangular supercell and moved the X atoms from their original location, which is right on top of the Ga/Bi atoms. The fully optimized DHF GaBi-X₂ monolayer shows a high symmetric space group of $Pca2_1$. We choose a rectangular primitive cell with lattice constants a along the x direction and b along the y direction. Without loss of generality, we can take the DHF GaBi-I₂ monolayer as an example. Its lattice constants are $a = 8.58 \text{ \AA}$ and $b = 8.14 \text{ \AA}$. Considering the Ga–Bi bonds, there are three kinds of bonds with different lengths, which is totally different from the RHF GaBi-I₂ monolayer. For the direction along y, the length of the Ga–Bi bond is labeled as

L1, which is equal to 2.91 Å. For the direction along x , the lengths of the Ga-Bi bonds are labeled as L2 and L3, respectively, as shown in Fig. 5.1(a). L2 is equal to 2.95 Å and L3 is equal to 2.80 Å. L2 and L3 alternate along the x direction. The different lengths of the Ga-Bi bonds lead to the DHF, while the lengths of L1, L2 and L3 are the same in the RHF (Fig. 5.1(c)). For the RHF GaBi-I₂ monolayer, all the I atoms are right on the Ga/Bi atoms along the z direction forming a chair configuration (Fig. 5.1(d)), but in the DHF GaBi-I₂ monolayer, the bonds of Ga-I and Bi-I are totally different. For Bi-I bonds, one I atom forms a bond with two Bi atoms and the lengths of the two Bi-I bonds can be labeled as M1 and M2. Along the x direction, M1 and M2 alternate, similar to L2 and L3. For Ga-I bonds, labeled as N (Fig. 5.1(b)), the I atom is not right on top of a Ga atom along the z direction, but there is a little deviation between them. For the three DHF GaBi-X₂ monolayers, the optimized geometrical structure data are summarized in Table 5.1. From iodization to chlorization, the lattice constants (a and b) diminish slightly and the lengths of M1, M2, and N also decrease, but the lengths of the three Ga-Bi bonds (L1, L2, and L3) remain almost unchanged.

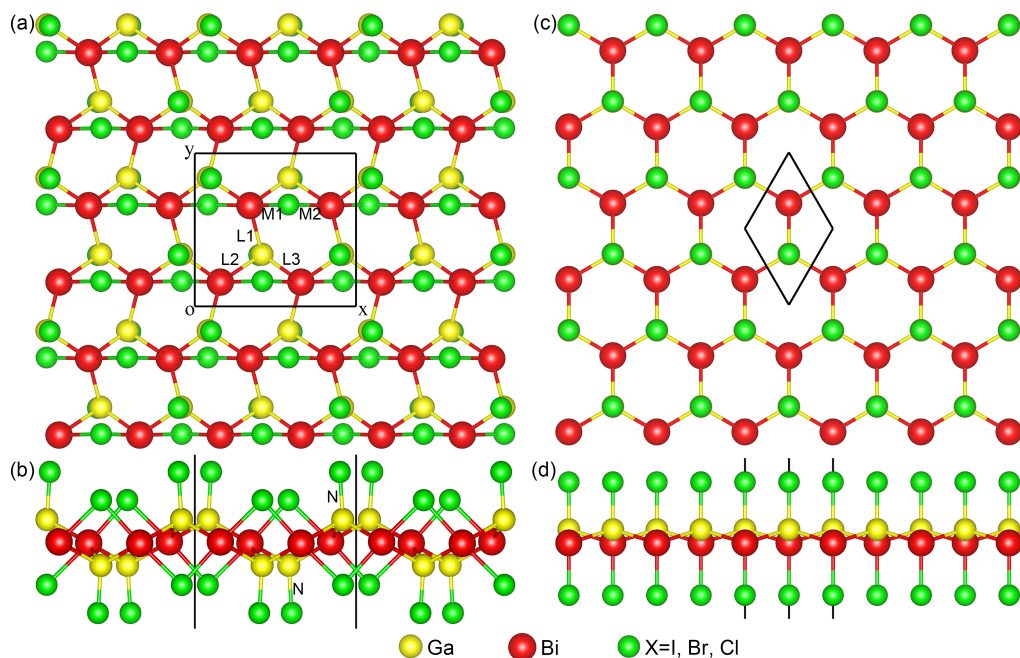


Fig. 5.1 Top view (a) and side view (b) of the DHF GaBi-X₂. Top view (c) and side view (d) of the RHF GaBi-X₂.

Table 5.1 Structure parameters and relative energies of the DHF GaBi-X₂ monolayers. a and b are the lattice constants. L1, L2, and L3 are the three lengths of the Ga–Bi bonds. M1 and M2 correspond to the two lengths of the Bi-X bonds and N is the length of the Ga–X bond. The relative formation energy ΔE is obtained with respect to the energy of the RHF GaBi-X₂ monolayer. Z_2 is the topological invariant.

GaBi-X ₂	a/b (Å)	L1/L2/L3/M1/M2/N (Å)	ΔE (meV/atom)	Z_2
GaBi-I ₂	8.58/8.14	2.91/2.95/2.80/3.08/3.15/2.54	−49	1
GaBi-Br ₂	8.36/8.03	2.89/2.95/2.79/2.88/2.95/2.32	−55	1
GaBi-Cl ₂	8.22/8.00	2.89/2.95/2.79/2.73/2.79/2.17	−57	1

5.3.2 Energy and Stability

We compare the energies of the RHF GaBi-X₂ monolayers, that have been investigated in previous studies [296–298, 231, 299–302], with those of the newly proposed DHF GaBi-X₂ monolayers. We set the energy of RHF GaBi-X₂ as 0 and then calculated the relative formation energy of DHF GaBi-X₂, which we show in Table 5.1. The DHF GaBi-X₂ monolayers all have a substantially lower energy. The RHF GaBi-X₂ monolayers exhibit a polarized structure due to the up-down asymmetry, which increases their energy and probably will lead to a curled configuration. In comparison, the DHF GaBi-X₂ has no dipole moment. The above two aspects are responsible for the superiority in the structural stability of the DHF GaBi-X₂ over the RHF GaBi-X₂. To investigate the dynamical stability of DHF GaBi-X₂ monolayers, we calculated their phonon spectra and show them in Fig. 5.2. It is clear that the DHF GaBi-X₂ monolayers are all free from imaginary frequency modes and are therefore dynamically stable.

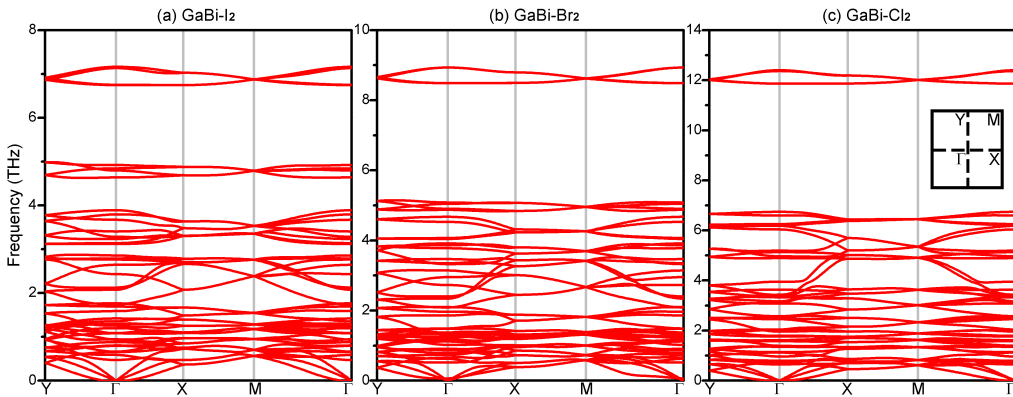


Fig. 5.2 Phonon spectra of the DHF GaBi-X₂ monolayers along the high-symmetry points in the BZ.

It should be noted that although there are some experiments on GaBi(As) [305, 306], InBi [307] and TlBi [308] films, the experimental support for their functionalization is still missing, similar to the experimental absence of other functionalized monolayers (e.g. functionalized Bi and Pb monolayers) [88]. Regarding experimental realization, we suggest obtaining the GaBi monolayer first and then synthesize the GaBi- X_2 monolayers through functionalization. Another possible chemical route is as follows. Taking the DHF GaBi-I₂ monolayer as an example, it could be synthesized by: BiI_3 [309, 310] + GaI_3 [311–313] + $4\text{Na} \rightarrow \text{GaBi-I}_2$ (DHF) + 4NaI . Our DFT calculations show that the reaction is exothermic with an energy release of 0.6 eV/atom, which indicates its feasibility for experimental synthesis.

5.3.3 Electronic Band Structure

The electronic band structures of the RHF GaBi- X_2 monolayers are topologically non-trivial and show a relatively larger bulk gap due to the strong SOC at the Γ point [296–298, 231, 299–302]. The electronic band structures of the DHF GaBi-I₂ monolayer obtained from DFT are plotted in Fig. 5.3. For the DHF GaBi-I₂ monolayer, the valence and conduction bands meet at a single point along the Γ -X line, giving rise to a distorted Dirac cone, as shown in Fig. 5.3(a). To further confirm the Dirac cone band structure, we calculated the total density of states (DOS), as shown in Fig. 5.4. It is clear that the DOS are 0 at the Fermi level. Similar band structures can also be found in other rectangular lattices [123, 314]. The orbital-projected band structure without SOC of the DHF GaBi-I₂ monolayer close to the Fermi level is shown in Fig. 5.5(a). It is clearly seen that the distorted Dirac cone mainly comes from the atomic orbitals of the Ga and Bi atoms. For the crossing bands forming the Dirac cone, one band comes from the p_y atomic orbitals (green dots) and the other originates from the s , p_x , and p_z atomic orbitals (red dots). The band structure with SOC for the DHF GaBi-I₂ monolayer shows an indirect band gap (Fig. 5.3(b)). The indirect band gap is 0.39 eV along the Γ -X line, which is less than that of the RHF GaBi-I₂ monolayer (0.606 eV) [299]. From its corresponding orbital-projected band structure close to the Fermi level (Fig. 5.5(b)), we find that these bands are mainly due to the s and p atomic orbitals of the Ga and Bi atoms. We now focus on the valence and conduction bands along the Γ -X line. The orbital contributions can be divided into two parts. The first part of the valence band corresponds to the s , p_x , and p_z orbitals (red dots) and the second part comes from the p_y orbitals (green dots). The

situation of the conduction band is the opposite. However, previous studies of the RHF GaBi-X₂ monolayer showed that the orbital contributions of the bands close to the Fermi level are mainly from the s , p_x , and p_y without p_z [296–298, 231, 299–302]. We may conclude that the p_z orbital contributions are due to the partial hybridization between the p_z orbitals and the X atomic orbitals, which comes from the deviations along the x direction between the X atoms and the Ga/Bi atoms. It is noteworthy that the spin degeneracy is lifted due to the asymmetric geometric structure. Such spin-splitting effect has also been found in III-Bi [257], hydrogenated/functionalized III-Bi [296–298, 231, 299, 300], and g-TIA (A = N, P, As and Sb) [278] monolayers. This lifting of spin degeneracy is due to spin-orbit interaction and results in terms linear in electron wave vector k in the effective Hamiltonian. The origin of these terms linear in low-dimensional systems is structure and bulk inversion asymmetry which lead to Rashba and Dresselhaus spin-orbit terms in the Hamiltonian, respectively [315–318]. It is well known that spin-splitting of Rashba states in a two-dimensional electron system provide a promising mechanism for spin manipulation that is needed in spintronics applications [319].

In contrast to the gapless band structure of the DHF GaBi-I₂ monolayer, the band structure without SOC of the DHF GaBi-Br₂ monolayer shows semiconducting behavior. The indirect band gap is 0.13 eV without SOC (Fig. 5.3(c)) while it becomes 0.30 eV with SOC (Fig. 5.3(d)), which is less than that of the RHF GaBi-Br₂ (0.628 eV) [299]. From the corresponding orbital-projected band structures close to the Fermi level (Fig. 5.5(c) and (d)), we find that those bands result from the s and p atomic orbitals of the Ga and Bi atoms. They are similar to the band structure with SOC of the DHF GaBi-I₂, which can also be divided into two parts. The SOC band structure also shows obvious spin-splitting of Rashba states. The band structures without and with SOC of the DHF GaBi-Cl₂ monolayer are shown in Fig. 5.6(a) and (c) and are similar to those of the DHF GaBi-Br₂. An indirect band gap of 0.22 eV (0.17eV) is found without (with) SOC. The band gap with SOC is much less than that of the RHF GaBi-Cl₂ monolayer, which was found to be 0.645eV [299].

5.3.4 Topologically Nontrivial Property

Similar to the band structures of graphene (silicene, germanene, and stanene) [268, 198, 199] and other 2D topological insulators, the DHF GaBi-I₂ monolayer also has a Dirac cone in its band structure without SOC, which is an important sign of a QSH

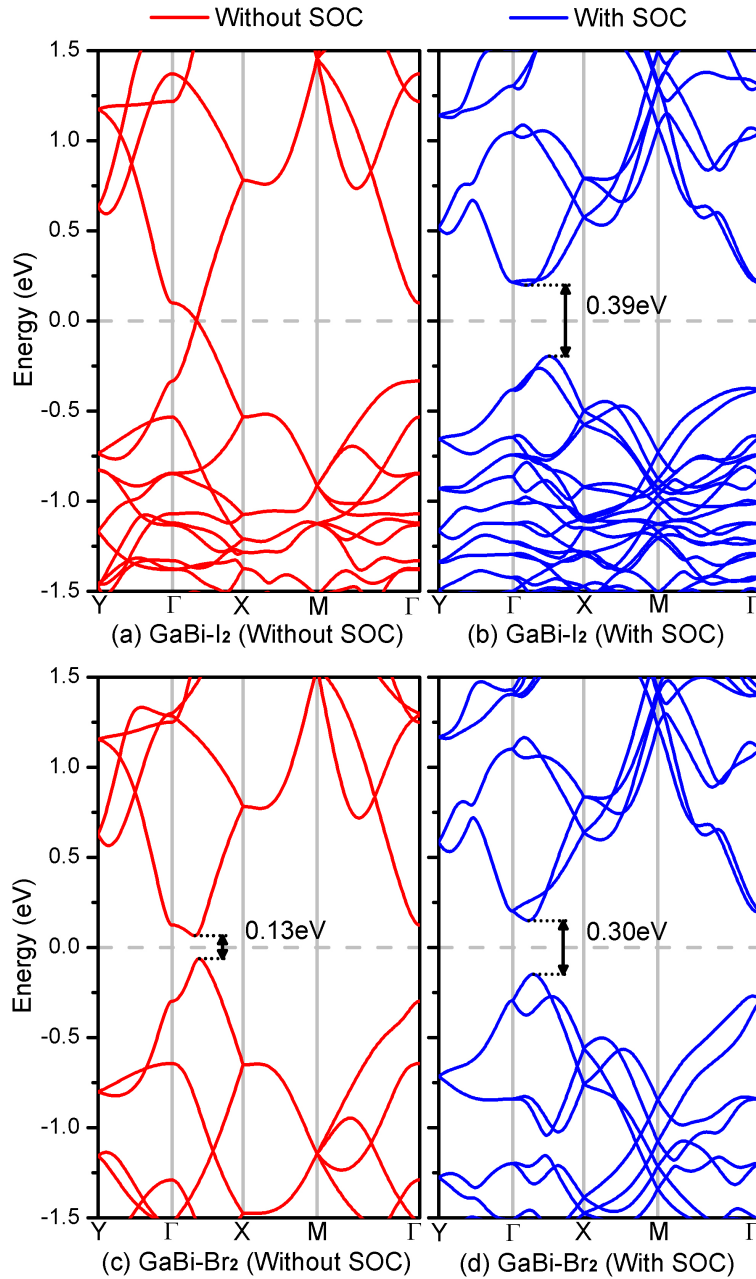


Fig. 5.3 Band structure of the DHF GaBi-I₂ and GaBi-Br₂ monolayers without and with SOC from DFT calculations. (a) GaBi-I₂ without SOC, (b) GaBi-I₂ with SOC, (c) GaBi-Br₂ without SOC, and (d) GaBi-Br₂ with SOC.

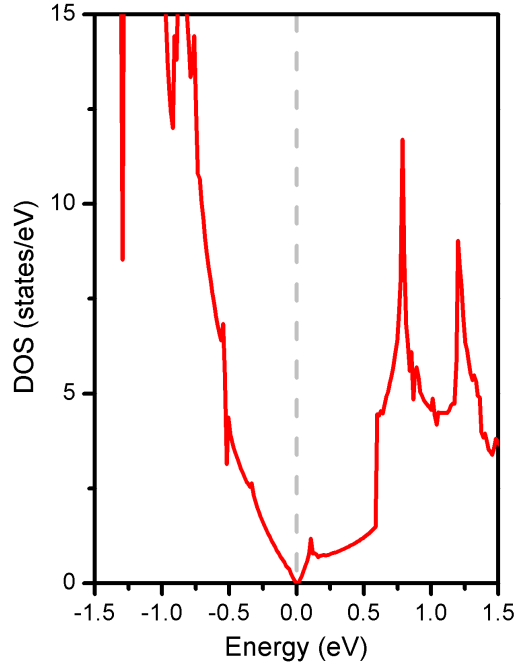


Fig. 5.4 DOS of the DHF GaBi-I₂ monolayer without SOC.

insulator [198, 199, 320, 321] and a large SOC bulk gap in its band structure with SOC. To confirm the topologically nontrivial property of the bulk gap, we calculated its Z_2 topological invariant (see Table 5.1), which is equal to 1. This indicates that the DHF GaBi-I₂ monolayer is a 2D topological insulator. For the DHF GaBi-Br₂ and GaBi-Cl₂ monolayers, we also calculated the Z_2 topological invariant (see Table 5.1). We find that the Z_2 topological invariant is 1 in both cases, although there are no Dirac cones in their band structures without SOC. To find the Dirac cone, we applied different SOC strengths (λ_{SOC}) [320, 321] and calculated the corresponding band gaps of the DHF GaBi-Br₂ (Fig. 5.7(a)). The band gap decreases with increasing λ_{SOC} at the beginning. When λ_{SOC} reaches 0.24, a gapless state can be found. Then the band gap increases with increasing λ_{SOC} . We plot the band structure for $\lambda_{\text{SOC}} = 0.24$ (Fig. 5.7(b)) and a distorted Dirac cone can be seen. From its corresponding orbital-projected band structure close to the Fermi level along the Γ -X line (Fig. 5.7(c)), it is seen that the crossing bands forming the distorted Dirac cone arise from the s and p atomic orbitals of the Ga and Bi atoms, similar to the case of the DHF GaBi-I₂ monolayer. For some QSH insulators, such as GaBi monolayer [257] and tetragonal Bi bilayer [320], the topological phase transition results from a band inversion when the band gap at the Γ point closes and reopens in the

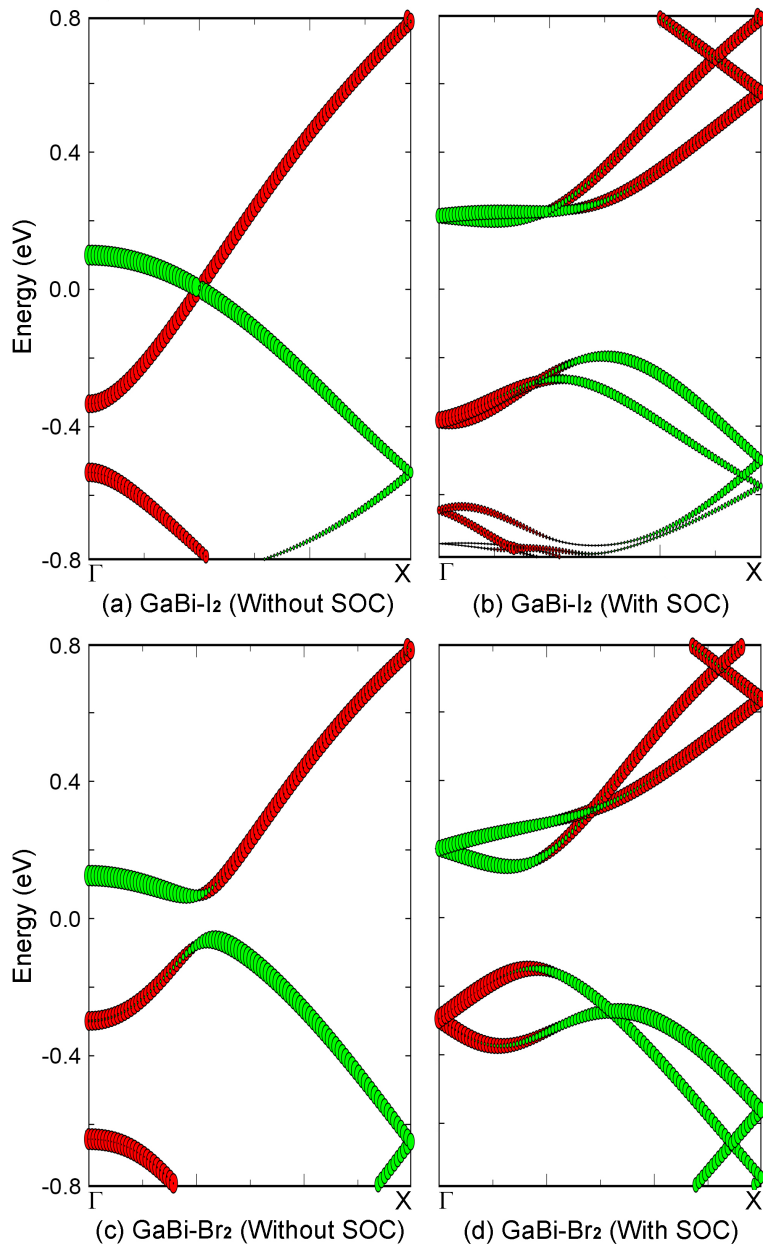


Fig. 5.5 Orbital-projected band structure close to the Fermi level without and with SOC along the Γ -X line. (a) GaBi-I₂ without SOC, (b) GaBi-I₂ with SOC, (c) GaBi-Br₂ without SOC, and (d) GaBi-Br₂ with SOC. The red dots represent the contributions from the s , p_x , and p_z atomic orbitals of the Ga and Bi atoms and the green dots represent contributions from the p_y atomic orbitals of the Ga and Bi atoms.

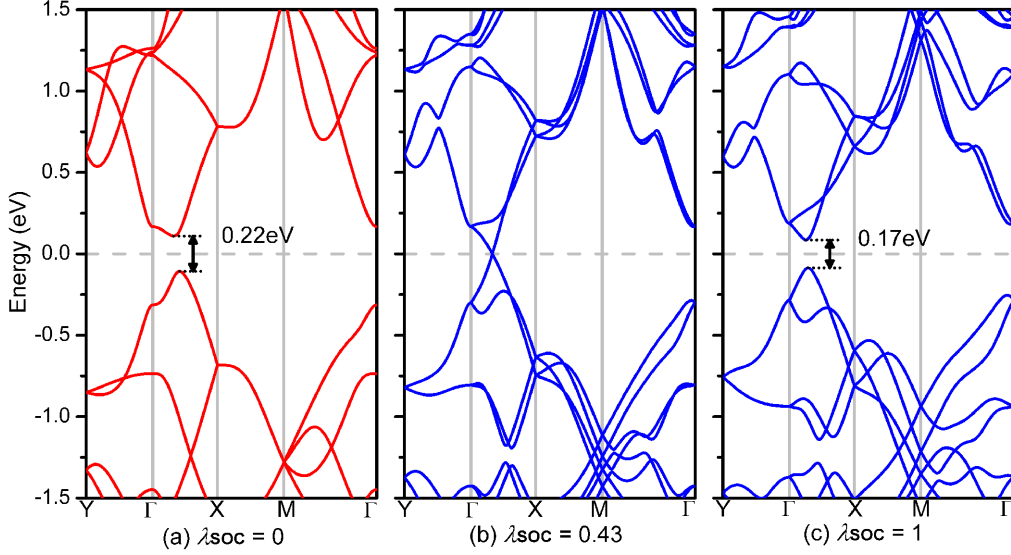


Fig. 5.6 Band structure of the DHF GaBi- Cl_2 monolayer for $\lambda_{SOC} = 0$ (a), $\lambda_{SOC} = 0.43$ (b), and $\lambda_{SOC} = 1$ (c).

process of changing the SOC strength. In our case, however, there is no band inversion at the Γ point. In changing the λ_{SOC} from 0 to 1 for the DHF GaBi- Br_2 , the Z_2 topological invariant is 0 before the gap closes at a point along the Γ -X line while it becomes 1 after the gapless state. This topological phase transition is similar as the case of stanene with an effective electric field (substrate) [322], where the competition between the trivial band gap introduced by the effective electric field and the SOC band gap can lead to a change of Z_2 and a topological phase transition. Here, the functionalized elements are equal to a build-in electric field and the Dirac cone is an important sign of a topological phase transition. For the DHF GaBi- Cl_2 monolayer, we find a similar distorted Dirac cone when λ_{SOC} is equal to 0.43 (Fig. 5.6(b)).

Although iodization, bromization, and chlorization of GaBi lead to qualitatively similar bands close to the Fermi level that arise from the atomic orbitals of the Ga and Bi atoms, their band gaps are totally different. We conclude that the different functionalized elements lead to different build-in electric fields, and then change the effective mass terms, which can influence the band gaps [231]. For the DHF GaBi- X_2 monolayer, we only find the Dirac cone for a particular λ_{SOC} and if we tune the λ_{SOC} or change the calculation method, the Dirac cone will disappear. It can be seen that the Dirac cone of the DHF GaBi- I_2 disappears for $\lambda_{SOC} = 0$, when we use the more sophisticated Heyd-Scuseria-Ernzerhof (HSE06) [97, 98] hybrid functional method (Fig. 5.8). With HSE, the

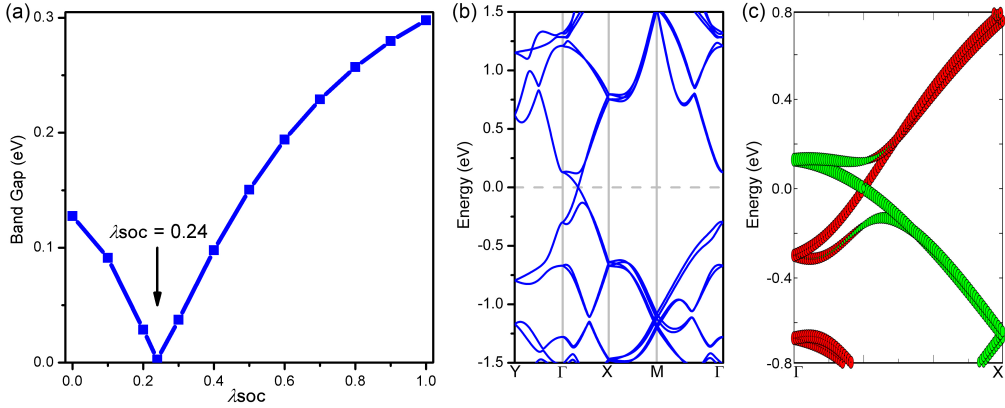


Fig. 5.7 (a) Variation of the DHF GaBi-Br₂ band gap as a function of SOC strength λ_{SOC} . (b) Band structure of the DHF GaBi-Br₂ for $\lambda_{\text{SOC}} = 0.24$. (c) Orbital-projected band structure for $\lambda_{\text{SOC}} = 0.24$ close to the Fermi level along the Γ -X line. The red dots represent the contributions from the s , p_x , and p_z atomic orbitals of the Ga and Bi atoms and the green dots represent contributions from the p_y atomic orbitals of the Ga and Bi atoms.

band gap including SOC is 0.47 eV (Fig. 5.8(b)), which is a little larger than the 0.39 eV from PBE calculations. For the HSE without SOC, a small band gap (0.05 eV) is opened (Fig. 5.8(a)), which is different from the Dirac cone of the PBE result. Similar to the band structures of the GaBi-Br₂ and GaBi-Cl₂ monolayers, the appearance of the DHF GaBi-I₂ Dirac cone in the HSE calculations will show up for a particular λ_{SOC} between 0 and 1 [320]. It is certain that we can always find Dirac cones for the three DHF GaBi-X₂ monolayers when varying λ_{SOC} from 0 to 1, but we can't find a Dirac cone for the DHF GaBi-F₂ monolayer. Its band gap ranges from 0.32 eV ($\lambda_{\text{SOC}} = 0$) to 0.03 eV ($\lambda_{\text{SOC}} = 1$) (Fig. 5.9) and no gapless state is found in the process. Corresponding to the absence of a Dirac cone, its Z_2 topological invariant is equal to 0, which indicates that the DHF GaBi-F₂ monolayer is a trivial insulator.

Besides the nonzero Z_2 topological invariant, the existence of gapless edge states is another prominent feature of QSH insulators. Since the DHF GaBi-Br₂ and GaBi-Cl₂ monolayers show a similar band structure, without loss of generality, we only considered the DHF GaBi-I₂ and GaBi-Br₂ nanoribbons with armchair edges. The nanoribbon structure is shown in Fig. 5.10(a) and their widths (W) are wide enough to avoid interactions between the edge states from the two sides. The band structures of the DHF GaBi-I₂ and GaBi-Br₂ nanoribbons are shown in Fig. 5.10(b) and (c), respectively. We can see that

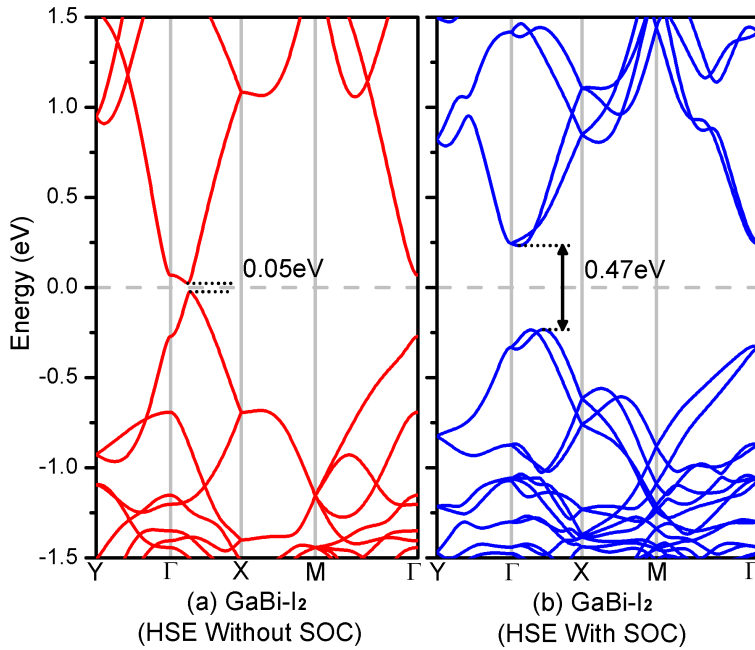


Fig. 5.8 Band structure of the DHF GaBi-I₂ monolayer without and with SOC from HSE calculations. (a) GaBi-I₂ without SOC and (b) GaBi-I₂ with SOC.

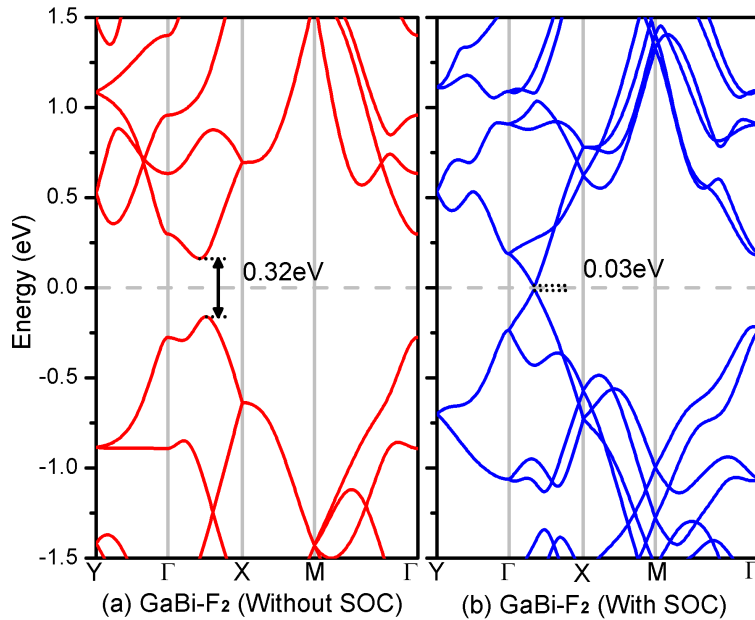


Fig. 5.9 Band structure of the DHF GaBi-F₂ monolayer without and with SOC.

the gapless edge states (Dirac point) appear in the bulk gap and the bands cross linearly at the Γ point, demonstrating the topologically nontrivial nature of these 2D materials.

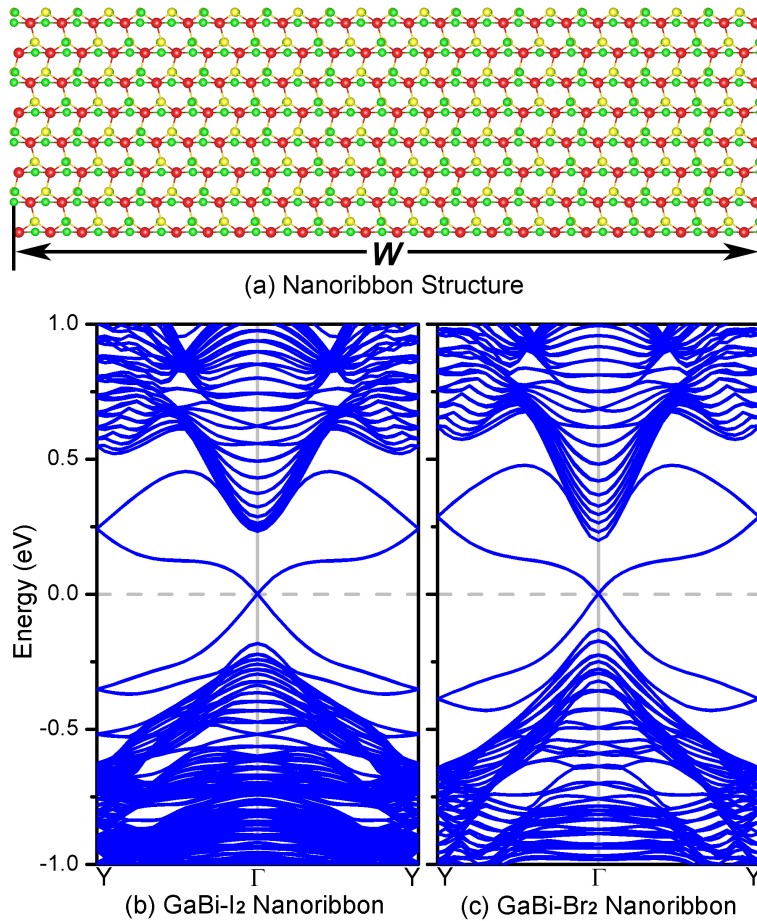


Fig. 5.10 (a) Top view of the nanoribbon structure. The width of the nanoribbon is labeled as W . Electronic band structure of the GaBi-I₂ nanoribbon with $W = 10.2$ nm (b) and the GaBi-Br₂ nanoribbon with $W = 9.9$ nm (c).

5.4 Conclusion

In summary, using first-principles calculations, we predict that the DHF GaBi-X₂ ($X = \text{I, Br, Cl}$) monolayers are QSH insulators with: 1) a novel framework structure, 2) high stability, 3) a sizeable nontrivial bulk gap, and 4) exhibiting the Rashba effect. The DHF structure is robust against different types of functionalization and is more favorable in energy than the RHF structure. The largest nontrivial bulk gap can reach 0.47 eV, which

is sufficient to achieve room-temperature QSH effect. Corresponding to the nonzero Z_2 topological invariant, band calculations show that distorted Dirac cones will appear when the SOC strength is tuned. The nanoribbon edge states with a Dirac point are very promising for future spintronics device applications.

Chapter 6

Bi-Based Topological Insulators: Bi Bilayers with 4,6,8-Atom Rings

¹Two-dimensional (2D) group V elemental materials have attracted widespread attention due to their nonzero band gap while displaying high electron mobility. Using first-principles calculations, we propose a series of new elemental bilayers with group V elements (Bi, Sb, As). Our study reveals the dynamical stability of 4, 6, and 8-atom ring structures, demonstrating their possible coexistence in such bilayer systems. The proposed structures for Sb and As are large-gap semiconductors that are potentially interesting for applications in future nanodevices. The Bi structures have nontrivial topological properties with a direct nontrivial band gap. The nontrivial gap is shown to arise from a band inversion at the Brillouin zone center due to the strong intrinsic spin-orbit coupling (SOC) in Bi atoms. Moreover, we demonstrate the possibility to tune the properties of these materials by enhancing the ratio of 6-atom rings to 4 and 8-atom rings, which results in wider nontrivial band gaps and lower formation energies.

6.1 Introduction

The story of 2D materials begins with the successful exfoliation of graphene from graphite [2]. 2D materials are usually defined as crystalline materials consisting of a single or few layers of atoms. The unusual physical properties, caused by dimensional restrictions, lead

¹The results of this chapter were published as: X. Kong, L. Li, O. Leenaerts, X.-J. Liu, and F. M. Peeters, *Physical Review B* **96**, 035123 (2017). **My contributions:** I proposed the idea and performed partial DFT calculations. I took part in analyzing the data and writing the paper.

researchers to study these materials for possible use in applications and future nanodevices [323]. The search for other 2D materials besides graphene is an on-going field of research. In analogy to graphene, other group IV elements also form 2D hexagonal structures, such as silicene [189, 324, 325, 193], germanene [326, 327], and stanene [328], and have been successfully synthesized on different substrates. Similar structures could also be observed for the 2D group V elemental structures. In theory, buckled hexagonal honeycomb bilayers of group V elements are also stable and favorable in energy [329]. For example, hexagonal Bi(111) bilayers [266, 267, 330, 331] have been experimentally synthesized on Bi_2Te_3 or Bi_2Se_3 surfaces [332–334]. In this connection, the successful growth of single layer blue phosphorus has attracted widespread attention to the group V elemental bilayers due to their nonzero band gap and high electron mobility [335]. There have also been many suggestions for other 2D stable carbon allotropes [126, 336], such as phagraphene [123] and graphyne [337, 158], and some of them have been successfully created or can be found as defects in graphene. The physical properties of such crystalline materials mainly originate from the underlying symmetry of the crystal structure. Therefore, it is interesting to study 2D crystal structures with different symmetries. Recently, some theoretical works have studied 2D group V structures with 4-atom and 8-atom rings on a square lattice [338, 339]. However, the formation energy of these bilayer structures is relatively high which makes it difficult to realize them in experiments. It is thus an interesting question how such materials can be made more stable.

One of the most intriguing properties of some 2D materials is their nontrivial band topology. 2D topological insulators with time-reversal (TR) symmetry, also known as quantum spin Hall (QSH) insulators, are a very important set of 2D materials [340, 40, 48, 341]. Graphene was the first proposal for such a topological insulator, but its negligible nontrivial band gap makes it impossible to observe the QSH effect [341, 342]. In experiment, the QSH effect has been observed in HgTe/CdTe and InAs/GaSb quantum wells [343–345], but the small bulk gap arising from weak SOC makes the operating temperature very low and this limits its further applications [231, 346, 271, 347, 302]. To realize 2D topological insulators with a large band gap, most studies have focused on some heavy elements, such as Bi, which exhibit a strong SOC effect. The largest nontrivial bulk gap (1.08 eV) is found in Bi_2F_2 bilayer. The huge SOC gap in this material originates from the Bi p_x and p_y orbitals [284, 285]. But also, hexagonal Bi(111) bilayer have been realized and their time-reversal symmetry-protected edge states have been

observed [332]. However, their topological nature is still debated. The search for other Bi-based QSH insulators is therefore interesting.

In this work, we propose a new structure model with 4-atom, 6-atom, and 8-atom (4,6,8-atom) rings for the group V elements: Bi, Sb, and As. The formation energy of these proposed structures is lower than those of other reported 2D group V structures containing 4- and 8-atom rings [338, 339]. We find that their phonon spectra contain no imaginary frequency modes, indicating their dynamical stability. In the case of Bi, the calculated band structure suggests nontrivial topological properties with a direct nontrivial bulk gap, resulting from a band inversion at the Γ point. The proposed Sb and As bilayers show large indirect band gaps with SOC, but these band gaps are trivial. We demonstrate that the properties of the proposed structures can be tuned by the number of 6-atom rings. For Bi, we show that the formation energy can be decreased while retaining the topologically nontrivial properties.

6.2 Computational Method

Our first-principles calculations are based on Density Functional Theory (DFT) with the projector augmented wave method as implemented in the Vienna *ab initio* simulation package (VASP) [100, 102, 101]. The generalized gradient approximation (GGA) in the form proposed by Perdew, Burke and Ernzerhof (PBE) [153] was chosen as the electron exchange-correlation functional. The structure relaxation including the atomic positions and lattice vectors was performed by the conjugate gradient (CG) scheme until the maximum force on each atom was less than $0.01 \text{ eV}/\text{\AA}$. The energy cutoff of the plane waves was set to 500 eV with an energy precision of 10^{-5} eV . The Brillouin zone (BZ) was sampled by using a $13 \times 7 \times 1$ Γ -centered Monkhorst-Pack grid. At the same time, to give a more reliable calculation for electronic band structures, the screened Heyd-Scuseria-Ernzerhof Hybrid functional method (HSE06) [97, 98] are also used with a $7 \times 3 \times 1$ Γ -centered Monkhorst-Pack grid for BZ integration. The main electronic band structures in the article for discussions are obtained at the HSE06 level. Phonon frequencies are calculated by the finite displacement method with the PHONOPY code [154].

The Z_2 topological invariants were obtained by calculating the Wannier Charge Centers (WCCs) and tracking the largest gap in the spectrum of the WCCs [113], which is equivalent to the computation of the Wilson loop [114]. The explicit numerical

computations were done with the Z2Pack code [111] which combines the *ab initio* calculations with the Wannier90 code [348]. The surface state calculations are illustrated with an effective tight-binding Hamiltonian generated from the first-principles Wannier functions. The p_x , p_y and p_z orbitals of the Bi atoms from the first-principles wave functions are used as the initial trial orbitals. The iterative Green's function method [349] was used with the software package Wannier_tools [350].

6.3 Results and Discussions

6.3.1 Structure and Stability

Due to the similarity of the proposed structures for the various investigated elements, we mainly focus on the structure model of Bi in this section. An example of such a structure is given in Fig. 6.1. Its lattice is rectangular, which is different from the hexagonal lattice of Bi(111) bilayers [266, 267, 330, 331] and the square lattice of the recently proposed Bi bilayers consisting of 4,8-atom rings [338, 339]. The space group of the proposed orthorhombic crystals is $Pccm$ (or D_{2h}^3). There is a two-fold rotation, mirror, and inversion symmetry in this structure. Along the x direction, there are two kinds of arrangements of atomic rings. One is formed by the line along the center of 4(8)-atom rings while the other is along the center of the 6-atom rings, as indicated by the blue dashed line in Fig. 6.1(a). The two arrangements of atomic rings alternate along the y direction and form a new type of Bi bilayer. Regarding the number of atomic rings, one 4-atom ring corresponds to one 8-atom ring and one 6-atom ring. Since the 4-atom rings always come in pairs with the 8-atom rings, our structure is denoted as a 4(8)-6 Bi bilayer in the following. As demonstrated below, such structures can be easily tuned by including more hexagons. A similar structure model can be applied to Sb and As.

The optimized structure parameters for the 4(8)-6 bilayers of Bi, Sb, and As are listed in Table 6.1. Due to the similarity of these 4(8)-6 bilayers, we focus on the Bi bilayer first. The lattice constant a (b) in the x (y) direction of Bi is 7.918 Å (13.050 Å). Although the lattice of the 4(8)-6 bilayer has different symmetry than the hexagonal and square Bi bilayers, the local arrangement of the neighboring atoms is similar [266, 267, 330, 331, 338, 339]. One Bi atom forms a bond with three other Bi atoms that are all above or below than the position of the Bi atom in the z direction. However, while there is only one kind of Bi atoms (one Wyckoff Position) in the hexagonal and square Bi bilayers, there

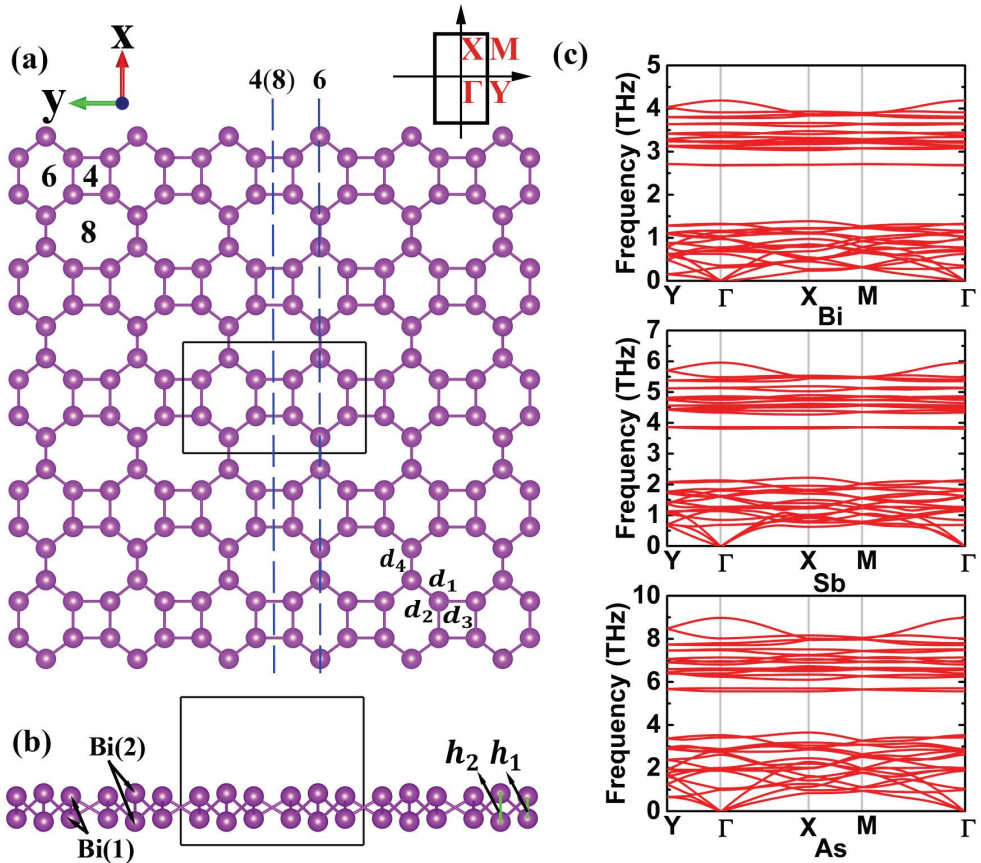


Fig. 6.1 (a) Top view of the 4(8)-6 Bi bilayer: the rectangle indicates the unit cell, the blue dashed lines are the 4(8)-center-connected and 6-center-connected lines, and the inset in the upper right corner depicts the Brillouin zone (BZ) with the time-reversal invariant momenta (TRIM). (b) Side view of the 4(8)-6 Bi bilayer. (c) Phonon spectra of 4(8)-6 Bi, Sb, and As bilayers.

are two kinds of Bi atoms (two Wyckoff Positions) in the 4(8)-6 structure, as illustrated in Fig. 6.1(b). Corresponding to these two kinds of Bi atoms, denoted as Bi(1) and Bi(2) in the following, there are two buckling heights, $h_1 = 1.579 \text{ \AA}$ and $h_2 = 2.014 \text{ \AA}$. The buckling heights of the hexagonal (1.737 \AA) and square (1.757 \AA) Bi bilayer are in between the two heights of the 4(8)-6 Bi bilayer. The Bi atoms in the 4(8)-6 bilayer are connected by four different bonds (see Fig. 6.1(a)) of which the lengths are shown in Table 6.1. The length d_1 of the bond shared by the 6-atom and 8-atom rings is about 3.046 \AA which is practically the same as the bond length in the buckled hexagonal Bi bilayer (3.046 \AA) [266, 267, 330, 331]. The length d_2 of the bond shared by 4-atom and 6-atom rings is about 3.055 \AA , which is slightly larger than d_1 . The bond length d_3 shared by the 4-atom and 8-atom rings is about 3.079 \AA which is larger than the reported bond length (3.059 \AA) shared by the 4-atom and 8-atom rings in square Bi bilayer [338]. The bond length d_4 shared by the 8-atom and 8-atom rings is about 3.043 \AA , which is nearly the same as the reported bond length (3.044 \AA) shared by the 8-atom and 8-atom rings in square Bi bilayer [338]. We can therefore conclude that the proposed structure is formed by an only slightly distorted combination of the square and hexagonal bilayer structures. Similar results are obtained for the 4(8)-6 Sb and As bilayers, although the structure parameters of Sb and As are smaller than that of 4(8)-6 Bi bilayer (see Table 6.1). This is in accordance with the general expectation that the lighter the atoms are, the smaller the structure parameters become.

Table 6.1 The optimized structure parameters of 4(8)-6 Bi, Sb and As bilayers. a (b) is the lattice constant in the x (y) direction; h_1 and h_2 is the buckling height as shown in Fig. 6.1(b); $d_{1,2,3,4}$ denotes the different bond lengths shown in Fig. 6.1(a). ΔE is the formation energy defined by Eq. (1).

Elements	a/b (\AA)	$h_1/h_2/d_1/d_2/d_3/d_4$ (\AA)	ΔE (meV/atom)
Bi	7.918/13.050	1.579/2.014/3.046/3.055/3.079/3.043	52.8
Sb	7.529/12.402	1.505/1.897/2.893/2.901/2.919/2.892	58.1
As	6.581/10.904	1.290/1.593/2.510/2.516/2.531/2.509	71.9

Next, let us focus on the stability of the 4(8)-6 bilayers. To this end, we define the formation energy with respect to the hexagonal bilayer as follows:

$$\Delta E = (E_{total} - N_{atom} \times \mu_{atom})/N_{atom}, \quad (6.1)$$

where E_{total} is the total energy of the 4(8)-6 bilayer, N_{atom} is the total number of atoms in the crystal structure and μ_{atom} is the energy per atom calculated for the hexagonal honeycomb structure. Starting from Bi, ΔE increases with decreasing atomic number. The formation energy for Bi (52.8 meV/atom) is the smallest, while ΔE for Sb and especially As becomes somewhat larger. For comparison, the formation energy of a 4(8)-6 P bilayer was also calculated, and it was found to be even larger (76.8 meV/atom). Furthermore, the phonon spectrum of the P bilayer exhibits imaginary frequency modes, indicating its dynamical instability. Therefore, we will not consider the 4(8)-6 P bilayer in this work. For Bi, the formation energy of the 4(8)-6 Bi bilayer (52.8 meV/atom) is significantly smaller than that of a square Bi bilayer (80.6 meV/atom) [338]. A similar behavior can be observed in 2D C allotropes, where the formation energy decreases with increasing number of C hexagons. In our case, the 4(8)-6 bilayers should be more stable than the reported square bilayers due to the larger number of hexagons [338, 339]. To investigate the dynamical stability of the 4(8)-6 bilayers, their phonon spectrum along the high symmetry lines in the BZ is calculated from first principles using a supercell approximation (see Fig. 6.1(c)). It can be seen that the 4(8)-6 bilayers of Bi, Sb, and As are all dynamically stable, because no imaginary frequency modes are observed in their phonon spectrum.

6.3.2 Electronic Band Structure

As mentioned in the introduction, 2D materials often have interesting electronic properties. The electronic band structures of the investigated 4(8)-6 bilayers at the HSE06 level are shown in Fig. 6.2. The left figures ((a), (c), and (e)) were calculated without SOC and the right ones ((b), (d), and (f)) were calculated with SOC. Let us consider the 4(8)-6 Bi bilayer first. It has a direct band gap of 0.916 eV at the Γ point without SOC, which is similar to that of the square (0.91 eV) but larger than that of the hexagonal Bi bilayer (0.803 eV) [338, 339]. With inclusion of SOC, the 4(8)-6 Bi bilayer retains its direct band gap, which is similar to the case of hexagonal bilayer which also retains a direct band gap with SOC at the HSE06 level [351]. The value of the direct band gap becomes 0.026 eV, which is smaller than that of the hexagonal/square Bi bilayer [338, 351].

On the other hand, the 4(8)-6 Sb/As bilayer has indirect band gaps with and without SOC at the HSE06 level. Different from the 4(8)-6 Bi bilayers, the SOC effect has little effect on the value of the band gap and the indirect property of band gap is not changed.

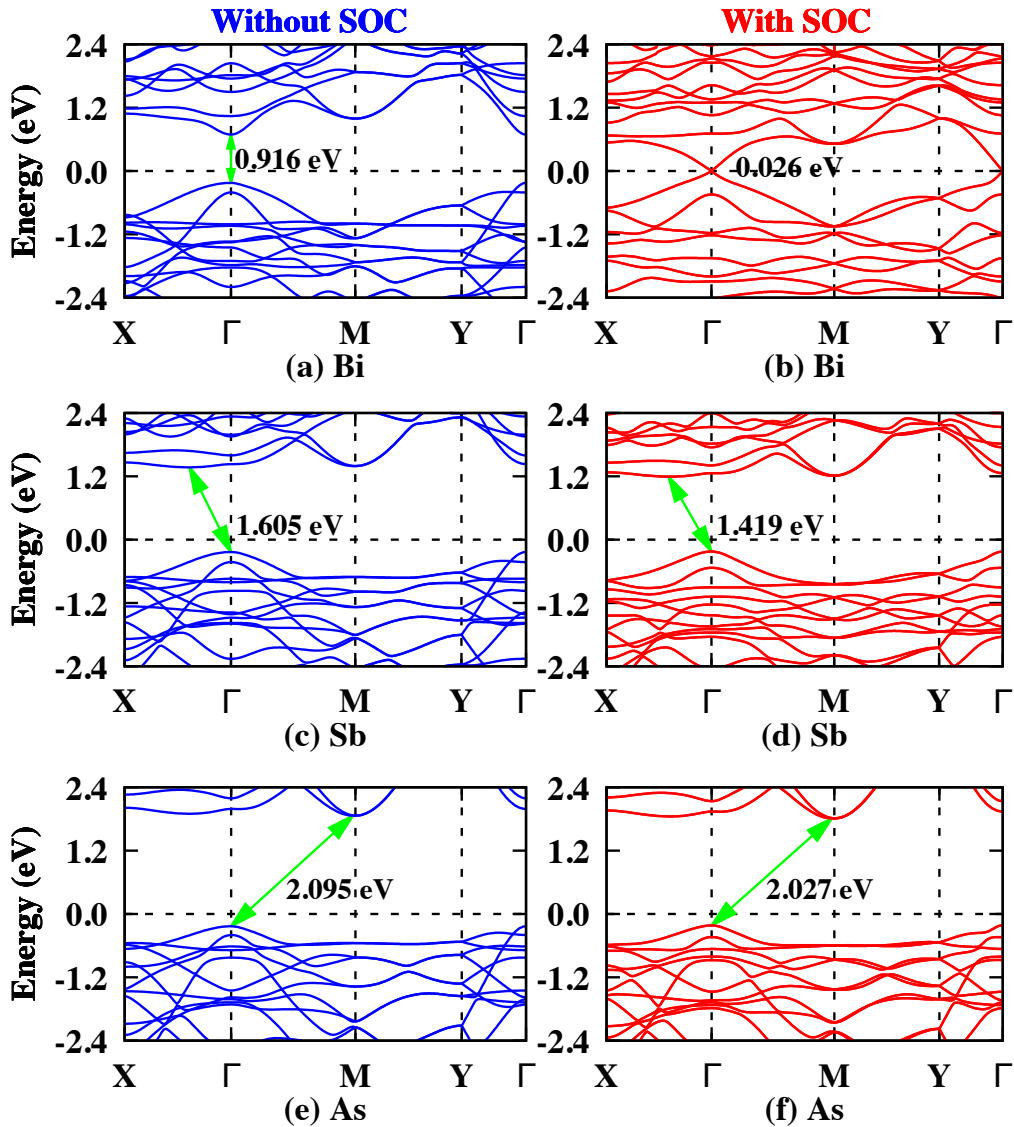


Fig. 6.2 (a), (c) and (e) are the band structures of 4(8)-6 Bi, Sb, and As bilayers without SOC; (b), (d) and (f) are the band structures with SOC. The band gaps are given in the figure. The band structures are calculated at the HSE06 level.

Therefore, we will focus on the band structures without SOC of the two bilayers. The 4(8)-6 Sb bilayer has an indirect band gap (1.605 eV) while the 4(8)-6 As bilayer has a larger indirect band gap (2.095 eV). Similar to the indirect band gap of the hexagonal Sb/As bilayer (2.28 eV/2.49 eV) [329], the indirect band gap property is kept and only the value of the band gap is smaller. It has been studied that the hexagonal Sb/As bilayer can be the promising materials for applications in optoelectronics [329]. Due to the similar band structure with the hexagonal Sb/As bilayer, we conclude that the 4(8)-6 Sb/As bilayer can also be applied in the nanoscale semiconducting devices. Although, 4(8)-6 Bi, Sb, and As bilayers have substantially different band gaps, the regular pattern that the gap values increase with decreasing atomic number is similar to the hexagonal/square group V bilayers [329, 339].

For comparison, the band structures at the PBE level is supplied in the Fig. 6.3. It is well known that the PBE calculations often underestimate the band gap of semiconductors or insulators, which can be confirmed in the band structures without and with SOC of the 4(8)-6 Sb/As bilayer and the band structure without SOC of the 4(8)-6 Bi bilayer. However, the situation is opposite in the band structure with SOC of the 4(8)-6 Bi bilayer, which is due to the special band structure induced by the SOC effect at the Γ point. In the square and hexagonal Bi bilayers, we can also observe the value decreasing of the SOC band gap from the PBE calculations to the HSE06 calculations [338, 351].

6.3.3 Topological Property

Since the electronic band gaps with SOC effect of hexagonal and square Bi bilayers have been shown to be nontrivial [330, 338, 339], we investigate the topological properties of the 4(8)-6 Bi bilayers here. Note that structures containing Bi atoms are often reported to be topologically nontrivial due to the strong intrinsic SOC of Bi. To investigate the topological properties of the 4(8)-6 Bi bilayer, we calculated the Z_2 topological invariant by the Wilson loop methods in the spectrum of the WCCs (see the Fig. 6.4). In addition to the Wilson loop methods, we also calculated the Z_2 invariants by parity analysis because the 4(8)-6 Bi bilayer has inversion symmetry. Following Fu *et al.* [49], the Z_2 topological invariant (ν) in systems with time-reversal symmetry and inversion symmetry can be obtained by:

$$(-1)^\nu = \prod_{i=1}^4 \delta(K_i), \delta(K_i) = \prod_{m=1}^N \xi_{2m}^i, \quad (6.2)$$

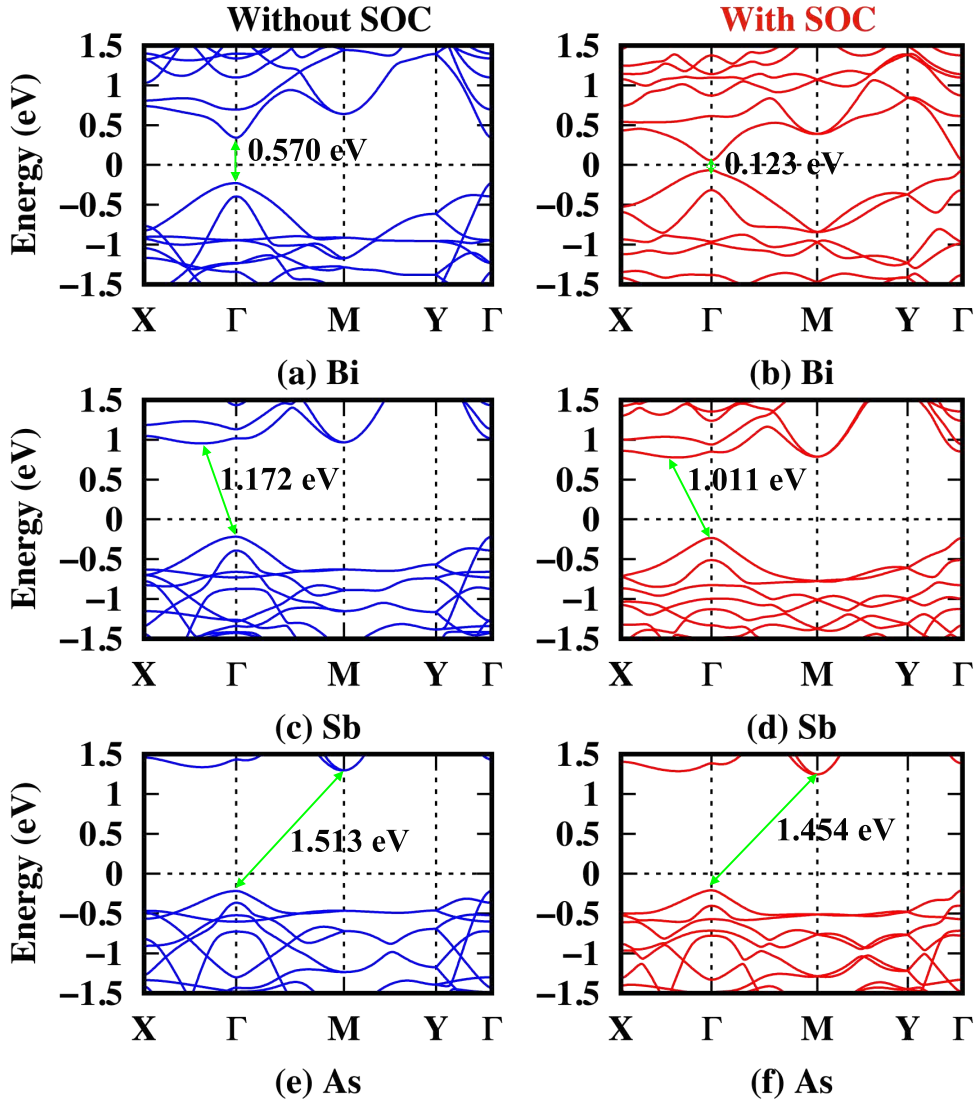


Fig. 6.3 Electronic band structures of Bi, Sb, and As 4(8)-6 bilayers at the PBE level. Without spin-orbit coupling (SOC): (a), (c) and (e); With SOC: (b), (d) and (f). The band gaps are given in the figure.

with K_i the TRIMs, $\xi = \pm 1$ the parity eigenvalue of the wave function, $\delta(K_i)$ the product of the parity eigenvalues at the TRIM, and N the total number of degenerate occupied bands. In our case K_i is Γ , X, Y, or M. The Z_2 topological invariant of the 4(8)-6 bilayer equals 1, which proves its nontrivial nature. We list the results of the parity eigenvalues in Table 6.2. It is seen that only the Bi bilayer has a nontrivial topological invariant ($\nu = 1$), with the only difference in parity eigenvalues between 4(8)-6 Bi and Sb or As bilayers at the Γ point. The parity eigenvalue of -1 at the Γ point of the 4(8)-6 Bi bilayer suggests that there is a band inversion at this TRIM. Similar to the hexagonal and square bilayers, only the Bi bilayer has a topologically nontrivial band gap, while Sb and As bilayers have trivial band gaps [330, 339].

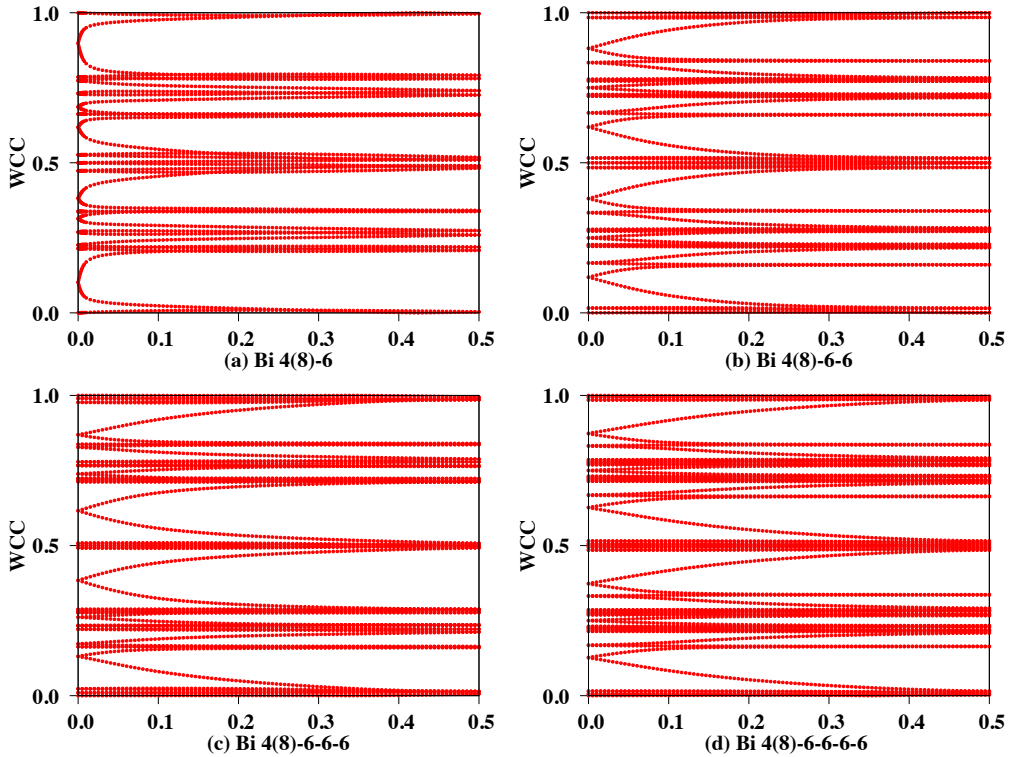


Fig. 6.4 Evolution of Wannier charge centers (WCCs) for the calculations of the Z_2 topological invariant. (a) Bi 4(8)-6; (b) Bi 4(8)-6-6; (c) Bi 4(8)-6-6-6; (d) 4(8)-6-6-6-6. The results show that all the four structures are topological insulators with $Z_2 = 1$. The calculations are done at the HSE06 level.

To find the origin of the topologically nontrivial nature of the 4(8)-6 Bi bilayer, we investigate the band inversion by the orbital-projected band structures as shown in Fig. 6.5. We can see that SOC plays an important role in the inversion of the states with

Table 6.2 The parity eigenvalues at the four TRIMs (Γ , X, Y, M) and the Z_2 topological invariants (ν) of the 4(8)-6 Bi, Sb, and As bilayers.

Element	Γ	X	Y	M	ν
Bi	-1	1	-1	-1	1
Sb	1	1	-1	-1	0
As	1	1	-1	-1	0

$p_{x,y}$ and p_z -orbital character: without SOC at the Γ point, the $p_{x,y}$ orbitals contribute the most to the highest occupied band and the p_z orbitals contribute the most to the lowest unoccupied band, but the situation is reversed when including SOC. This is also verified by the reversal of parity eigenvalues between the highest occupied band and the lowest unoccupied band at the Γ point. Note that the observed band inversion found here is similar to the case of hexagonal and square Bi bilayers whose band inversion also occurs between the $p_{x,y}$ and p_z orbitals [330, 338, 339]. The band inversion indicates that there must be a gap closing with corresponding formation of a Dirac cone when continuously turning on the SOC [338, 352]. To find the Dirac cone, continuous variations of SOC strengths λ were applied to calculate the corresponding band gaps of the 4(8)-6 Bi bilayer. As shown in Fig. 6.6, for $\lambda < 0.962$, the band gaps decrease as λ increases; for $\lambda > 0.962$, the band gaps begin to increase as λ increases; and for $\lambda = 0.962$, there is a zero gap state. Therefore, the band structure for $\lambda = 0.962$ is plotted in the inset, and a gap closing with a Dirac point at the Γ point could be observed.

Besides the nonzero Z_2 topological invariant and the observed band inversion, the existence of gapless edge states is another prominent feature of QSH insulators. According to the bulk-edge correspondence in topological insulators, a nontrivial topological invariant ($\nu = 1$) indicates the presence of topologically protected edge states at the edges of the material. The calculated edge states of the 4(8)-6 Bi bilayer are shown in Fig. 6.7. In Fig. 6.7(a), it is seen that there are edge states in the band gap without SOC, but these edge states do not bridge the band gap which indicates that they are trivial. However, including SOC, there are two oppositely propagating gapless edge states appearing in the bulk gap that connect the conduction and valence bands and which cross at the TRIM (X point) as shown in Fig. 6.7(b).

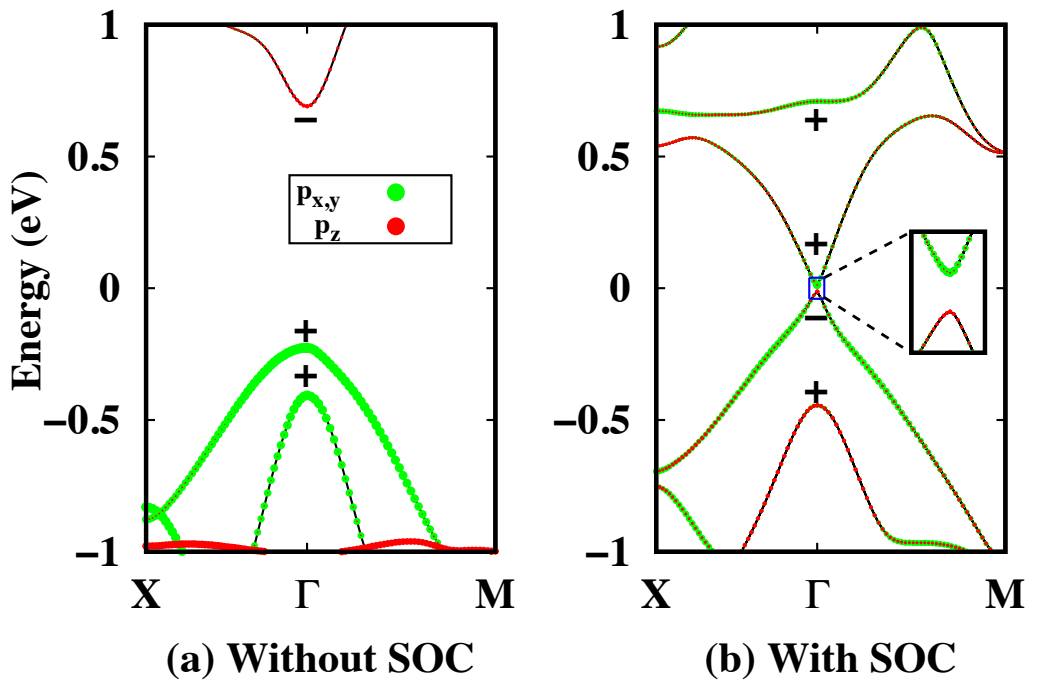


Fig. 6.5 The orbital-projected band structures of the 4(8)-6 Bi bilayer: (a) without SOC and (b) with SOC. The symbol size indicates the contribution weight: larger dot means higher contribution while smaller one indicates lower contribution. \pm indicates an even or odd parity eigenvalue. Green: $p_{x,y}$ (p_x and p_y) orbitals; red: p_z orbitals.

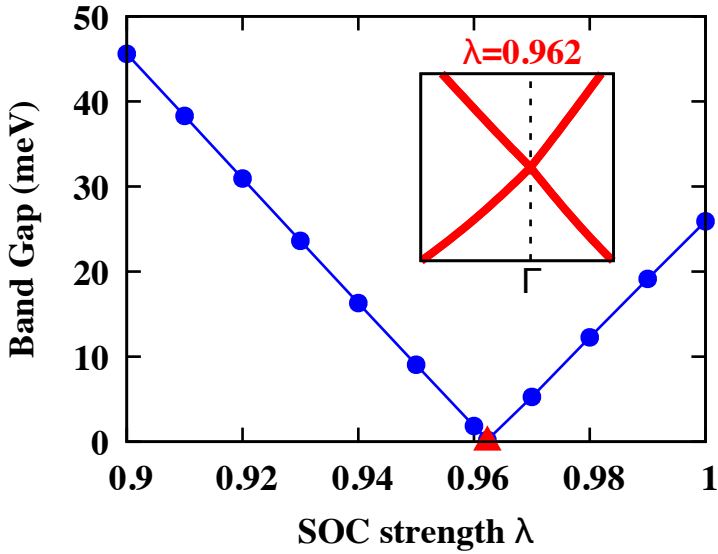


Fig. 6.6 (a) Variation of the band gap in 4(8)-6 Bi bilayer as a function of SOC strength λ . The red triangle indicates the critical point at $\lambda = 0.962$. The inset demonstrates the gapless Dirac point at the Γ point for $\lambda = 0.962$. The band crossing with a Dirac point indicates there is a topological phase transition by tuning the SOC strength λ continuously.

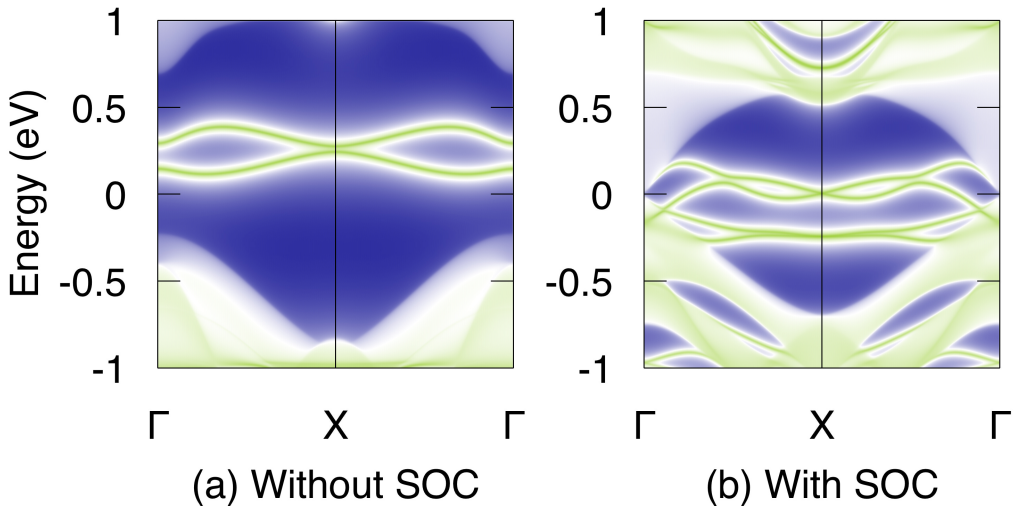


Fig. 6.7 The edge states of 4(8)-6 Bi bilayer: (a) without SOC; and (b) with SOC.

6.3.4 Structural Tunability

As we discussed above, the formation energy decreases with increasing number of 6-atom rings in the system. In this section we investigate how the properties of the 4(8)-6 Bi bilayer can be tuned by changing the number of hexagons. This is done in a systematic way by increasing the number of 6-connected-lines which connect the centers of 6-atom rings in the x direction. Taking Bi as an example, we show three such structures in Fig. 6.8. As indicated by the blue dashed lines, the number of 6-connected-lines is 2, 3, and 4 in these structures and they are correspondingly named 4(8)-6-6, 4(8)-6-6-6 and 4(8)-6-6-6-6. The calculated structure parameters of the three structures are shown in Table 6.3. Due to the similar structure along the x direction compared to 4(8)-6, the lattice constants of the expanded structures in the x direction are similar (7.919 Å, 7.778 Å, 7.708 Å, and 7.661 Å) and are in between those of the square and hexagonal structures. We can easily understand this: the larger the number of the 6-atom rings becomes, the closer to the hexagonal Bi bilayer the expanded structure gets. There is now a larger variety of different Bi atoms, corresponding to various buckling heights, so we compare the averaged buckling heights. These are 1.724 Å, 1.735 Å, 1.734 Å, and 1.734 Å, respectively. Note that these averaged buckling heights are larger than the buckling height of 1.71 Å as found in the hexagonal Bi bilayer [331, 353] and smaller than 1.76 Å in the square Bi bilayer [338, 339].

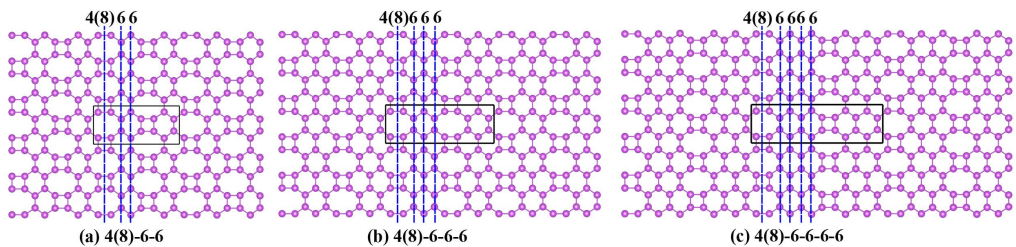


Fig. 6.8 The tunable structures: (a) 4(8)-6-6; (b) 4(8)-6-6-6; (c) 4(8)-6-6-6-6 Bi bilayers. The blue dashed lines are the 4(8)-center-connected and 6-center-connected lines.

We also calculated the energy per atom in all these structures and compare them to the hexagonal and square Bi bilayers which have been studied before [331, 338, 339, 353]. As shown in Fig. 6.9, the hexagonal Bi bilayer has the lowest energy which implies it is the most stable of all these structures. On the other hand, the square Bi bilayer has the largest energy of all. The energy per atom of the new proposed structures varies

Table 6.3 The optimized structure parameters of 4(8)-6-6, 4(8)-6-6-6, and 4(8)-6-6-6-6 Bi bilayers. a (b) is the lattice constant in the x (y) direction; h is the averaged buckling height.

Structures	a (Å)	b (Å)	h (Å)
4(8)-6-6	7.778	17.493	1.735
4(8)-6-6-6	7.708	21.834	1.734
4(8)-6-6-6-6	7.661	26.188	1.734

monotonously between these two limiting structures and converges to the energy of the hexagonal bilayer as more hexagons are included.

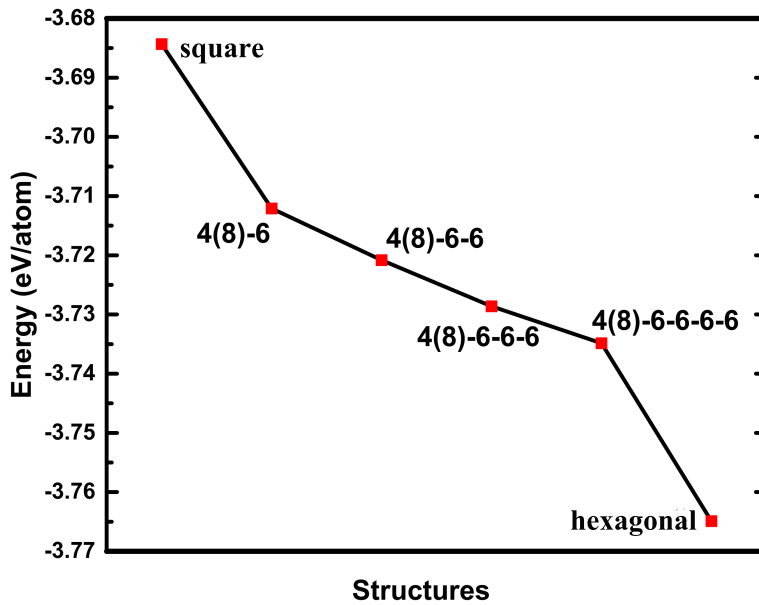


Fig. 6.9 The energy per atom of 4(8)-6, 4(8)-6-6, 4(8)-6-6-6, 4(8)-6-6-6-6 Bi bilayers.

The electronic band structures of the 4(8)-6-6, 4(8)-6-6-6, 4(8)-6-6-6-6 Bi bilayers at the HSE06 level are shown in Fig. 6.10. As shown in Fig. 6.10(a), (c) and (e), the direct band gaps calculated without SOC of the three structures are 0.820 eV, 0.880 eV and 0.890 eV, which are smaller than that of 4(8)-6 Bi bilayer (0.916 eV). After including the SOC, as shown in Fig. 6.10(b), (d) and (f), the direct band gaps of the three structures are 0.303 eV, 0.237 eV and 0.311 eV, which are much larger than that of the 4(8)-6 Bi bilayer (0.026 eV). For the three structures, their band structures at the PBE level are shown in the Fig. 6.11. Similar to the band structure with SOC of the 4(8)-6 Bi bilayer, they also show the value decreasing of band gap from the PBE calculations to the HSE

calculations. Since the SOC band gap of the 4(8)-6 Bi bilayer is nontrivial, we calculated the Z_2 topological invariant of the new three Bi bilayers, and all the Z_2 are equal to 1 which confirms they are all 2D topological insulators (Fig. 6.4). It can be concluded that the value of the nontrivial SOC band gap will approach that of the hexagonal Bi bilayer upon inclusion of more Bi hexagons [330, 351]. To further confirm their topological properties, the nontrivial edge states of 4(8)-6-6, 4(8)-6-6-6, 4(8)-6-6-6-6 Bi bilayers are shown in Fig. 6.12, and the edge Dirac cones are clearly observed. The topological edge states of the three structures appear to be very similar.

In general, we can conclude that as the number of the 6-atom rings increases, the energy, electronic structure, and nontrivial band gap approach those of the hexagonal Bi bilayer. At the same time, the lines of 4-atom and 8-atom rings can be regarded as line defects in the hexagonal Bi bilayer. By introducing such line defects, it is possible to tune the properties of the hexagonal Bi bilayer.

6.4 Conclusions

Using first-principles calculations, we propose a new stable 4(8)-6 model for the group V elements (Bi, Sb, As), which enrich the family of 2D materials. Their formation energy compares favorably to the square bilayer while our phonon calculations confirm their dynamical stability. The trivial (Sb, As) and nontrivial (Bi) band gaps make the group V 4(8)-6 structures promising candidates for applications in future nanodevices. The nontrivial topological phase of the Bi 4(8)-6 structure are demonstrated by the calculations of Z_2 topological invariant, band inversion and the edge states. Moreover, the 4(8)-6 model allows for property tuning by changing the ratio of hexagons in the structure. In the case of Bi, we investigated 3 such models, namely 4(8)-6-6, 4(8)-6-6-6, and 4(8)-6-6-6-6, and found that they are all topological insulators. As the number of the hexagons increases, the energy, electronic structure, and nontrivial band gap approach those of the hexagonal Bi bilayer. In the dilute limit, the lines of 4-atom and 8-atom rings can be regarded as line defects in the hexagonal Bi bilayer that can be used to tune the properties of the hexagonal Bi bilayer.

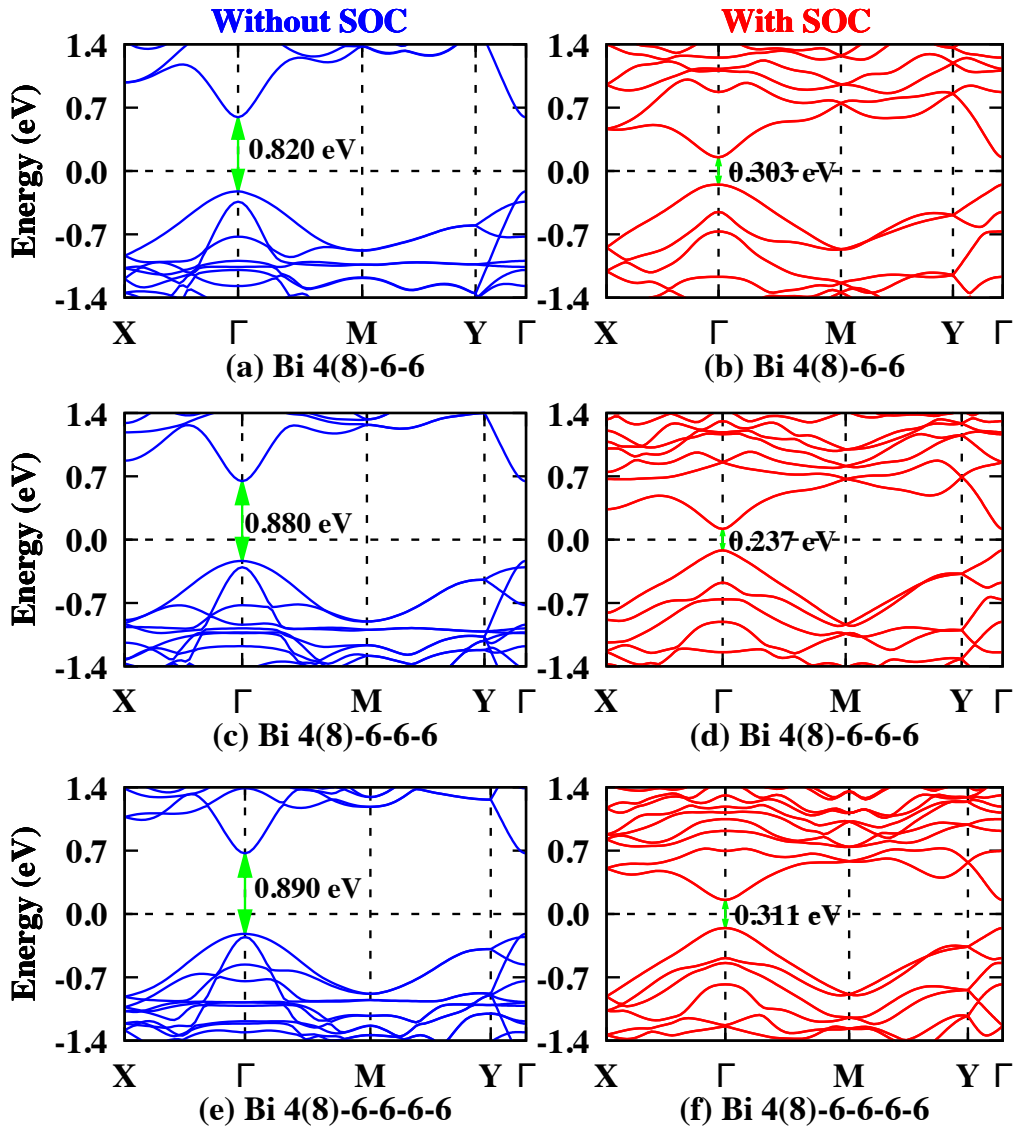


Fig. 6.10 (a), (c), and (e) are the band structures of the 4(8)-6-6, 4(8)-6-6-6, and 4(8)-6-6-6-6 Bi bilayers without SOC; (b), (d), and (f) are the band structures with SOC. The band gaps are marked in the figure. The band structures are calculated at the HSE06 level.

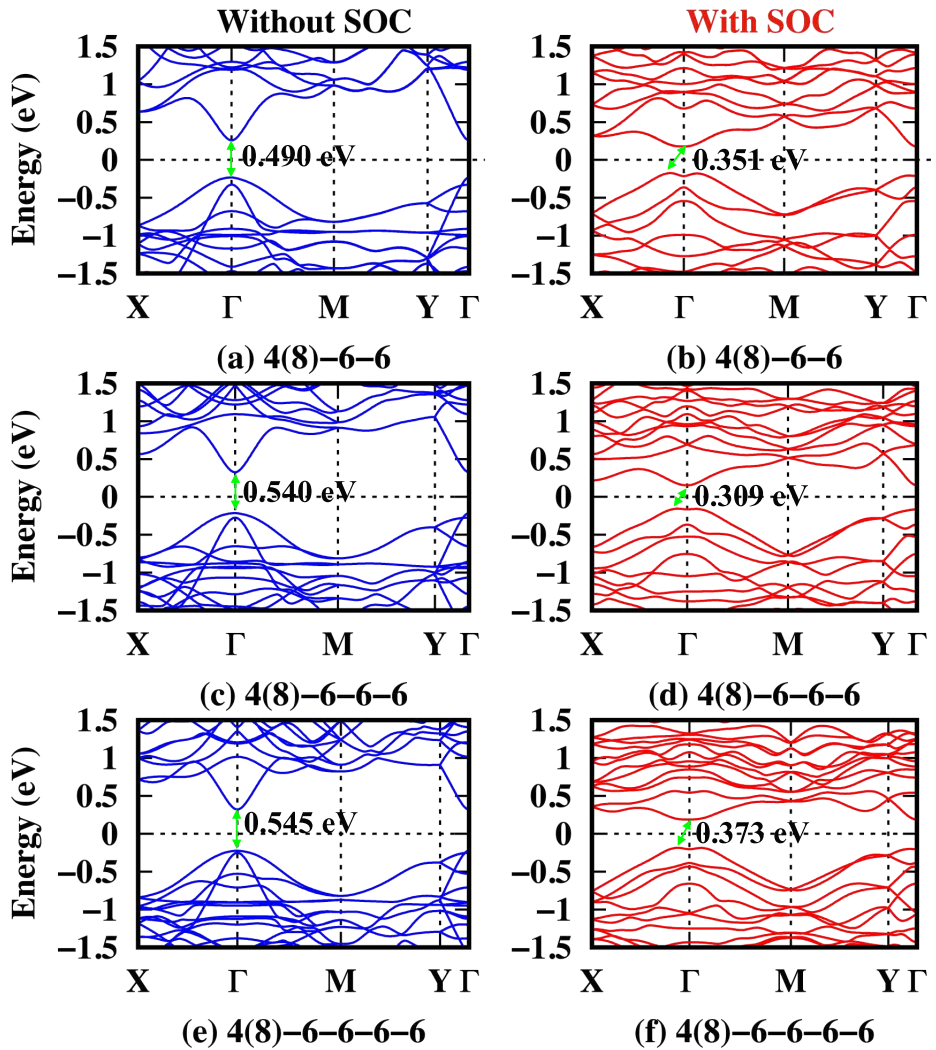


Fig. 6.11 Electronic band structures of Bi 4(8)-6-6, 4(8)-6-6-6 and 4(8)-6-6-6-6 bilayers at the PBE level. Without SOC: (a), (c) and (e); With SOC: (b), (d) and (f). The band gaps are given in the figure.

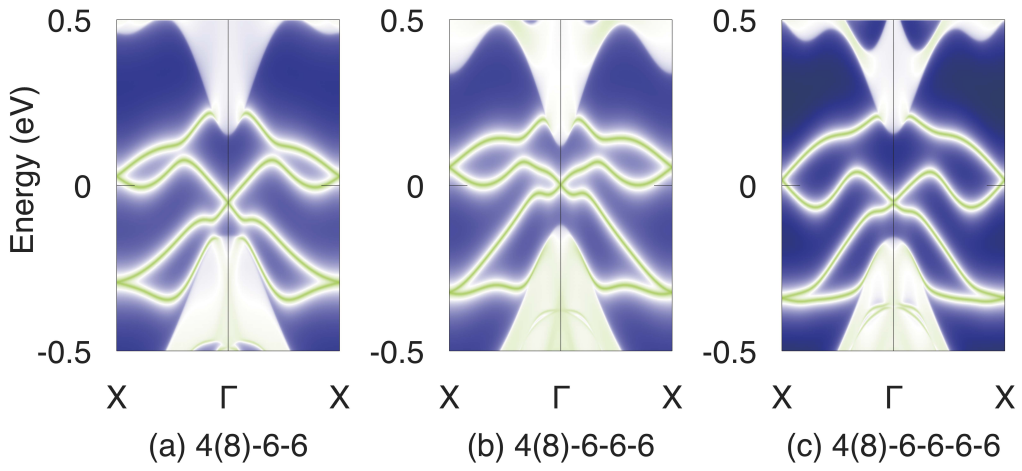


Fig. 6.12 The nontrivial edge states of the structures: (a) 4(8)-6-6, (b)4(8)-6-6-6, and (c) 4(8)-6-6-6-6 Bi bilayers.

Chapter 7

Y-Based Chern Insulator: 1T-YN₂

¹The quantum anomalous Hall (QAH) effect is a topologically nontrivial phase, characterized by a non-zero Chern number defined in the bulk and chiral edge states in the boundary. Using first-principles calculations, we demonstrate the presence of the QAH effect in 1T-YN₂ monolayer, which was recently predicted to be a Dirac half metal without spin-orbit coupling (SOC). We show that the inclusion of SOC opens up a large nontrivial band gap of nearly 0.1 eV in the electronic band structure. This results in the nontrivial bulk topology which is confirmed by the calculation of Berry curvature, anomalous Hall conductance and the presence of chiral edge states. Remarkably, a QAH phase of high Chern number $C = 3$ is found, and there are three corresponding gapless chiral edge states emerging inside the bulk gap. Different substrates are also chosen to study the possible experimental realization of the 1T-YN₂ monolayer while keeping its nontrivial topological properties. Our results open a new avenue in searching for QAH insulators with high temperature and high Chern numbers, which can have nontrivial practical applications.

7.1 Introduction

The discovery of quantum Hall effect brought about a new fundamental concept, the topological phase of matter, to condensed matter physics [354]. The quantum Hall effect is obtained in a two-dimensional (2D) electron gas in the presence of a strong

¹The results of this chapter were published as: X. Kong, L. Li, O. Leenaerts, W. Wang, X.-J. Liu, and F. M. Peeters, *Nanoscale* **10**, 8153 (2018). **My contributions:** I proposed the idea and performed partial DFT calculations. I took part in analyzing the data and writing the paper.

perpendicular external magnetic field, which drives the electrons to fill in the discrete Landau levels, resulting in the quantized Hall conductance. Nevertheless, Landau levels are not the necessary ingredient for the realization of the quantum Hall effect, where the integer Hall plateaus are actually interpreted by Chern numbers, a type of topological invariants defined in the 2D momentum space [355]. The topological interpretation implies that the realization of quantum Hall effect may be achieved without external magnetic field. The first toy model for the quantum Hall effect without Landau level, i.e. the quantum anomalous Hall (QAH) effect was proposed by Haldane in 1988 in a 2D honeycomb lattice with next-nearest-neighboring hopping modulated by staggered flux [42]. While there have been theoretical studies of QAH effect in solid state materials [77, 356], little progress was made in experiment until the discovery of time-reversal (TR) invariant topological insulators [40, 72]. Realization of QAH effect combines several basic ingredients that the system should be in 2D regime, insulating, TR symmetry breaking with a finite magnetic ordering, and has a non-zero Chern number in the valence bands [357, 358]. Many theoretical schemes for realizing QAH insulators have been proposed, including the magnetically doped quantum well-based 2D topological insulators [359], graphene with transition metal (TM) adatoms ($3d$, $4d$ and $5d$) [79, 360–362], buckled honeycomb-lattice systems of group IV or V elements with TM adatoms [363–365], half-functionalized honeycomb-lattice systems [366, 367], heterostructure quantum wells [368, 369], organic metal frameworks [260], sd^2 ‘graphene’ with TM atoms [370] and also ultracold atom systems [371, 372]. In particular, following the theoretical work by Yu *et al.* [373], the QAH effect was first realized experimentally using Cr-doped magnetic thin-film topological insulator, with the quantized Hall conductance being observed [374]. The QAH states have also been reported in experiment for ultracold atoms, with the Haldane model [375] and a minimized spin-orbit coupled model [376] being realized, respectively. Realization of QAH phases is of great interests both in fundamental theory and potential applications. For example, the chiral edge states of a spin-orbit coupled QAH insulator may exhibit novel topological spin texture in real space, which can have applications in designing spin devices [377]. More interestingly, the heterostructure formed by a QAH insulator and conventional s -wave superconductivity can realize chiral topological superconductors, which host Majorana zero modes binding to vortices and chiral Majorana edge modes in the boundary [378, 379]. Remarkably, a recent experiment observed such chiral Majorana edge modes based on the QAH

insulator/*s*-wave superconductor heterostructure, where a $e^2/(2h)$ -plateau of tunneling conductance was observed [380].

Albeit the important experiment progress, there are several limitations for the current study of real QAH materials. First, so far the QAH phases in solid state materials have only be observed at quite low temperature, typically in the order of mK, due to small topological bulk gap [374]. To enable broad studies of fundamental physics and potential future applications, it is important to have QAH insulators with a large bulk gap and observable with high temperature. Furthermore, the current experimental studies are focused on the QAH states with low Chern number $C = \pm 1$. The QAH insulators with high Chern numbers exhibit different topological phases which are expected to bring about new fundamental physics and interesting applications but they are yet to be demonstrated experimentally. This motivates us to search for new QAH insulators based on the transition metal compounds.

Transition metal is defined as an element whose atom has a partially filled *d* sub-shell or which can give rise to cations with an incomplete *d* sub-shell [381]. Due to the partially filled *d* shell, TMs can have many different oxidation states when forming compounds and show many appealing electronic, magnetic, and catalytic properties. Strong electronegative elements (groups V, VI, and VII) are easily combined with TMs to form stable compounds. One of the most attractive compounds are the transition metal dichalcogenides (TMDs) with chemical composition TMX_2 , where TM stands for the TM and X is a chalcogen element such as S, Se, or Te [382, 383]. TMD monolayers have many new physical properties as compared to their bulk counterparts due to their reduced dimensions. As confirmed by experiment, TMDs can exhibit three different structures, called 1H, 1T, and 1T' [384]. Using first-principles calculations, TMD monolayers have been predicted to show both semiconducting (1H-MoS₂) [253] and metallic (1T-PtSe₂) [385] properties, spin polarization effect (1H-VS₂) [386] and quantum spin Hall (QSH) effect (1T'-WTe₂) [384, 387], where some of them have been realized experimentally [382, 383]. However, the QAH effect has not yet been predicted in TMD structures. A recent expansion of the TMD-like compounds has been realized through MoN₂, a nitrogen-rich TM nitrides (TMN) that has been synthesized through a solid-state ion-exchange reaction under high pressure [388]. First-principles calculations predict that 1H-MoN₂ monolayer is a high temperature 2D ferromagnetic (FM) material with Curie temperature of nearly 420 K [389]. This suggests that combining TM and N atoms can

lead to stable 2D monolayers exhibiting novel band structures. A natural question arises: can we find the QAH effect in the TMNs?

Previous calculations focused on TMN monolayers with the chemical composition TMN₂ (TM = Y, Zr, Nb and Tc) which demonstrated that the most energetically and dynamically stable phase is 1T [390–392]. Interestingly, the strong nonlocal *p* orbitals of the N atoms in 1T-YN₂ result in a Curie temperature of 332 K. The three unpaired electrons in the two N atoms give 1T-YN₂ a FM ground state with a total magnetic moment of $3\mu_B$ per unit cell. Remarkably, the electronic band structures as obtained from DFT calculations show that 1T-YN₂ is a *p*-state Dirac half metal (DHM) in the absence of spin-orbit coupling (SOC). A DHM is defined as a metal in which a Dirac cone exists at the Fermi level in one spin channel and a band gap opens in the other channel [393, 394]. The 100% spin-polarization and massless Dirac fermions in DHMs attracted a lot of attention due to potential applications in high-speed spintronic devices [392]. In this paper, we investigate the stable 1T-YN₂ monolayer using first-principles calculations with the inclusion of SOC. We obtain a relatively large nontrivial band gap (≈ 0.1 eV) in the Dirac cone. The nontrivial properties of the 1T-YN₂ monolayers are further confirmed by the calculation of the Berry curvature, the anomalous Hall conductance (AHC), the Chern number, and the corresponding edge states. The large nontrivial band gap and high Chern number are very interesting for practical applications in future nanodevices.

7.2 Computational Method

The first-principles calculations were done with the Vienna *ab initio* simulation package (VASP) using the projector augmented wave (PAW) method in the framework of Density Functional Theory (DFT) [100, 102, 101]. The electron exchange-correlation functional was described by the generalized gradient approximation (GGA) in the form proposed by Perdew, Burke, and Ernzerhof (PBE) [153]. The structure relaxation considering both the atomic positions and lattice vectors was performed by the conjugate gradient (CG) scheme until the maximum force on each atom was less than 0.01 eV/Å, and the total energy was converged to 10^{-5} eV with Gaussian smearing method. To avoid unnecessary interactions between the YN₂ monolayer and its periodic images, the vacuum layer is set to at least 17 Å. The energy cutoff of the plane waves was chosen as 500 eV. The Brillouin zone (BZ) integration was sampled by using a $31 \times 31 \times 1$ Γ -centered Monkhorst-Pack grid. To obtain a more reliable calculation for the electronic band structure, especially the band

gap, the screened Heyd-Scuseria-Ernzerhof Hybrid functional method (HSE06) [97, 98] with mixing constant 1/4 was also used with a $15 \times 15 \times 1$ Γ -centered Monkhorst-Pack grid for BZ integration. SOC is included by a second variational procedure on a fully self-consistent basis. In the calculations of van der Waals (vdW) heterostructures and quantum wells in our work, the zero damping DFT-D3 method of Grimme within the PBE functional was employed for the vdW correction [186]. An effective tight-binding Hamiltonian constructed from the maximally localized Wannier functions (MLWF) was used to investigate the surface states [348, 132]. The iterative Green's function method [395] was used with the package WannierTools [350].

7.3 Results

SOC is a relativistic effect which describes the interaction of the spin of an electron with its orbital motion [396, 397]. Though SOC is a small perturbation in a crystalline solid and has little effect on structure and energy, it plays a more important role in the band structure near the Fermi level in the case of heavy elements. SOC will cause a spin splitting of the energy bands in inversion-asymmetric systems, and more importantly, it can result in a band opening and a band inversion that gives rise to fascinating phenomena. Previous studies neglected SOC in 1T-YN₂, although the SOC effect of the Y and N atoms are not negligible and turns out to be important to realize the topological properties discussed in our work. In the following, we will take SOC into account and study the electronic band structure of stable 1T-YN₂ monolayer by first-principles calculations. Though the calculation demonstrated that the easy magnetic axis of 1T-YN₂ monolayer is in-plane, the Magnetocrystalline Anisotropy Energy (MAE) of the out-of-plane spin orientation is only about 0.025 meV per spin of every nitrogen atom. Therefore, The spin orientation in the calculations is chosen in the direction of out-of-plane.

The space group of YN₂ is $P\bar{3}m1$ (No.164, D_{3d}^3), and its Wyckoff Positions are Y (0, 0, 0) and N ($1/3, 2/3, z$) with $z = 0.04489$. As shown in Fig. 7.1(a), the Y atom is the inversion center in the octahedral structure unit and the three N atoms in the upper layer will turn into the three N atoms in the lower layer under inversion. The optimized lattice parameter and Y–N bond distance are 3.776 and 2.350 Å, respectively, which is in good agreement with previous calculations [392]. Without SOC, we observe a distorted Dirac cone along the M-K high-symmetry line both at the PBE and HSE06 level. Similar band structures can also be observed in other 2D non-magnetic systems, such as the TaCX

[398] and the distorted hexagonal frameworks GaBi-X₂ (X = I, Br, Cl) [399]. However, distorted Dirac cones in 2D magnetic systems are rare. The calculated band structures with SOC are shown in Fig. 7.1(b). The blue lines indicate the band structure at the PBE level and a band gap (29.7 meV) can be observed at the Fermi level along the M-K high-symmetry line. The semilocal approximations to the exchange-correlation energy at the PBE level underestimate the band gap with respect to experiment and overestimate electron delocalization effects for many *d*-element compounds. Therefore, calculations at the HSE06 level are necessary to give more reliable band gaps and band structures. We found that the band gap at the HSE06 level is larger than that at the PBE level. To see the difference more clearly, the enlarged band structure is shown in Fig. 7.1(c). The calculated band gap at the PBE level is $\Delta E_{PBE} = 29.7$ meV, while that at the HSE06 level ΔE_{HSE06} increases to 97.5 meV. By projecting the wavefunctions onto the spherical harmonics, we analyzed the occupation of the different atomic orbitals both with and without SOC near the Fermi level. Though there are minor contributions of *d* orbitals from the Y atom near the Fermi level, the major contribution of the atomic orbitals comes from the *p* orbitals of the N atoms. This is consistent with previous study [392]. Next, we constructed a tight-binding Hamiltonian with 12 Wannier functions by projecting the *p_x*, *p_y*, and *p_z* orbitals of the two N atoms in the unit cell of 1T-YN₂ in order to further examine the electronic band structure. Despite the difference in the band gap, the main character close to the Fermi level at the PBE and HSE06 level with SOC are qualitatively the same. In the following analysis, we will consider the results at the PBE level with SOC.

To investigate the topological properties of 1T-YN₂, we first calculated the gauge-invariant Berry curvature in momentum space. The Berry curvature $\Omega_z(k)$ in 2D can be obtained by analyzing the Bloch wave functions from the self-consistent potentials:

$$\Omega_z(k) = \sum_n f_n \Omega_n^z(k), \quad (7.1)$$

$$\Omega_n^z(k) = -2 \sum_{m \neq n} \text{Im} \frac{\langle \psi_n(k) | v_x | \psi_m(k) \rangle \langle \psi_m(k) | v_y | \psi_n(k) \rangle}{(\varepsilon_m(k) - \varepsilon_n(k))^2}, \quad (7.2)$$

where f_n is the Fermi-Dirac distribution function, $v_{x(y)}$ is the velocity operator, $\psi_n(k)$ is the Bloch wave function, ε_n is the eigenvalue and the summation is over all *n* occupied bands below the Fermi level (*m* indicates the unoccupied bands above the Fermi level). In Fig. 7.2 the reproduced band structure (blue curves) and Berry curvature (red curves)

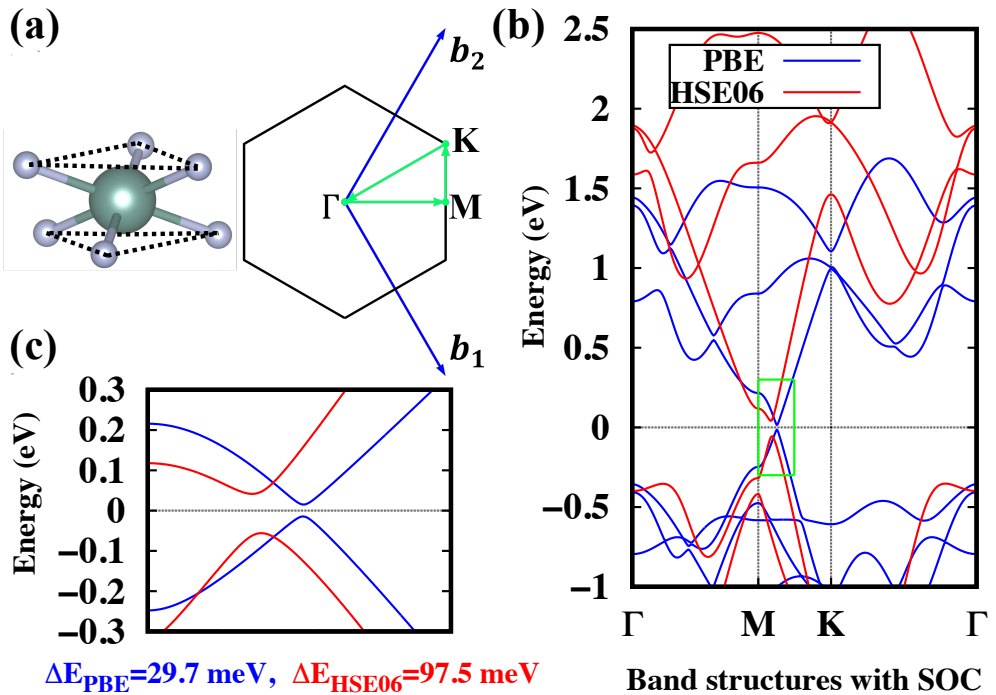


Fig. 7.1 (a) The octahedral structure unit of 1T-YN₂ monolayer and the corresponding 2D Brillouin zone with its high symmetry points (Γ , M and K). b_1 and b_2 are the reciprocal lattice vectors. The band structure is calculated along the green path (Γ -M-K- Γ). (b) Band structures of 1T-YN₂ monolayer with SOC calculated at the PBE and HSE06 levels. The blue lines indicate the PBE calculations, and the red lines indicate the HSE06 calculations. (c) The enlarged band structures shown in the green rectangle in (b). The band gaps are indicated below the figure: $\Delta E_{PBE} = 29.7 \text{ meV}$ and $\Delta E_{HSE06} = 97.5 \text{ meV}$.

along the high symmetry direction K-M-K', calculated by Wannier interpolation [348], are shown. To clarify that our MLWF is good enough to describe the electronic structures of 1T-YN₂, we also plot the band structures reproduced by the MLWF basis together with the PBE results along the high symmetry direction Γ -M-K in Fig. 7.3. As can be observed, the nonzero Berry curvature is mainly distributed around the avoided band crossings at the Fermi level. The peaks in the Berry curvature at the two sides of the M point have the same sign. Furthermore, a plot of the Berry curvature peaks over the whole Brillouin zone (see inset of Fig. 7.2) indicates that all 6 peaks have the same sign because of inversion symmetry. Furthermore, the out of plane spin textures (see Fig. 7.4) is consistent with Berry curvature peaks, and we could conclude that the two Berry curvature peaks at the two sides of the M point contribute to the nonzero Chern number 1. The total Chern number from the 6 Berry curvature peaks is summed to 3, and this will be discussed below.

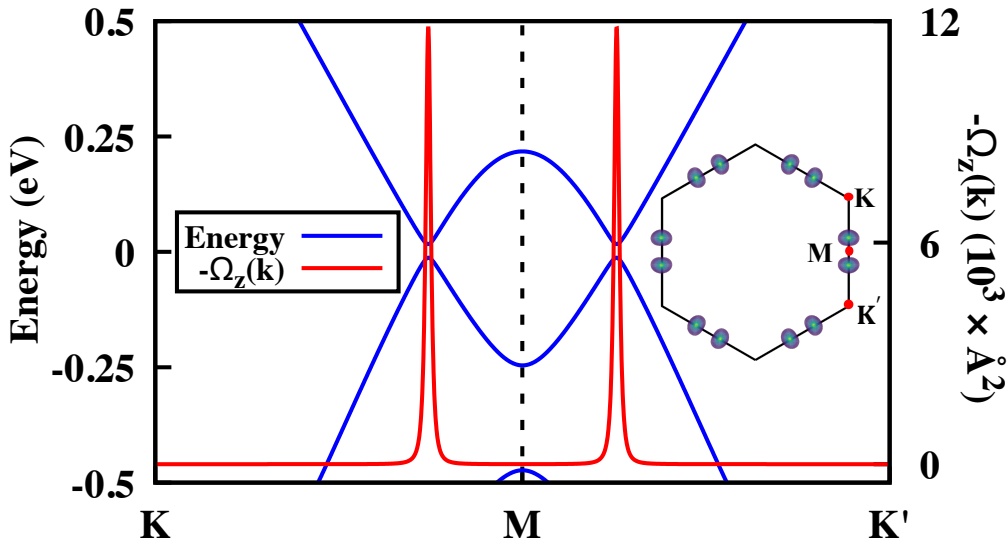


Fig. 7.2 The reproduced band structures along the path K-M-K' (blue curves) with MLWF basis and the distribution of the corresponding Berry curvature in momentum space (red curves). The inset indicates the position of the peaks of the Berry curvature in the 2D Brillouin zone.

The Chern number is obtained by integrating the Berry curvature $\Omega_z(k)$ over the BZ,

$$C = \frac{1}{2\pi} \int_{BZ} d^2k \Omega_z(k). \quad (7.3)$$

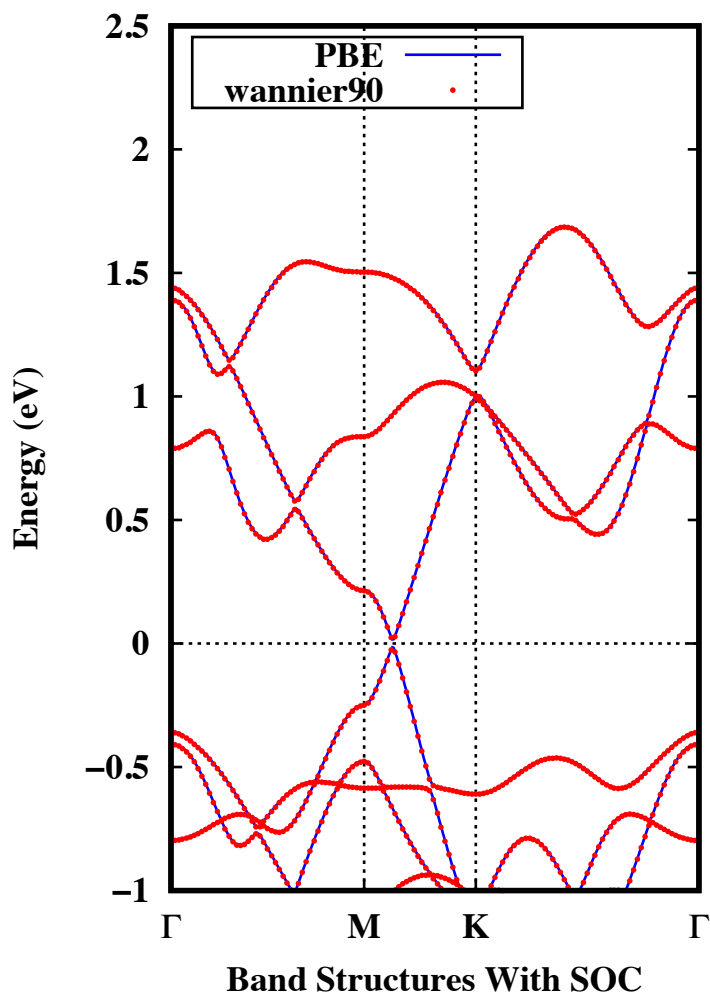


Fig. 7.3 The comparison of SOC band structures between DFT-PBE calculation and MLWF calculation.

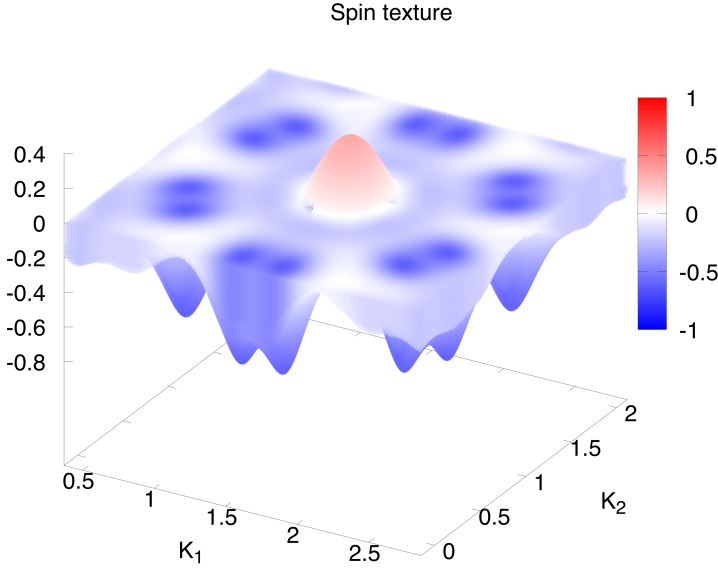


Fig. 7.4 The out of plane spin textures of the 1T-YN₂ monolayer.

The Chern number C is an integer and gives rise to the quantized Hall conductance: $\sigma_{xy} = Ce^2/h$. σ_{xy} is also known as the AHC, and the calculated chemical-potential-resolved AHC is shown in Fig. 7.5(a). A nontrivial gap of about 30 meV and a Chern number $C = 3$ can be deduced from the plateau near the Fermi level. The non-zero Chern number can also be confirmed by evaluating the electronic polarization P_e at discrete points in one primitive reciprocal lattice vector $k_y = k_i$ [113, 114, 111]. In another primitive reciprocal lattice vector k_x , the hybrid Wannier charge centers (WCCs) can be defined as

$$\bar{x}_n(k_y) = \frac{i}{2\pi} \int_{-\pi}^{\pi} dk_x \langle u_n(k_x, k_y) | \partial k_x | u_n(k_x, k_y) \rangle, \quad (7.4)$$

where $u_n(k_x, k_y)$ is the periodic part of the Bloch function $\psi_n(k)$. The sum of the hybrid WCCs \bar{x}_n will give the electronic polarization $P_e = e \sum_n \bar{x}_n(k_i)$ (e stands for the electronic charge) which is gauge invariant modulo a lattice vector. This brings about a well-defined physical observable ΔP_e under a continuous deformation of the system. Thus the Chern number is given by

$$C = \frac{1}{e} \Delta P_e = \frac{1}{e} (P_e(2\pi) - P_e(0)). \quad (7.5)$$

As can be seen from Fig. 7.5(b) which was calculated by WannierTools [350], the electronic polarization P_e shifts upwards with the winding number 3, so the Chern number $C = 3$.

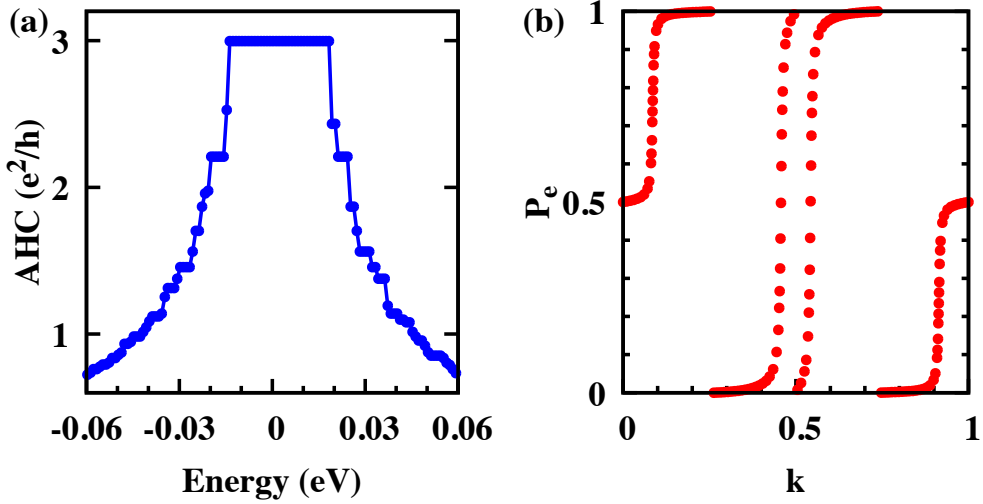


Fig. 7.5 (a) The chemical-potential-resolved AHC when the Fermi level is shifted to zero. (b) The change in the electronic polarization P_e .

According to the bulk-edge correspondence [76], the non-zero Chern number is closely related to the number of nontrivial chiral edge states that emerge inside the bulk gap of a semi-infinite system. With an effective concept of principle layers, an iterative procedure to calculate the Green's function for a semi-infinite system is employed. The momentum and energy dependence of the local density of states at the edge can be obtained from the imaginary part of the surface Green's function:

$$A(k, \omega) = -\frac{1}{\pi} \lim_{\eta \rightarrow 0^+} \text{ImTr}G_s(k, \omega + i\eta), \quad (7.6)$$

and the results are shown in Fig. 7.6. It is clear that there are three gapless chiral edge states that emerge inside the bulk gap connecting the valence and conduction bands and corresponding to a Chern number $C = 3$.

7.4 Possibility of Experimental Realization

In the following section, we will discuss the possibility of experimentally realizing the YN_2 monolayer. Notice that the lattice constant of 1T- YN_2 is close to that of the GaSe

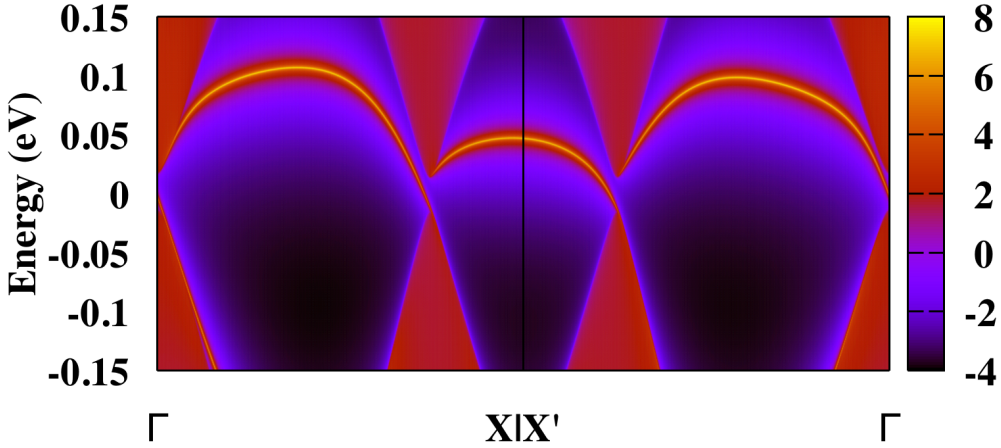


Fig. 7.6 Momentum and energy dependence of local density of states (log-scale) for the states at the edge of a semi-infinite plane ($\bar{1}10$).

monolayer, which has been realized experimentally [400] and therefore is expected to be a suitable substrate. We used the semiconducting GaSe monolayer as the substrate for the YN₂ monolayer. We found there are six kinds of highly symmetrical stacking models (A, B, C, D, E, and F) for the heterostructure (see Fig. 7.7(a)), which are similar to those of the high-buckled silicene on MoS₂ substrate [187]. First-principles calculations including vdW interactions resulted in a lattice constant of YN₂ of 3.765 Å, which is slightly smaller than the PBE result (3.776 Å) without vdW interactions. Comparing the lattice constant of the GaSe monolayer (3.804 Å), the lattice mismatch between the two monolayers is only 1.0%, which is far smaller than that of the high-buckled silicene on MoS₂ substrate (20.8%) [193], indicating its feasibility for experimental synthesis. Then we calculated the energy and the band structures of the six heterostructures without and with SOC effect. From Table 7.1, we can clearly see that the energy is related to the interlayer distance (h) between the two monolayers. Stacking model B shows the lowest energy with the smallest distance h and stacking model C/F shows the highest energy with the largest distance h . It can be easily understood that the smaller h , the stronger the interactions between the monolayers. All the six vdW YN₂/GaSe heterostructures show similar band structures as shown in Fig. 7.7(b). Not only the energy, but also the band gap without SOC is influenced by h . Comparing the other stacking models (A, B, D, and E), the band gap without SOC of the C/F is smaller, 16.6 meV, which indicates that the effect from the substrate is small. When considering SOC effect, changing the band gap with different size is related with the stacking style. On the other hand, we found that stacking

model C/F can keep its nontrivial topological properties with a Chern number $C = 3$, but other stacking models cannot keep the nontrivial properties ($C = 0$) due to the strong interaction with the substrate. To demonstrate the nontrivial topological properties, we calculated the corresponding edge states shown in Fig. 7.7(c) and Fig. 7.8. Notice that the stacking model C/F has similar three chiral edge states as the single 1T-YN₂ monolayer in the semi-infinite plane ($\bar{1}10$).

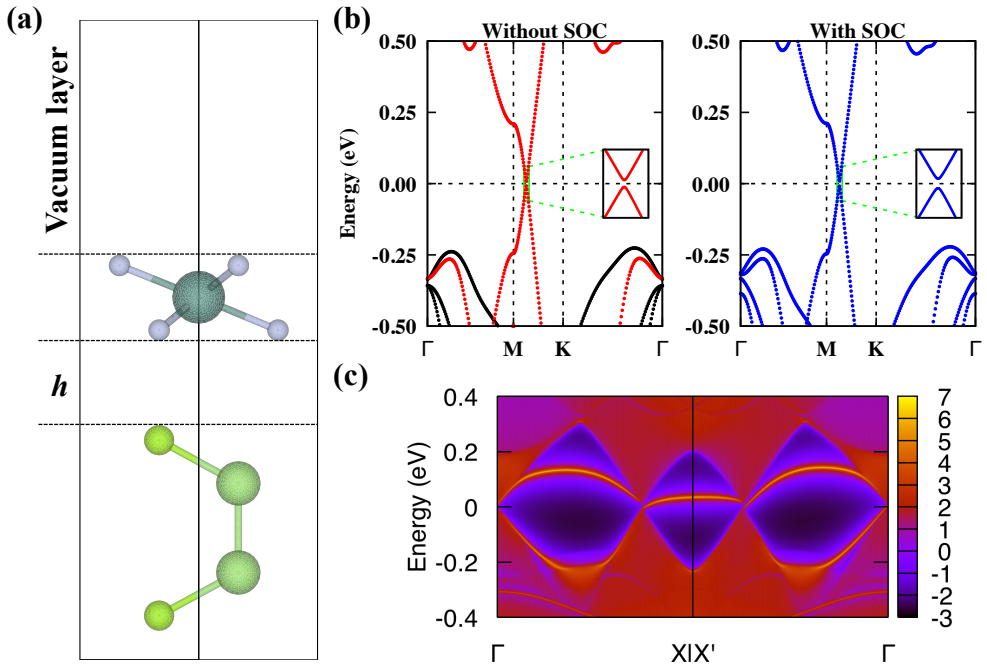


Fig. 7.7 (a) Side view of the YN₂/GaSe heterostructure with stacking model C along the $(\bar{1}10)$ direction. h indicates the interlayer distance. (b) The band structures of heterostructure C without SOC (left) and with SOC (right). The spin up band structure is plotted with black dots and the spin down band structure is given by red dots. The insets demonstrate the avoided band crossings. (c) Momentum and energy dependence of local density of states for the states at the edge of heterostructure C.

The nontrivial topological properties of the YN₂/GaSe heterostructure C/F is related with the interlayer distance (h), which may need some manipulations in experiment, and their energy is slightly higher than the other heterostructures. Here, we propose another way to keep the nontrivial properties of the YN₂. We construct GaSe/YN₂/GaSe quantum well structures by inverting the original GaSe monolayer in the YN₂/GaSe heterostructure about the Y atom in the YN₂ monolayer. Then, we obtain the sandwiched quantum wells

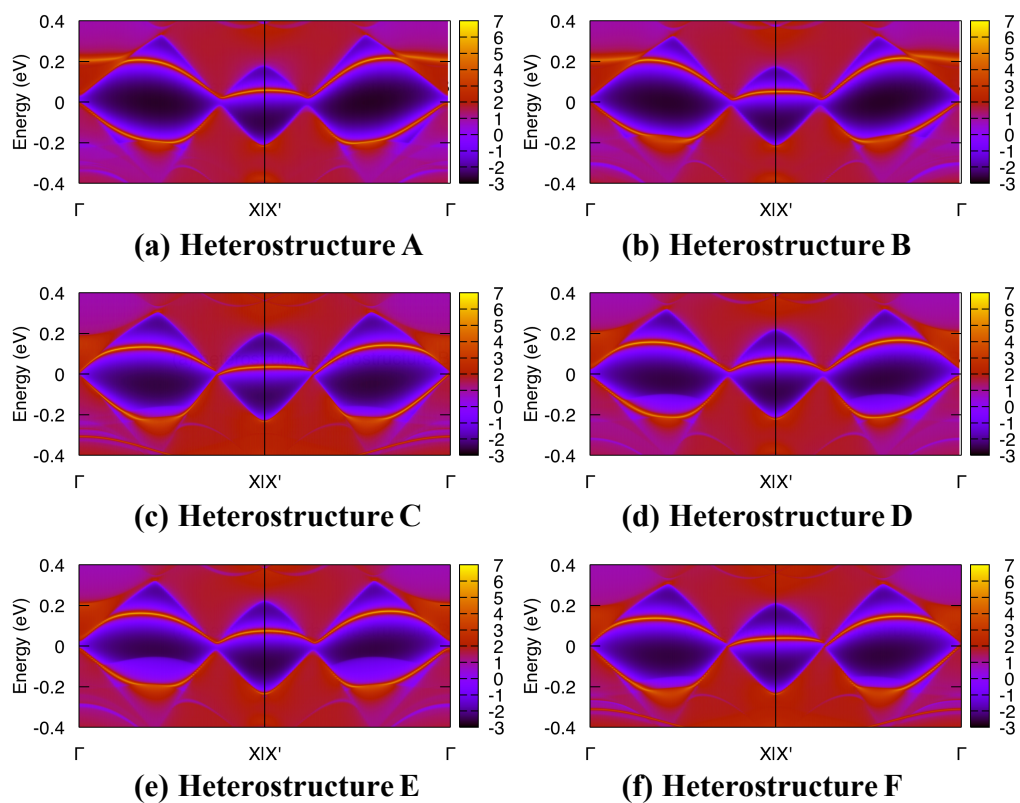


Fig. 7.8 Momentum and energy dependence of local density of states for the states at the edge of the heterostructures.

Table 7.1 The DFT calculated total energy E , lattice constant a , interlayer distance h between the YN_2 and GaSe layer, band gap Δ_{PBE} without SOC and Δ_{SOC} with SOC (at the Dirac point) of the six different stacked YN_2/GaSe heterostructures and GaSe/ YN_2/GaSe quantum wells. All results are calculated at the PBE level. The first lines of every item correspond to the YN_2/GaSe heterostructures, and the second lines correspond to the GaSe/ YN_2/GaSe quantum wells.

Six models	A	B	C	D	E	F
E (eV)	-37.450	-37.470	-37.302	-37.353	-37.357	-37.300
	-53.624	-53.666	-53.324	-53.436	-53.434	-53.320
a (Å)	3.800	3.800	3.776	3.781	3.783	3.776
	3.813	3.813	3.777	3.789	3.790	3.780
h (Å)	2.402	2.338	3.030	2.739	2.675	3.037
	2.405	2.341	2.977	2.748	2.683	3.028
Δ_{PBE} (meV)	69.0	65.2	16.6	62.8	69.0	16.6
	0	0	0	0	0	0
Δ_{SOC} (meV)	39.6	95.0	18.1	90.9	41.5	45.5
	35.1	31.9	25.8	28.5	26.4	30.8

as shown in Fig. 7.9. The lowest energy quantum well structure is the stacking model B, which is shown in Fig. 7.9(a). The corresponding band structures without and with SOC are shown in Fig. 7.9(b). In the quantum well structure, the band gap influenced by the GaSe substrate is close to 0 (thus it retains the Dirac cone), and SOC can induce a nontrivial band gap (31.9 meV) in the Dirac cone, but the Dirac cone will submerge in the band line at the Γ point, making the quantum well become semimetal. Due to the metallic bulk band structure, parts of the two edge states are absorbed by the bulk states as shown in Fig. 7.9(c). Only one edge state through the $X1X'$ point connecting the valence and conduction bands can be clearly seen. We could conclude that the GaSe/ YN_2/GaSe quantum well structures maintain the nontrivial topological properties of YN_2 monolayer, and thus has the potential to be observed in experiments.

Considering the Dirac cone preserved in the GaSe/ YN_2/GaSe quantum well structure, we also propose hexagonal boron nitride (hBN) monolayer as a possible substrate to construct the hBN/ YN_2/hBN quantum well structure (Fig. 7.10(a) and Fig. 7.11). The hBN substrate has been a popular substrate for graphene in experiment [180] and silicene/germanene in theories [322, 183, 401], and the similar hBN/ WTe_2/hBN quantum well has been realized experimentally for observing QSH effect at about 100 K [402]. The band structures of the hBN/ YN_2/hBN quantum well structure are shown in Figs. 7.10(b)

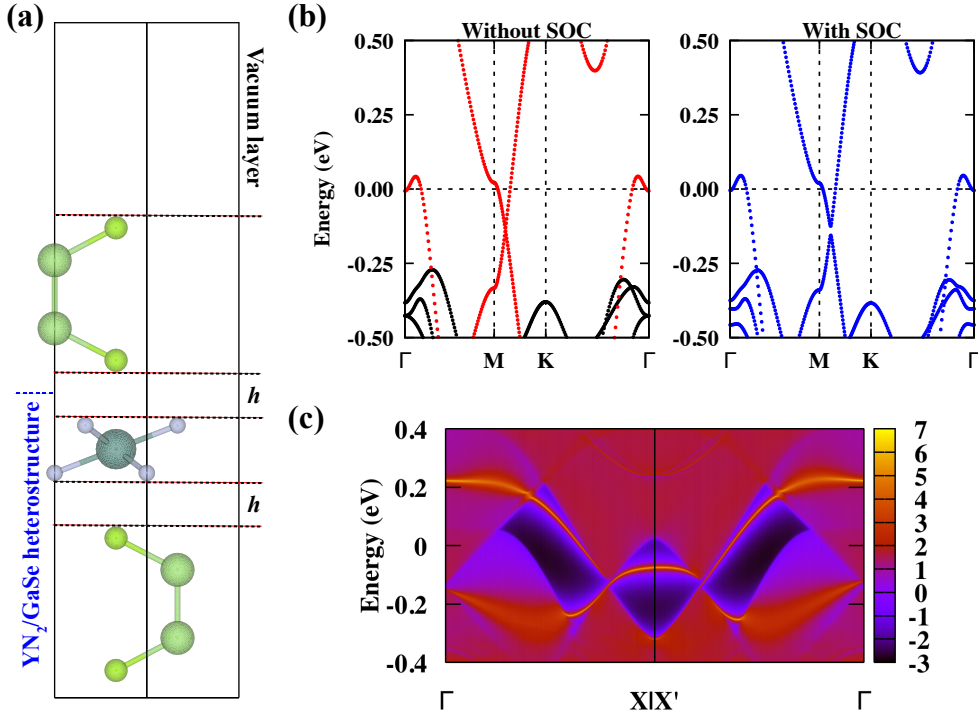


Fig. 7.9 (a) Side view of the GaSe/YN₂/GaSe quantum well with stacking model B from the (1 $\bar{1}$ 0) direction. h indicates the interlayer distance. (b) The band structures of quantum well B without SOC (left) and with SOC (right). The spin up band structure is plotted with black dots and the spin down structure is given by red dots. (c) Momentum and energy dependence of local density of states for the states at the edge of quantum well B.

and (c). Due to the band folding effect, the Dirac cone moves to the K- Γ line as shown in Fig. 7.10(b). Without SOC, the band gap is close to zero, and a band gap 32.6 meV is induced when considering the SOC effect. In contrast to the metallic GaSe/YN₂/GaSe quantum well, it is insulating with a sizable band gap. Thus, the hBN/YN₂/hBN quantum well is a good way for experimental synthesis of the YN₂ monolayer while keeping its topological nontrivial properties.

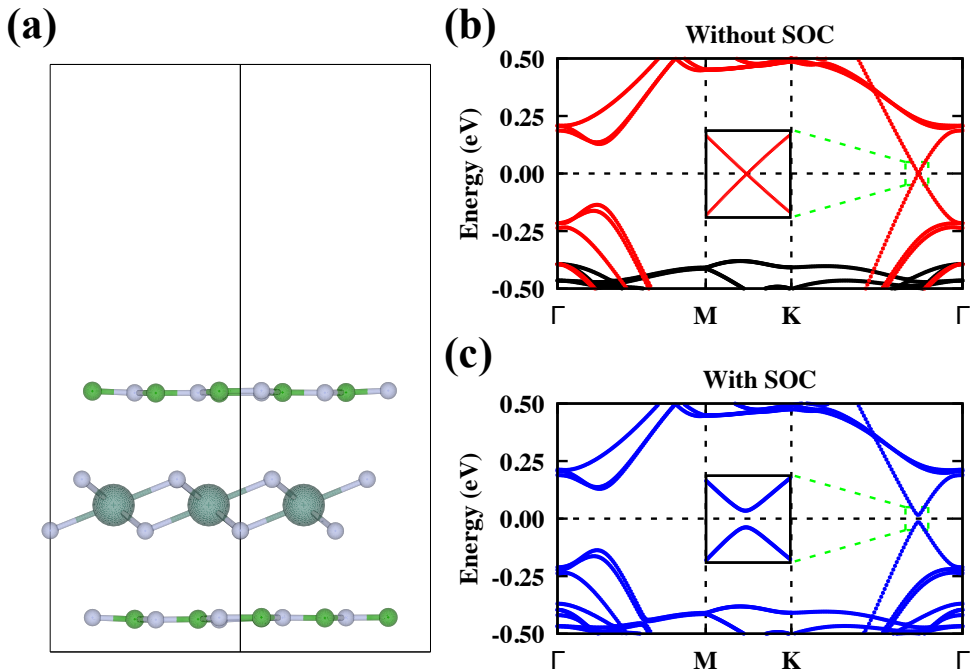


Fig. 7.10 (a) Side view of hBN/YN₂/hBN quantum well along the (110) direction. (b) The band structures of hBN/YN₂/hBN quantum well without SOC. The spin up band structure is plotted with black dots and the spin down band structure is given by red dots. The inset demonstrates the unavaoided band crossing. (c) The band structures of hBN/YN₂/hBN quantum well with SOC. The inset demonstrates the avoided band crossing.

7.5 Discussions

By the calculations of Berry curvature, the AHC, the Chern number, and the corresponding edge states, we confirm the topological nontrivial properties of the 1T-YN₂ monolayer. Also, we construct YN₂/GaSe heterostructures, GaSe/YN₂/GaSe and hBN/YN₂/hBN quantum wells to investigate the effect of substrates, and we show that the nontrivial

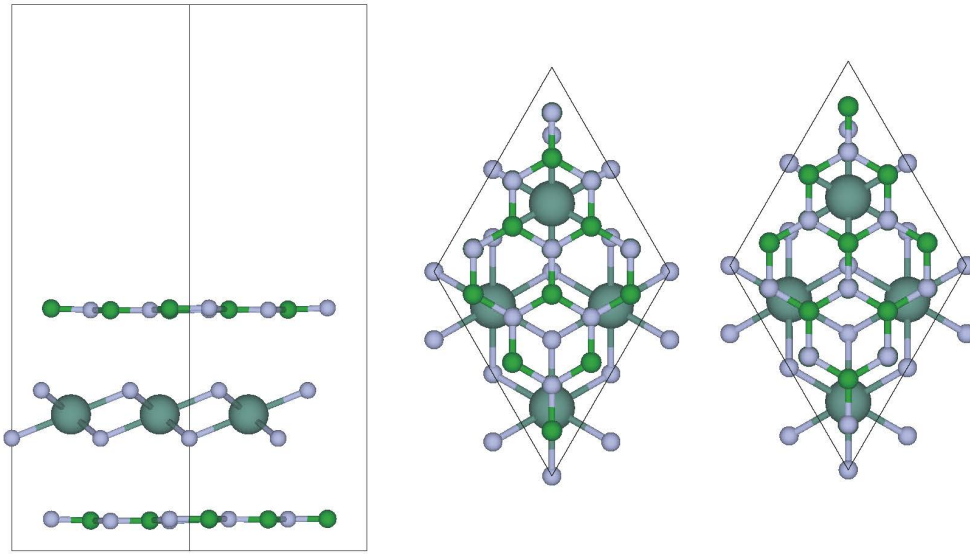


Fig. 7.11 Side view and vertical views of hBN/YN₂/hBN quantum well.

topological properties are preserved. The most significant points of our research can be summarized as follows:

1. The 1T-YN₂ monolayer has a nontrivial band gap of nearly 0.1 eV which is sufficient for the realization of QAH effect at room temperature. The found magnitude of the nontrivial band gap compares favorably to previous proposals [358, 403]. The largest band gap among the large number of QSH insulators is 1.08 eV [284, 285], but a band gap in QAH insulators of this order of magnitude has not been discovered. In recent reviews [358, 403], some systems have been proposed exhibiting large nontrivial band gaps (> 0.1 eV), but most of them are realized by functionalization methods, such as half functionalization of stanene with I atoms (≈ 340 meV) [367] and half functionalization of Bi (111) bilayer with H atoms (≈ 200 meV) [404, 405]. However, their stability still needs to be confirmed, and realizing such functionalization seems to be difficult to control experimentally. In contrast, note that the stability of 1T-YN₂ has been demonstrated by energetic and dynamical analysis [392]. On the other hand, we demonstrate that GaSe and hBN monolayers are favorable substrates to construct heterostructures and quantum wells while keeping the nontrivial topological properties of 1T-YN₂ monolayer. Since MoN₂ has been realized in experiment [388] and its monolayer stability has

been predicted [389], it seems likely that the realization of 1T-YN₂ monolayer is also possible.

2. Unlike the quantum Hall effect in which the Chern number can be tuned by changing the magnetic field or varying the Fermi level, the Chern number for intrinsic QAH effects in realistic materials are mostly limited to ± 1 and ± 2 [358, 403, 406]. QAH insulators with high Chern number and corresponding nontrivial chiral edge states are rarely reported. These nontrivial edge states will provide strong currents and signals which are significant in experiments. For example, more evidences should be observed in the QAH insulator/*s*-wave superconductor heterostructure for the chiral Majorana edge modes, which has been predicted to be able to realize robust topological quantum computing [380]. Thus, the stable 1T-YN₂ monolayer with a high Chern number is expected to lead to important applications in experiments.
3. To our knowledge, this is the first time that the QAH effect is predicted in a 2D TMN material. At present, the topological QSH effect was predicted in 1T' TMDs [384]. On the other hand, some TMD monolayers with square lattice [274] and hexagonal lattice [232] have also been predicted to be 2D topological insulators, but such structures have yet not been observed experimentally. Here, we report that the QAH effect can be realized in the 1T structure of TMN, which is a common structure for TMDs in experiment.

7.6 Conclusion

In conclusion, we investigated the electronic band structure of 1T-YN₂ monolayer by first-principles calculations in the case of SOC and observed an intrinsic QAH effect. A large nontrivial band gap (≈ 0.1 eV) and high Chern number ($C = 3$) were found. We calculated the Berry curvature and AHC to demonstrate the nontrivial topological properties. Three nontrivial gapless chiral edge states were found which provide strong evidence for the realization of the QAH effect in experiments. Moreover, we propose different substrates, such as GaSe and hBN monolayers, for the possible experimental realization of the nontrivial topological properties in the YN₂/GaSe heterostructures, GaSe/YN₂/GaSe and hBN/YN₂/hBN quantum wells. The prediction of the QAH effect in the 1T-YN₂ monolayer provides a different type of structure and material for the investigation of QAH insulators in the TM compounds.

Chapter 8

Summary and Outlook

8.1 Summary

Graphene is the most famous 2D Dirac materials since 2004. In the past ten years, the study of graphene has made large contributions to theory, experiment, and applications. Its influence is not only in physics, but also in many other fields. From the point of view of the Dirac band structure of graphene, this thesis address as two main questions: 1) Can we find other elements forming a stable 2D lattice with Dirac points? and 2) Can we find other Dirac band structures?

For the first question, we proposed three different kinds of 2D Dirac materials. Using first-principles calculations, we predicted a new stable carbon monolayer, $H_{4,4,4}$ -graphyne. Adding the adjacent element of C in the periodic table, i.e. the N element, two kinds of dumbbell C_4N structures can be obtained. The three monolayers can be called C-based materials. They all show Dirac band structures with a linear relationship between energy and momentum and the SOC effect is too weak therefore can be neglected. These C-based monolayers show high Fermi velocities, making them promising materials for future high-speed electronic devices. Remarkable, the Fermi velocities of $H_{4,4,4}$ -graphyne are slightly higher than that of graphene. It is well known that there are many kinds of 2D carbon structures with a Dirac point, but their Fermi velocities are often lower than that of graphene. To our knowledge, the Fermi velocities of $H_{4,4,4}$ -graphyne are the highest Fermi velocities among all of the 2D carbon structures.

On the another hand, we tried to find some materials exhibiting a large SOC effect. Since it is difficult to see the SOC effect in materials containing only light elements,

and therefore we focused on materials having heavy elements, such as Bi. We proposed several Bi-based 2D topological insulators. The large nontrivial band gaps make it possible to realize the QSH effect at room temperature. Remarkable, we were able to tune band structure such that we obtain Dirac points when changing the SOC strength. Although large SOC effect can be found in those Bi-based 2D topological insulators, they did not show any magnetic properties.

In order to introduce magnetic properties, we tried transition metals. We predict a spin-polarized Dirac point in Y-based materials with ferromagnetic properties. The bands of spin-up and spin-down are separated and the Dirac point formed by the spin-down bands is at the Fermi level. Including SOC, a large nontrivial band gap is opened. The proposed Chern insulator 1T-YN₂ can be used to realized QAH effect.

In summary, we started with carbon, added different elements to achieve our targets, such as high Fermi velocity, SOC effect, topological properties and magnetic properties. Those properties are expected to be investigated experimentally and may lead to applications of nano-electronic devices. In all search for different 2D Dirac materials, we also showed the different origins for the occurrence of Dirac points. Different from the single Dirac cone of graphene, which is at the high symmetry point K, we found a distorted Dirac point, which is not located at a high symmetry point, and we also found double Dirac points, which originate from nodal line states. Different Dirac points are expected to result into different physical properties of 2D materials.

8.2 Outlook

In this thesis, we focused on the Dirac band structure of 2D materials. However, we considered only isolated 2D materials and their band structures. In a typical experiment and in the case of applications, monolayer materials are placed on substrates. In our future research, we should investigated the effect of substrates on these Dirac materials. Whether the Dirac points, SOC effect, topological properties, and magnetic properties are modified by substrates is an important question we will focus on in the future.

By some search algorithms, thousands of topological insulators can be predicted. However, topological superconductor is a novel quantum material, which combines topological properties and superconductive properties. In contrast to the extended literature on DFT calculations of topological insulators, the study of calculations of topological su-

perconductors is still in its infancy. Finding a suitable calculation method for topological superconductors will be another direction of our future study.

Chapter 9

Samenvatting

Grafeen is het meest bekende 2D Dirac-materiaal sinds 2004. In de afgelopen tien jaar heeft de studie van grafeen een grote bijdrage geleverd aan theorie, experiment en toepassingen. De invloed van dit onderzoek is niet alleen beperkt tot natuurkunde, maar heeft ook zijn weerslag gevonden in veel andere gebieden. Vanuit het standpunt van de Dirac-bandenstructuur van grafeen, concentreert dit proefschrift zich op twee hoofdvragen: 1) Zijn er andere elementen die een stabiel 2D-rooster vormen met Dirac-punten? en 2) Is het mogelijk om andere Dirac-bandenstructuren te bekomen?

Voor de eerste vraag hebben we drie verschillende soorten 2D Dirac-materialen onderzocht. Gebruik makend van eerste beginselen berekeningen, voorspelden we een nieuwe stabiele koolstofmonolaag, $H_{4,4,4}$ -graphyne. Toevoegen van het aangrenzende element van C in het periodiek systeem, d.w.z. het N element, hebben we twee soorten van haltervormige C_4N -structuren verkregen. De drie monolagen kunnen C-gebaseerd materialen worden genoemd. Ze tonen allemaal Dirac-bandenstructuren met een lineaire relatie tussen energie en het momentum en daar het SOC-effect zwak is, kan het daarom worden verwaarloosd. Deze C-gebaseerde monolagen vertonen hoge Fermi-snelheden, waardoor ze veelbelovende materialen zijn voor hoge snelheid elektronische apparaten. Opmerkelijk, de Fermi-snelheden van $H_{4,4,4}$ -graphyne zijn iets hoger dan dat van grafeen. Het is bekend dat er veel soorten 2D koolstofstructuren zijn met een Dirac-punt, maar hun Fermi-snelheden zijn vaak lager dan dat van grafeen. Voor zover wij weten, zijn de Fermi-snelheden van $H_{4,4,4}$ -graphyne het hoogst van alle 2D-koolstofstructuren.

Aan de andere kant probeerden we een aantal materialen te vinden die een groot SOC-effect vertoonden. Omdat het moeilijk is om het SOC-effect te zien in materialen die alleen

lichte elementen bevatten, hebben we onze aandacht gericht op materialen met zware elementen, zoals Bi. We hebben verschillende Bi-gebaseerde 2D topologische isolatoren gevonden. De grote niet-triviale bandkloof maakt het mogelijk om het QSH-effect bij kamertemperatuur te realiseren. Opmerkelijk, we waren in staat om de bandstructuur zo af te stemmen dat we Dirac-punten verkrijgen bij het veranderen van de SOC-sterkte. Hoewel we een groot SOC-effect vonden in deze op Bi gebaseerde 2D topologische isolatoren, vertoonden zij geen magnetische eigenschappen.

Om magnetische eigenschappen te introduceren, hebben we gebruik gemaakt van overgangsmetalen. We voorspellen een spin-gepolariseerd Dirac-punt in Y-gebaseerde materialen met ferromagnetische eigenschappen. De banden van spin-up en spin-down zijn nu gescheiden en het Dirac-punt gevormd door de spin-down banden is gelokaliseerd aan het Fermi-niveau. Indien we SOC in rekening brengen wordt een grote niet-triviale band gap geopend. De voorgestelde Chern-isolator 1T-YN₂ kan worden gebruikt om het QAH-effect te realiseren.

Samengevat, we zijn begonnen met koolstof, hebben verschillende elementen (nl. atomen) toegevoegd om onze doelen te bereiken, zoals hoge Fermi-snelheid, SOC-effect, topologische eigenschappen en magnetische eigenschappen. Van deze eigenschappen wordt verwacht dat ze in de toekomst experimenteel worden onderzocht en dat ze mogelijk tot toepassingen leiden in nano-elektronische apparaten. Bij de zoektocht naar verschillende typen van 2D Dirac-materialen hebben we telkens de verschillende oorsprong van het ontstaan van Dirac-punten aangetoond. Anders dan de enkele Dirac-kegel van grafeen, dat zich op het hoge symmetriepunt K bevindt, vonden we vervormde Dirac-punten die zich niet op een hoog symmetriepunt bevinden. Bovendien vonden we ook dubbele Dirac-punten, die afkomstig zijn van knoopljntoestanden. We verwachten dat deze verschillende Dirac-punten aanleiding zullen geven tot verschillende fysieke eigenschappen van 2D-materialen.

Bibliography

- [1] J. Güttinger, F. Molitor, C. Stampfer, S. Schnez, A. Jacobsen, S. Dröscher, T. Ihn, and K. Ensslin, “Transport through graphene quantum dots,” *Reports on Progress in Physics* **75**, 126502 (2012).
- [2] K. S. Novoselov, “Electric Field Effect in Atomically Thin Carbon Films,” *Science* **306**, 666 (2004).
- [3] A. K. Geim and K. S. Novoselov, “The rise of graphene,” *Nature Materials* **6**, 183 (2007).
- [4] C. Lee, X. Wei, J. W. Kysar, and J. Hone, “Measurement of the Elastic Properties and Intrinsic Strength of Monolayer Graphene,” *Science* **321**, 385 (2008).
- [5] K. S. Novoselov, A. K. Geim, S. V. Morozov, D. Jiang, M. I. Katsnelson, I. V. Grigorieva, S. V. Dubonos, and A. A. Firsov, “Two-dimensional gas of massless Dirac fermions in graphene,” *Nature* **438**, 197 (2005).
- [6] K. S. Novoselov, Z. Jiang, Y. Zhang, S. V. Morozov, H. L. Stormer, U. Zeitler, J. C. Maan, G. S. Boebinger, P. Kim, and A. K. Geim, “Room-Temperature Quantum Hall Effect in Graphene,” *Science* **315**, 1379 (2007).
- [7] A. A. Balandin, S. Ghosh, W. Bao, I. Calizo, D. Teweldebrhan, F. Miao, and C. N. Lau, “Superior Thermal Conductivity of Single-Layer Graphene,” *Nano Letters* **8**, 902 (2008).
- [8] K. I. Bolotin, K. J. Sikes, J. Hone, H. L. Stormer, and P. Kim, “Temperature-Dependent Transport in Suspended Graphene,” *Physical Review Letters* **101**, 096802 (2008).
- [9] A. Hirsch, “The era of carbon allotropes,” *Nature Materials* **9**, 868 (2010).
- [10] M. Nakajima, K. Hosaka, M. Yamauti, R. M. Foxton, and J. Tagami, “Bonding durability of a self-etching primer system to normal and caries-affected dentin under hydrostatic pulpal pressure in vitro,” *American Journal of Dentistry* **19**, 147 (2006).
- [11] S. Iijima and T. Ichihashi, “Single-shell carbon nanotubes of 1-nm diameter,” *Nature* **363**, 603 (1993).

- [12] Y. Li, L. Xu, H. Liu, and Y. Li, "Graphdiyne and graphyne: From theoretical predictions to practical construction," *Chemical Society Reviews* **43**, 2572 (2014).
- [13] M. M. Haley, "Synthesis and properties of annulenic subunits of graphyne and graphdiyne nanoarchitectures," *Pure and Applied Chemistry* **80**, 519 (2008).
- [14] F. Diederich and M. Kivala, "All-carbon scaffolds by rational design," *Advanced Materials* **22**, 803 (2010).
- [15] P. Rivera-Fuentes and F. Diederich, "Allenes in molecular materials," *Angewandte Chemie - International Edition* **51**, 2818 (2012).
- [16] R. H. Baughman, H. Eckhardt, and M. Kertesz, "Structure-property predictions for new planar forms of carbon: Layered phases containing sp² and sp atoms," *The Journal of Chemical Physics* **87**, 6687 (1987).
- [17] G. Li, Y. Li, H. Liu, Y. Guo, Y. Li, and D. Zhu, "Architecture of graphdiyne nanoscale films," *Chemical Communications* **46**, 3256 (2010).
- [18] N. K. Perkgöz and C. Sevik, "Vibrational and thermodynamic properties of α -, β -, γ -, and 6, 6, 12-graphyne structures," *Nanotechnology* **25**, 185701 (2014).
- [19] A. R. Puigdollers, G. Alonso, and P. Gamallo, "First-principles study of structural, elastic and electronic properties of α -, β - and γ -graphyne," *Carbon* **96**, 879 (2016).
- [20] K. Srinivasu and S. K. Ghosh, "Graphyne and graphdiyne: promising materials for nanoelectronics and energy storage applications," *The Journal of Physical Chemistry C* **116**, 5951 (2012).
- [21] P. Zhang, Q. Song, J. Zhuang, and X. J. Ning, "First-principles study of gas adsorption on Γ -graphyne," *Chemical Physics Letters* **689**, 185 (2017).
- [22] A. Ruiz-Puigdollers and P. Gamallo, "DFT study of the role of N- and B-doping on structural, elastic and electronic properties of α -, β - and γ -graphyne," *Carbon* **114**, 301 (2017).
- [23] Q. Li, Y. Li, Y. Chen, L. Wu, C. Yang, and X. Cui, "Synthesis of γ -graphyne by mechanochemistry and its electronic structure," *Carbon* **136**, 248 (2018).
- [24] J. v. Liebig, "About some nitrogen compounds," *Ann. Pharm* **10** (1834).
- [25] H. Huang, S. Yang, R. Vajtai, X. Wang, and P. M. Ajayan, "Pt-decorated 3D architectures built from graphene and graphitic carbon nitride nanosheets as efficient methanol oxidation catalysts," *Advanced Materials* **26**, 5160 (2014).
- [26] F. Goettmann, A. Fischer, M. Antonietti, and A. Thomas, "Metal-free catalysis of sustainable Friedel–Crafts reactions: direct activation of benzene by carbon nitrides to avoid the use of metal chlorides and halogenated compounds," *Chemical Communications* , 4530 (2006).

- [27] X. Wang, K. Maeda, A. Thomas, K. Takanebe, G. Xin, J. M. Carlsson, K. Domen, and M. Antonietti, "A metal-free polymeric photocatalyst for hydrogen production from water under visible light," *Nature Materials* **8**, 76 (2009).
- [28] X. Wang, X. Chen, A. Thomas, X. Fu, and M. Antonietti, "Metal-Containing Carbon Nitride Compounds: A New Functional Organic-Metal Hybrid Material," *Advanced Materials* **21**, 1609 (2009).
- [29] W.-J. Ong, L.-L. Tan, Y. H. Ng, S.-T. Yong, and S.-P. Chai, "Graphitic Carbon Nitride (g-C₃N₄)-Based Photocatalysts for Artificial Photosynthesis and Environmental Remediation: Are We a Step Closer To Achieving Sustainability?" *Chemical Reviews* **116**, 7159 (2016).
- [30] Y. Zhao, J. Zhang, and L. Qu, "Graphitic Carbon Nitride/Graphene Hybrids as New Active Materials for Energy Conversion and Storage," *ChemNanoMat* **1**, 298 (2015).
- [31] A. Zambon, J.-M. Mouesca, C. Gheorghiu, P. A. Bayle, J. Pécaut, M. Claeys-Bruno, S. Gambarelli, and L. Dubois, "s-Heptazine oligomers: promising structural models for graphitic carbon nitride," *Chemical Science* **7**, 945 (2016).
- [32] Y. Zheng, L. Lin, B. Wang, and X. Wang, "Graphitic Carbon Nitride Polymers toward Sustainable Photoredox Catalysis," *Angewandte Chemie International Edition* **54**, 12868 (2015).
- [33] E. Kroke, M. Schwarz, E. Horath-Bordon, P. Kroll, B. Noll, and A. D. Norman, "Tri-s-triazine derivatives. Part I. From trichloro-tri-s-triazine to graphitic C₃N₄ structures," *New Journal of Chemistry* **26**, 508 (2002).
- [34] J. Mahmood, E. K. Lee, M. Jung, D. Shin, I.-Y. Jeon, S.-M. Jung, H.-J. Choi, J.-M. Seo, S.-Y. Bae, S.-D. Sohn, N. Park, J. H. Oh, H.-J. Shin, and J.-B. Baek, "Nitrogenated holey two-dimensional structures," *Nature Communications* **6**, 6486 (2015).
- [35] J. Mahmood, E. K. Lee, M. Jung, D. Shin, H.-J. Choi, J.-M. Seo, S.-M. Jung, D. Kim, F. Li, M. S. Lah, N. Park, H.-J. Shin, J. H. Oh, and J.-B. Baek, "Two-dimensional polyaniline (C₃N) from carbonized organic single crystals in solid state," *Proceedings of the National Academy of Sciences* **113**, 7414 (2016).
- [36] E. Hall, "On a new action of the magnet on electric currents," *American Journal of Science* , 200 (1880).
- [37] K. von Klitzing, "The quantized Hall effect," *Reviews of Modern Physics* **58**, 519 (1986).
- [38] M. König, H. Buhmann, L. W. Molenkamp, T. Hughes, C.-X. Liu, X.-L. Qi, and S.-C. Zhang, "The Quantum Spin Hall Effect: Theory and Experiment," *Journal of the Physical Society of Japan* **77**, 031007 (2008).

- [39] J. E. Moore, "The birth of topological insulators," *Nature* **464**, 194 (2010).
- [40] M. Z. Hasan and C. L. Kane, "Colloquium : Topological insulators," *Reviews of Modern Physics* **82**, 3045 (2010).
- [41] X.-L. Qi and S.-C. Zhang, "The quantum spin Hall effect and topological insulators," *Physics Today* **63**, 33 (2010).
- [42] F. D. M. Haldane, "Model for a Quantum Hall Effect without Landau Levels: Condensed-Matter Realization of the "Parity Anomaly"," *Physical Review Letters* **61**, 2015 (1988).
- [43] S.-C. Zhang, "A Four-Dimensional Generalization of the Quantum Hall Effect," *Science* **294**, 823 (2001).
- [44] S. Murakami, "Dissipationless Quantum Spin Current at Room Temperature," *Science* **301**, 1348 (2003).
- [45] S. Murakami, N. Nagaosa, and S.-C. Zhang, "Spin-Hall Insulator," *Physical Review Letters* **93**, 156804 (2004).
- [46] J. Sinova, D. Culcer, Q. Niu, N. A. Sinitsyn, T. Jungwirth, and A. H. MacDonald, "Universal Intrinsic Spin Hall Effect," *Physical Review Letters* **92**, 126603 (2004).
- [47] C. L. Kane and E. J. Mele, "Quantum Spin Hall Effect in Graphene," *Physical Review Letters* **95**, 226801 (2005).
- [48] B. A. Bernevig and S.-C. Zhang, "Quantum Spin Hall Effect," *Physical Review Letters* **96**, 106802 (2006).
- [49] L. Fu and C. L. Kane, "Topological insulators with inversion symmetry," *Physical Review B* **76**, 045302 (2007).
- [50] L. Fu, C. L. Kane, and E. J. Mele, "Topological Insulators in Three Dimensions," *Physical Review Letters* **98**, 106803 (2007).
- [51] J. E. Moore and L. Balents, "Topological invariants of time-reversal-invariant band structures," *Physical Review B* **75**, 121306 (2007).
- [52] X.-L. Qi, T. L. Hughes, and S.-C. Zhang, "Topological field theory of time-reversal invariant insulators," *Physical Review B* **78**, 195424 (2008).
- [53] R. Roy, " Z_2 classification of quantum spin Hall systems: An approach using time-reversal invariance," *Physical Review B* **79**, 195321 (2009).
- [54] B. A. Bernevig, T. L. Hughes, and S.-C. Zhang, "Quantum spin Hall effect and topological phase transition in HgTe quantum wells," *Science* **314**, 1757 (2006).

- [55] M. König, S. Wiedmann, C. Brune, A. Roth, H. Buhmann, L. W. Molenkamp, X.-L. Qi, and S.-C. Zhang, “Quantum Spin Hall Insulator State in HgTe Quantum Wells,” *Science* **318**, 766 (2007).
- [56] A. Roth, C. Brune, H. Buhmann, L. W. Molenkamp, J. Maciejko, X.-L. Qi, and S.-C. Zhang, “Nonlocal Transport in the Quantum Spin Hall State,” *Science* **325**, 294 (2009).
- [57] C. Day, “Quantum spin Hall effect shows up in a quantum well insulator, just as predicted,” *Physics Today* **61**, 19 (2008).
- [58] S. Wu, V. Fatemi, Q. D. Gibson, K. Watanabe, T. Taniguchi, R. J. Cava, and P. Jarillo-Herrero, “Observation of the quantum spin Hall effect up to 100 kelvin in a monolayer crystal,” *Science* **359**, 76 (2018).
- [59] F. Zheng, C. Cai, S. Ge, X. Zhang, X. Liu, H. Lu, Y. Zhang, J. Qiu, T. Taniguchi, K. Watanabe, S. Jia, J. Qi, J.-H. Chen, D. Sun, and J. Feng, “On the Quantum Spin Hall Gap of Monolayer 1T-WTe₂,” *Advanced Materials* **28**, 4845 (2016).
- [60] Y. Xia, D. Qian, D. Hsieh, L. Wray, A. Pal, H. Lin, A. Bansil, D. Grauer, Y. S. Hor, R. J. Cava, and M. Z. Hasan, “Observation of a large-gap topological-insulator class with a single Dirac cone on the surface,” *Nature Physics* **5**, 398 (2009).
- [61] H. Zhang, C.-X. Liu, X.-L. Qi, X. Dai, Z. Fang, and S.-C. Zhang, “Topological insulators in Bi₂Se₃, Bi₂Te₃ and Sb₂Te₃ with a single Dirac cone on the surface,” *Nature Physics* **5**, 438 (2009).
- [62] D. Hsieh, D. Qian, L. Wray, Y. Xia, Y. S. Hor, R. J. Cava, and M. Z. Hasan, “A topological Dirac insulator in a quantum spin Hall phase,” *Nature* **452**, 970 (2008).
- [63] Y. L. Chen, J. G. Analytis, J.-H. Chu, Z. K. Liu, S.-K. Mo, X. L. Qi, H. J. Zhang, D. H. Lu, X. Dai, Z. Fang, S. C. Zhang, I. R. Fisher, Z. Hussain, and Z.-X. Shen, “Experimental Realization of a Three-Dimensional Topological Insulator, Bi₂Te₃,” *Science* **325**, 178 (2009).
- [64] S. Perovic, “Why were Matrix Mechanics and Wave Mechanics considered equivalent?” *Studies in History and Philosophy of Science Part B: Studies in History and Philosophy of Modern Physics* **39**, 444 (2008).
- [65] S.-C. Zhang, “Topological states of quantum matter,” *Physics* **1**, 6 (2008).
- [66] S. Chadov, X. Qi, J. Kübler, G. H. Fecher, C. Felser, and S. C. Zhang, “Tunable multifunctional topological insulators in ternary Heusler compounds,” *Nature Materials* **9**, 541 (2010).
- [67] M. Franz, “Starting a new family,” *Nature Materials* **9**, 536 (2010).

- [68] B. Yan, C.-X. Liu, H.-J. Zhang, C.-Y. Yam, X.-L. Qi, T. Frauenheim, and S.-C. Zhang, "Theoretical prediction of topological insulators in thallium-based III-V-VI 2 ternary chalcogenides," *EPL (Europhysics Letters)* **90**, 37002 (2010).
- [69] H. Lin, L. A. Wray, Y. Xia, S. Xu, S. Jia, R. J. Cava, A. Bansil, and M. Z. Hasan, "Half-Heusler ternary compounds as new multifunctional experimental platforms for topological quantum phenomena," *Nature Materials* **9**, 546 (2010).
- [70] Y. L. Chen, Z. K. Liu, J. G. Analytis, J.-H. Chu, H. J. Zhang, B. H. Yan, S.-K. Mo, R. G. Moore, D. H. Lu, I. R. Fisher, S. C. Zhang, Z. Hussain, and Z.-X. Shen, "Single Dirac Cone Topological Surface State and Unusual Thermoelectric Property of Compounds from a New Topological Insulator Family," *Physical Review Letters* **105**, 266401 (2010).
- [71] T. Sato, K. Segawa, H. Guo, K. Sugawara, S. Souma, T. Takahashi, and Y. Ando, "Direct evidence for the Dirac-cone topological surface states in the ternary chalcogenide TlBiSe_2 ," *Physical Review Letters* **105**, 136802 (2010).
- [72] X.-L. Qi and S.-C. Zhang, "Topological insulators and superconductors," *Reviews of Modern Physics* **83**, 1057 (2011).
- [73] J. E. Avron, R. Seiler, and B. Simon, "Homotopy and Quantization in Condensed Matter Physics," *Physical Review Letters* **51**, 51 (1983).
- [74] B. Simon, "Holonomy, the Quantum Adiabatic Theorem, and Berry's Phase," *Physical Review Letters* **51**, 2167 (1983).
- [75] K. Von Klitzing, "25 Years of Quantum Hall Effect (QHE) A Personal View on the Discovery, Physics and Applications of this Quantum Effect," in *The Quantum Hall Effect* (Springer, 2005) pp. 1–21.
- [76] Y. Hatsugai, "Chern number and edge states in the interger quantum hall effect," *Physical Review Letters* **71** (1993).
- [77] M. Onoda and N. Nagaosa, "Quantized Anomalous Hall Effect in Two-Dimensional Ferromagnets: Quantum Hall Effect in Metals," *Physical Review Letters* **90**, 206601 (2003).
- [78] R. Yu, W. Zhang, H.-J. Zhang, S.-C. Zhang, X. Dai, and Z. Fang, "Quantized anomalous Hall effect in magnetic topological insulators," *Science* **329**, 61 (2010).
- [79] Z. Qiao, S. A. Yang, W. Feng, W.-K. Tse, J. Ding, Y. Yao, J. Wang, and Q. Niu, "Quantum anomalous Hall effect in graphene from Rashba and exchange effects," *Physical Review B* **82**, 161414 (2010).
- [80] H. Jin, J. Im, and A. J. Freeman, "Topological and magnetic phase transitions in Bi_2Se_3 thin films with magnetic impurities," *Physical Review B* **84**, 134408 (2011).

- [81] A. Fedrizzi, R. Ursin, T. Herbst, M. Nespoli, R. Prevedel, T. Scheidl, F. Tiefenbacher, T. Jennewein, and A. Zeilinger, “High-fidelity transmission of entanglement over a high-loss free-space channel,” *Nature Physics* **5**, 389 (2009).
- [82] C.-Z. Chang, J. Zhang, X. Feng, J. Shen, Z. Zhang, M. Guo, K. Li, Y. Ou, P. Wei, L.-L. Wang, Z.-Q. Ji, Y. Feng, S. Ji, X. Chen, J. Jia, X. Dai, Z. Fang, S.-C. Zhang, K. He, Y. Wang, L. Lu, X.-C. Ma, and Q.-K. Xue, “Experimental Observation of the Quantum Anomalous Hall Effect in a Magnetic Topological Insulator,” *Science* **340**, 167 (2013).
- [83] J. G. Checkelsky, R. Yoshimi, A. Tsukazaki, K. S. Takahashi, Y. Kozuka, J. Falson, M. Kawasaki, and Y. Tokura, “Trajectory of the anomalous Hall effect towards the quantized state in a ferromagnetic topological insulator,” *Nature Physics* **10**, 731 (2014).
- [84] X. Kou, S.-T. Guo, Y. Fan, L. Pan, M. Lang, Y. Jiang, Q. Shao, T. Nie, K. Murata, J. Tang, Y. Wang, L. He, T.-K. Lee, W.-L. Lee, and K. L. Wang, “Scale-Invariant Quantum Anomalous Hall Effect in Magnetic Topological Insulators beyond the Two-Dimensional Limit,” *Physical Review Letters* **113**, 137201 (2014).
- [85] K. He, X.-C. Ma, X. Chen, L. Lü, Y.-Y. Wang, and Q.-K. Xue, “From magnetically doped topological insulator to the quantum anomalous Hall effect,” *Chinese Physics B* **22**, 067305 (2013).
- [86] H.-Z. Lu, A. Zhao, and S.-Q. Shen, “Quantum Transport in Magnetic Topological Insulator Thin Films,” *Physical Review Letters* **111**, 146802 (2013).
- [87] S.-g. Cheng, “The quantum anomalous Hall effect in a topological insulator thin film —The role of magnetic disorder,” *EPL (Europhysics Letters)* **105**, 57004 (2014).
- [88] Y. Ren, Z. Qiao, and Q. Niu, “Topological phases in two-dimensional materials: a review,” *Reports on Progress in Physics* **79**, 066501 (2016).
- [89] P. Hohenberg and W. Kohn, “Inhomogeneous electron gas,” *Physical Review* **136**, B864 (1964).
- [90] W. Kohn and L. J. Sham, “Self-Consistent Equations Including Exchange and Correlation Effects,” *Physical Review* **140**, A1133 (1965).
- [91] M. Born and R. Oppenheimer, “Zur Quantentheorie der Molekeln,” *Annalen der Physik* **389**, 457 (1927).
- [92] M. Levy, “Universal variational functionals of electron densities, first-order density matrices, and natural spin-orbitals and solution of the v -representability problem,” *Proceedings of the National Academy of Sciences* **76**, 6062 (1979).
- [93] J. P. Perdew and Y. Wang, “Accurate and simple analytic representation of the electron-gas correlation energy,” *Physical Review B* **45**, 13244 (1992).

- [94] J. P. Perdew and Y. Wang, "Erratum: Accurate and simple analytic representation of the electron-gas correlation energy [Phys. Rev. B 45, 13244 (1992)]," *Physical Review B* **98**, 079904 (2018).
- [95] J. P. Perdew, K. Burke, and M. Ernzerhof, "Generalized Gradient Approximation Made Simple [Phys. Rev. Lett. 77, 3865 (1996)]," *Physical Review Letters* **78**, 1396 (1997).
- [96] C. Adamo and V. Barone, "Toward reliable density functional methods without adjustable parameters: The PBE0 model," *The Journal of Chemical Physics* **110**, 6158 (1999).
- [97] J. Heyd, G. E. Scuseria, and M. Ernzerhof, "Hybrid functionals based on a screened Coulomb potential," *The Journal of Chemical Physics* **118**, 8207 (2003).
- [98] J. Heyd, G. E. Scuseria, and M. Ernzerhof, "Erratum: "Hybrid functionals based on a screened Coulomb potential" [J. Chem. Phys. 118, 8207 (2003)]," *The Journal of Chemical Physics* **124**, 219906 (2006).
- [99] M. J. Lucero, T. M. Henderson, and G. E. Scuseria, "Improved semiconductor lattice parameters and band gaps from a middle-range screened hybrid exchange functional," *Journal of Physics: Condensed Matter* **24**, 145504 (2012).
- [100] G. Kresse and J. Furthmüller, "Efficient iterative schemes for ab initio total-energy calculations using a plane-wave basis set," *Physical Review B* **54**, 11169 (1996).
- [101] G. Kresse and J. Hafner, "Ab initio molecular dynamics for open-shell transition metals," *Physical Review B* **48**, 13115 (1993).
- [102] G. Kresse and D. Joubert, "From ultrasoft pseudopotentials to the projector augmented-wave method," *Physical Review B* **59**, 1758 (1999).
- [103] F. Bloch, "Elektron im periodischen Potential, Bändermodell des Festkörpers, Z," *Phys* **52**, 555 (1928).
- [104] J. C. Slater and G. F. Koster, "Simplified LCAO method for the periodic potential problem," *Physical Review* **94**, 1498 (1954).
- [105] H. Min, J. Hill, N. A. Sinitsyn, B. Sahu, L. Kleinman, and A. H. MacDonald, "Intrinsic and Rashba spin-orbit interactions in graphene sheets," *Physical Review B* **74**, 165310 (2006).
- [106] D. Huertas-Hernando, F. Guinea, and A. Brataas, "Spin-orbit coupling in curved graphene, fullerenes, nanotubes, and nanotube caps," *Physical Review B* **74**, 155426 (2006).
- [107] Y. Yao, F. Ye, X.-L. Qi, S.-C. Zhang, and Z. Fang, "Spin-orbit gap of graphene: First-principles calculations," *Physical Review B* **75**, 041401 (2007).

- [108] J. Boettger and S. Trickey, "First-principles calculation of the spin-orbit splitting in graphene," *Physical Review B* **75**, 121402 (2007).
- [109] M. Gmitra, S. Konschuh, C. Ertler, C. Ambrosch-Draxl, and J. Fabian, "Band-structure topologies of graphene: Spin-orbit coupling effects from first principles," *Physical Review B* **80**, 235431 (2009).
- [110] A. Wang, X. Zhang, and M. Zhao, "Topological insulator states in a honeycomb lattice of s-triazines," *Nanoscale* **6**, 11157 (2014).
- [111] D. Gresch, G. Autès, O. V. Yazyev, M. Troyer, D. Vanderbilt, B. A. Bernevig, and A. A. Soluyanov, "Z2Pack: Numerical implementation of hybrid Wannier centers for identifying topological materials," *Physical Review B* **95**, 075146 (2017).
- [112] T. Fukui, Y. Hatsugai, and H. Suzuki, "Chern numbers in discretized Brillouin zone: efficient method of computing (spin) Hall conductances," *Journal of the Physical Society of Japan* **74**, 1674 (2005).
- [113] A. A. Soluyanov and D. Vanderbilt, "Computing topological invariants without inversion symmetry," *Physical Review B* **83**, 235401 (2011).
- [114] R. Yu, X. L. Qi, A. Bernevig, Z. Fang, and X. Dai, "Equivalent expression of Z_2 topological invariant for band insulators using the non-Abelian Berry connection," *Physical Review B* **84**, 075119 (2011).
- [115] X. Dai, "DOI10.7693/wl20161201," .
- [116] O. V. Yazyev and Y. P. Chen, "Polycrystalline graphene and other two-dimensional materials," *Nature Nanotechnology* **9**, 755 (2014).
- [117] J. Lahiri, Y. Lin, P. Bozkurt, I. I. Oleynik, and M. Batzill, "An extended defect in graphene as a metallic wire," *Nature Nanotechnology* **5**, 326 (2010).
- [118] E. Cockayne, G. M. Rutter, N. P. Guisinger, J. N. Crain, P. N. First, and J. A. Stroscio, "Grain boundary loops in graphene," *Physical Review B* **83**, 195425 (2011).
- [119] G. Zheng, Y. Jia, S. Gao, and S.-H. Ke, "A planar carbon allotrope with linear bipentagon-octagon and hexagon arrangement," *Physica E: Low-dimensional Systems and Nanostructures* **87**, 107 (2017).
- [120] B. R. Sharma, A. Manjanath, and A. K. Singh, "pentahexoctite: A new two-dimensional allotrope of carbon," *Scientific Reports* **4**, 7164 (2015).
- [121] H. Sun, S. Mukherjee, M. Daly, A. Krishnan, M. H. Karigerasi, and C. V. Singh, "New insights into the structure-nonlinear mechanical property relations for graphene allotropes," *Carbon* **110**, 443 (2016).

- [122] H. Terrones, M. Terrones, E. Hernández, N. Grobert, J.-C. Charlier, and P. M. Ajayan, "New Metallic Allotropes of Planar and Tubular Carbon," *Physical Review Letters* **84**, 1716 (2000).
- [123] Z. Wang, X.-F. Zhou, X. Zhang, Q. Zhu, H. Dong, M. Zhao, and A. R. Oganov, "Phagraphene: A Low-Energy Graphene Allotrope Composed of 5–6–7 Carbon Rings with Distorted Dirac Cones," *Nano Letters* **15**, 6182 (2015).
- [124] X. Li, Q. Wang, and P. Jena, " ψ -Graphene: A New Metallic Allotrope of Planar Carbon with Potential Applications as Anode Materials for Lithium-Ion Batteries," *The Journal of Physical Chemistry Letters* **8**, 3234 (2017).
- [125] Y. Liu, G. Wang, Q. Huang, L. Guo, and X. Chen, "Structural and Electronic Properties of *T* Graphene: A Two-Dimensional Carbon Allotrope with Tetrarings," *Physical Review Letters* **108**, 225505 (2012).
- [126] S. Zhang, J. Zhou, Q. Wang, X. Chen, Y. Kawazoe, and P. Jena, "Penta-graphene: A new carbon allotrope," *Proceedings of the National Academy of Sciences* **112**, 2372 (2015).
- [127] B. G. Kim and H. J. Choi, "Graphyne: Hexagonal network of carbon with versatile Dirac cones," *Physical Review B* **86**, 115435 (2012).
- [128] M. Zhao, W. Dong, and A. Wang, "Two-dimensional carbon topological insulators superior to graphene," *Scientific Reports* **3**, 3532 (2013).
- [129] D. Malko, C. Neiss, and A. Görling, "Two-dimensional materials with Dirac cones: Graphynes containing heteroatoms," *Physical Review B* **86**, 045443 (2012).
- [130] Y. Qu, F. Li, and M. Zhao, "Efficient $^3\text{He}/^4\text{He}$ separation in a nanoporous graphenylene membrane," *Physical Chemistry Chemical Physics* **19**, 21522 (2017).
- [131] J. Kou, X. Zhou, H. Lu, F. Wu, and J. Fan, "Graphyne as the membrane for water desalination," *Nanoscale* **6**, 1865 (2014).
- [132] X. Kong, L. Li, O. Leenaerts, X.-J. Liu, and F. M. Peeters, "New group-V elemental bilayers: A tunable structure model with four-, six-, and eight-atom rings," *Physical Review B* **96**, 035123 (2017).
- [133] N. V. R. Nulakani and V. Subramanian, "Cp-Graphyne: A Low-Energy Graphyne Polymorph with Double Distorted Dirac Points," *ACS Omega* **2**, 6822 (2017).
- [134] G. Long, Y. Zhou, M. Jin, B. Kan, Y. Zhao, A. Gray-Weale, D.-e. Jiang, Y. Chen, and Q. Zhang, "Theoretical investigation on two-dimensional non-traditional carbon materials employing three-membered ring and four-membered ring as building blocks," *Carbon* **95**, 1033 (2015).

- [135] L. Z. Zhang, Z. F. Wang, Z. M. Wang, S. X. Du, H.-J. Gao, and F. Liu, "Highly Anisotropic Dirac Fermions in Square Graphynes," *The Journal of Physical Chemistry Letters* **6**, 2959 (2015).
- [136] H. Weng, X. Dai, and Z. Fang, "Topological semimetals predicted from first-principles calculations," *Journal of Physics: Condensed Matter* **28**, 303001 (2016).
- [137] Y.-J. Jin, R. Wang, J.-Z. Zhao, Y.-P. Du, C.-D. Zheng, L.-Y. Gan, J.-F. Liu, H. Xu, and S. Y. Tong, "The prediction of a family group of two-dimensional node-line semimetals," *Nanoscale* **9**, 13112 (2017).
- [138] Y. Wu, L.-L. Wang, E. Mun, D. D. Johnson, D. Mou, L. Huang, Y. Lee, S. L. Bud'ko, P. C. Canfield, and A. Kaminski, "Dirac node arcs in PtSn₄," *Nature Physics* **12**, 667 (2016).
- [139] G. Bian, T.-R. Chang, R. Sankar, S.-Y. Xu, H. Zheng, T. Neupert, C.-K. Chiu, S.-M. Huang, G. Chang, I. Belopolski, D. S. Sanchez, M. Neupane, N. Alidoust, C. Liu, B. Wang, C.-C. Lee, H.-T. Jeng, C. Zhang, Z. Yuan, S. Jia, A. Bansil, F. Chou, H. Lin, and M. Z. Hasan, "Topological nodal-line fermions in spin-orbit metal PbTaSe₂," *Nature Communications* **7**, 10556 (2016).
- [140] L. M. Schoop, M. N. Ali, C. Straßer, A. Topp, A. Varykhalov, D. Marchenko, V. Duppel, S. S. P. Parkin, B. V. Lotsch, and C. R. Ast, "Dirac cone protected by non-symmorphic symmetry and three-dimensional Dirac line node in ZrSiS," *Nature Communications* **7**, 11696 (2016).
- [141] M. Neupane, I. Belopolski, M. M. Hosen, D. S. Sanchez, R. Sankar, M. Szlowska, S.-Y. Xu, K. Dimitri, N. Dhakal, P. Maldonado, P. M. Oppeneer, D. Kaczorowski, F. Chou, M. Z. Hasan, and T. Durakiewicz, "Observation of topological nodal fermion semimetal phase in ZrSiS," *Physical Review B* **93**, 201104 (2016).
- [142] G. Bian, T.-R. Chang, H. Zheng, S. Velury, S.-Y. Xu, T. Neupert, C.-K. Chiu, S.-M. Huang, D. S. Sanchez, I. Belopolski, N. Alidoust, P.-J. Chen, G. Chang, A. Bansil, H.-T. Jeng, H. Lin, and M. Z. Hasan, "Drumhead surface states and topological nodal-line fermions in TlTaSe₂," *Physical Review B* **93**, 121113 (2016).
- [143] H. Weng, Y. Liang, Q. Xu, R. Yu, Z. Fang, X. Dai, and Y. Kawazoe, "Topological node-line semimetal in three-dimensional graphene networks," *Physical Review B* **92**, 045108 (2015).
- [144] L. S. Xie, L. M. Schoop, E. M. Seibel, Q. D. Gibson, W. Xie, and R. J. Cava, "A new form of Ca₃P₂ with a ring of Dirac nodes," *APL Materials* **3**, 083602 (2015).
- [145] Y.-H. Chan, C.-K. Chiu, M. Y. Chou, and A. P. Schnyder, "Ca₃P₂ and other topological semimetals with line nodes and drumhead surface states," *Physical Review B* **93**, 205132 (2016).

- [146] S. Nie, H. Weng, and F. B. Prinz, "Topological nodal-line semimetals in ferromagnetic rare-earth-metal monohalides," *Physical Review B* **99**, 035125 (2019).
- [147] R. Yu, H. Weng, Z. Fang, X. Dai, and X. Hu, "Topological Node-Line Semimetal and Dirac Semimetal State in Antiperovskite Cu_3PdN ," *Physical Review Letters* **115**, 036807 (2015).
- [148] J.-T. Wang, H. Weng, S. Nie, Z. Fang, Y. Kawazoe, and C. Chen, "Body-Centered Orthorhombic C_{16} : A Novel Topological Node-Line Semimetal," *Physical Review Letters* **116**, 195501 (2016).
- [149] R. Yu, Z. Fang, X. Dai, and H. Weng, "Topological nodal line semimetals predicted from first-principles calculations," *Frontiers of Physics* **12**, 127202 (2017).
- [150] B. Feng, B. Fu, S. Kasamatsu, S. Ito, P. Cheng, C.-C. Liu, Y. Feng, S. Wu, S. K. Mahatha, P. Sheverdyeva, P. Moras, M. Arita, O. Sugino, T.-C. Chiang, K. Shimada, K. Miyamoto, T. Okuda, K. Wu, L. Chen, Y. Yao, and I. Matsuda, "Experimental realization of two-dimensional Dirac nodal line fermions in monolayer Cu_2Si ," *Nature Communications* **8**, 1007 (2017).
- [151] B. Yang, X. Zhang, and M. Zhao, "Dirac node lines in two-dimensional Lieb lattices," *Nanoscale* **9**, 8740 (2017).
- [152] J.-L. Lu, W. Luo, X.-Y. Li, S.-Q. Yang, J.-X. Cao, X.-G. Gong, and H.-J. Xiang, "Two-Dimensional Node-Line Semimetals in a Honeycomb-Kagome Lattice," *Chinese Physics Letters* **34**, 057302 (2017).
- [153] J. P. Perdew, K. Burke, and M. Ernzerhof, "Generalized Gradient Approximation Made Simple," *Physical Review Letters* **77**, 3865 (1996).
- [154] A. Togo and I. Tanaka, "First principles phonon calculations in materials science," *Scripta Materialia* **108**, 1 (2015).
- [155] W.-J. Yin, Y.-E. Xie, L.-M. Liu, R.-Z. Wang, X.-L. Wei, L. Lau, J.-X. Zhong, and Y.-P. Chen, "R-graphyne: a new two-dimensional carbon allotrope with versatile Dirac-like point in nanoribbons," *Journal of Materials Chemistry A* **1**, 5341 (2013).
- [156] H. Zhang, H. Pan, M. Zhang, and Y. Luo, "First-principles prediction of a new planar hydrocarbon material: half-hydrogenated 14,14,14-graphyne," *Physical Chemistry Chemical Physics* **18**, 23954 (2016).
- [157] N. V. R. Nulakani and V. Subramanian, "A Theoretical Study on the Design, Structure, and Electronic Properties of Novel Forms of Graphynes," *The Journal of Physical Chemistry C* **120**, 15153 (2016).
- [158] A. Wang, L. Li, X. Wang, H. Bu, and M. Zhao, "Graphyne-based carbon allotropes with tunable properties: From Dirac fermion to semiconductor," *Diamond and Related Materials* **41**, 65 (2014).

- [159] Y. Qu, F. Li, and M. Zhao, "Efficient hydrogen isotopologues separation through a tunable potential barrier: The case of a C₂N membrane," *Scientific Reports* **7**, 1483 (2017).
- [160] F. Li, Y. Qu, and M. Zhao, "Efficient helium separation of graphitic carbon nitride membrane," *Carbon* **95**, 51 (2015).
- [161] B. P. Biswal, H. D. Chaudhari, R. Banerjee, and U. K. Kharul, "Chemically Stable Covalent Organic Framework (COF)-Polybenzimidazole Hybrid Membranes: Enhanced Gas Separation through Pore Modulation," *Chemistry - A European Journal* **22**, 4695 (2016).
- [162] J. Li, Z. Xie, Y. Xiong, Z. Li, Q. Huang, S. Zhang, J. Zhou, R. Liu, X. Gao, C. Chen, L. Tong, J. Zhang, and Z. Liu, "Architecture of β -Graphdiyne-Containing Thin Film Using Modified Glaser-Hay Coupling Reaction for Enhanced Photocatalytic Property of TiO₂," *Advanced Materials* **29**, 1700421 (2017).
- [163] J. Li, Y. Xiong, Z. Xie, X. Gao, J. Zhou, C. Yin, L. Tong, C. Chen, Z. Liu, and J. Zhang, "Template Synthesis of an Ultrathin β -Graphdiyne-Like Film Using the Eglinton Coupling Reaction," *ACS Applied Materials & Interfaces* **11**, 2734 (2019).
- [164] J. Zhang, R. Wang, X. Zhu, A. Pan, C. Han, X. Li, Dan Zhao, C. Ma, W. Wang, H. Su, and C. Niu, "Pseudo-topotactic conversion of carbon nanotubes to T-carbon nanowires under picosecond laser irradiation in methanol," *Nature Communications* **8**, 683 (2017).
- [165] X.-L. Sheng, Q.-B. Yan, F. Ye, Q.-R. Zheng, and G. Su, "T-Carbon: A Novel Carbon Allotrope," *Physical Review Letters* **106**, 155703 (2011).
- [166] G. F. Emerson, L. Watts, and R. Pettit, "Cyclobutadiene- and Benzocyclobutadiene-Iron Tricarbonyl Complexes¹," *Journal of the American Chemical Society* **87**, 131 (1965).
- [167] H. Kollmar and V. Staemmler, "A theoretical study of the structure of cyclobutadiene," *Journal of the American Chemical Society* **99**, 3583 (1977).
- [168] Y. Cheng, X. Feng, X. Cao, B. Wen, Q. Wang, Y. Kawazoe, and P. Jena, "Body-Centered Tetragonal C₁₆: A Novel Topological Node-Line Semimetallic Carbon Composed of Tetrarings," *Small* **13**, 1602894 (2017).
- [169] Q. Li, Y. Li, Y. Chen, L. Wu, C. Yang, and X. Cui, "Synthesis of γ -graphyne by mechanochemistry and its electronic structure," *Carbon* **136**, 248 (2018).
- [170] J. Gao, J. Li, Y. Chen, Z. Zuo, Y. Li, H. Liu, and Y. Li, "Architecture and properties of a novel two-dimensional carbon material-graphtetrayne," *Nano Energy* **43**, 192 (2018).

- [171] Q.-S. Du, P.-D. Tang, H.-L. Huang, F.-L. Du, K. Huang, N.-Z. Xie, S.-Y. Long, Y.-M. Li, J.-S. Qiu, and R.-B. Huang, "A new type of two-dimensional carbon crystal prepared from 1,3,5-trihydroxybenzene," *Scientific Reports* **7**, 40796 (2017).
- [172] L.-C. Xu, A. Du, and L. Kou, "Hydrogenated borophene as a stable two-dimensional Dirac material with an ultrahigh Fermi velocity," *Physical Chemistry Chemical Physics* **18**, 27284 (2016).
- [173] L. Li, X. Kong, O. Leenaerts, X. Chen, B. Sanyal, and F. M. Peeters, "Carbon-rich carbon nitride monolayers with Dirac cones: Dumbbell C₄N," *Carbon* **118**, 285 (2017).
- [174] D. Malko, C. Neiss, F. Viñes, and A. Görling, "Competition for Graphene: Graphynes with Direction-Dependent Dirac Cones," *Physical Review Letters* **108**, 086804 (2012).
- [175] L. Li, O. Leenaerts, X. Kong, X. Chen, M. Zhao, and F. M. Peeters, "Gallium bismuth halide GaBi-X₂ (X = I, Br, Cl) monolayers with distorted hexagonal framework: Novel room-temperature quantum spin Hall insulators," *Nano Research* **10**, 2168 (2017).
- [176] X. Kong, L. Li, O. Leenaerts, W. Wang, X.-J. Liu, and F. M. Peeters, "Quantum anomalous Hall effect in a stable 1T-YN₂ monolayer with a large nontrivial bandgap and a high Chern number," *Nanoscale* **10**, 8153 (2018).
- [177] C. Niu, P. M. Buhl, G. Bihlmayer, D. Wortmann, Y. Dai, S. Blügel, and Y. Mokrousov, "Two-dimensional topological nodal line semimetal in layered X₂Y (X = Ca, Sr, and Ba; Y = As, Sb, and Bi)," *Physical Review B* **95**, 235138 (2017).
- [178] N. V. R. Nulakani and V. Subramanian, "Computational realization of Dirac nodal point and Dirac nodal loop fermions in novel β -graphyne analogues," *Journal of Materials Chemistry C* **6**, 7626 (2018).
- [179] M. Wu, Z. Wang, J. Liu, W. Li, H. Fu, L. Sun, X. Liu, M. Pan, H. Weng, M. Dincă, L. Fu, and J. Li, "Conetronics in 2D metal-organic frameworks: double/half Dirac cones and quantum anomalous Hall effect," *2D Materials* **4**, 015015 (2016).
- [180] C. R. Dean, A. F. Young, I. Meric, C. Lee, L. Wang, S. Sorgenfrei, K. Watanabe, T. Taniguchi, P. Kim, K. L. Shepard, and J. Hone, "Boron nitride substrates for high-quality graphene electronics," *Nature Nanotechnology* **5**, 722 (2010).
- [181] W. Yang, G. Chen, Z. Shi, C.-C. Liu, L. Zhang, G. Xie, M. Cheng, D. Wang, R. Yang, D. Shi, K. Watanabe, T. Taniguchi, Y. Yao, Y. Zhang, and G. Zhang, "Epitaxial growth of single-domain graphene on hexagonal boron nitride," *Nature Materials* **12**, 792 (2013).

- [182] X. Zhao, L. Li, and M. Zhao, "Lattice match and lattice mismatch models of graphene on hexagonal boron nitride from first principles," *Journal of Physics: Condensed Matter* **26**, 095002 (2014).
- [183] L. Li, X. Wang, X. Zhao, and M. Zhao, "Moiré superstructures of silicene on hexagonal boron nitride: A first-principles study," *Physics Letters A* **377**, 2628 (2013).
- [184] L. Li and M. Zhao, "First-principles identifications of superstructures of germanene on Ag(111) surface and h-BN substrate," *Physical Chemistry Chemical Physics* **15**, 16853 (2013).
- [185] J. Zhou, Z. Xie, R. Liu, X. Gao, J. Li, Y. Xiong, L. Tong, J. Zhang, and Z. Liu, "Synthesis of Ultrathin Graphdiyne Film Using a Surface Template," *ACS Applied Materials & Interfaces* **11**, 2632 (2019).
- [186] S. Grimme, J. Antony, S. Ehrlich, and H. Krieg, "A consistent and accurate ab initio parametrization of density functional dispersion correction (DFT-D) for the 94 elements H-Pu," *The Journal of Chemical Physics* **132**, 154104 (2010).
- [187] L. Li and M. Zhao, "Structures, Energetics, and Electronic Properties of Multifarious Stacking Patterns for High-Buckled and Low-Buckled Silicene on the MoS₂ Substrate," *The Journal of Physical Chemistry C* **118**, 19129 (2014).
- [188] E. Wang, X. Lu, S. Ding, W. Yao, M. Yan, G. Wan, K. Deng, S. Wang, G. Chen, L. Ma, J. Jung, A. V. Fedorov, Y. Zhang, G. Zhang, and S. Zhou, "Gaps induced by inversion symmetry breaking and second-generation Dirac cones in graphene/hexagonal boron nitride," *Nature Physics* **12**, 1111 (2016).
- [189] B. Feng, Z. Ding, S. Meng, Y. Yao, X. He, P. Cheng, L. Chen, and K. Wu, "Evidence of Silicene in Honeycomb Structures of Silicon on Ag(111)," *Nano Letters* **12**, 3507 (2012).
- [190] P. Vogt, P. De Padova, C. Quaresima, J. Avila, E. Frantzeskakis, M. C. Asensio, A. Resta, B. Ealet, and G. Le Lay, "Silicene: Compelling Experimental Evidence for Graphenelike Two-Dimensional Silicon," *Physical Review Letters* **108**, 155501 (2012).
- [191] D. Chiappe, C. Grazianetti, G. Tallarida, M. Fanciulli, and A. Molle, "Local Electronic Properties of Corrugated Silicene Phases," *Advanced Materials* **24**, 5088 (2012).
- [192] L. Meng, Y. Wang, L. Zhang, S. Du, R. Wu, L. Li, Y. Zhang, G. Li, H. Zhou, W. A. Hofer, and H.-J. Gao, "Buckled Silicene Formation on Ir(111)," *Nano Letters* **13**, 685 (2013).
- [193] D. Chiappe, E. Scalise, E. Cinquanta, C. Grazianetti, B. van den Broek, M. Fanciulli, M. Houssa, and A. Molle, "Two-Dimensional Si Nanosheets with Local Hexagonal Structure on a MoS₂ Surface," *Advanced Materials* **26**, 2096 (2014).

- [194] M. Derivaz, D. Dentel, R. Stephan, M.-C. Hanf, A. Mehdaoui, P. Sonnet, and C. Pirri, "Continuous Germanene Layer on Al(111)," *Nano Letters* **15**, 2510 (2015).
- [195] L. Zhang, P. Bampoulis, A. N. Rudenko, Q. Yao, A. van Houselt, B. Poelsema, M. I. Katsnelson, and H. J. W. Zandvliet, "Structural and Electronic Properties of Germanene on MoS₂," *Physical Review Letters* **116**, 256804 (2016).
- [196] J. Gou, Q. Zhong, S. Sheng, W. Li, P. Cheng, H. Li, L. Chen, and K. Wu, "Strained monolayer germanene with 1 × 1 lattice on Sb(111)," *2D Materials* **3**, 045005 (2016).
- [197] F.-f. Zhu, W.-j. Chen, Y. Xu, C.-l. Gao, D.-d. Guan, C.-h. Liu, D. Qian, S.-C. Zhang, and J.-f. Jia, "Epitaxial growth of two-dimensional stanene," *Nature Materials* **14**, 1020 (2015).
- [198] C.-C. Liu, W. Feng, and Y. Yao, "Quantum Spin Hall Effect in Silicene and Two-Dimensional Germanium," *Physical Review Letters* **107**, 076802 (2011).
- [199] C.-C. Liu, H. Jiang, and Y. Yao, "Low-energy effective Hamiltonian involving spin-orbit coupling in silicene and two-dimensional germanium and tin," *Physical Review B* **84**, 195430 (2011).
- [200] P. Tang, P. Chen, W. Cao, H. Huang, S. Cahangirov, L. Xian, Y. Xu, S.-C. Zhang, W. Duan, and A. Rubio, "Stable two-dimensional dumbbell stanene: A quantum spin Hall insulator," *Physical Review B* **90**, 121408 (2014).
- [201] V. O. Özçelik and S. Ciraci, "Local Reconstructions of Silicene Induced by Adatoms," *The Journal of Physical Chemistry C* **117**, 26305 (2013).
- [202] V. O. Özçelik, E. Durgun, and S. Ciraci, "New Phases of Germanene," *The Journal of Physical Chemistry Letters* **5**, 2694 (2014).
- [203] X. Chen, L. Li, and M. Zhao, "Dumbbell stanene: a large-gap quantum spin hall insulator," *Physical Chemistry Chemical Physics* **17**, 16624 (2015).
- [204] X. Chen, L. Li, and M. Zhao, "Hydrogenation-induced large-gap quantum-spin-Hall insulator states in a germanium–tin dumbbell structure," *RSC Advances* **5**, 72462 (2015).
- [205] H. Zhang, J. Zhang, B. Zhao, T. Zhou, and Z. Yang, "Quantum anomalous Hall effect in stable dumbbell stanene," *Applied Physics Letters* **108**, 082104 (2016).
- [206] Y.-p. Wang, W.-x. Ji, C.-w. Zhang, P. Li, F. Li, P.-j. Wang, S.-s. Li, and S.-s. Yan, "Large-gap quantum spin Hall state in functionalized dumbbell stanene," *Applied Physics Letters* **108**, 073104 (2016).
- [207] T. Zhang, Z.-Y. Zeng, Y. Cheng, X.-R. Chen, and L.-C. Cai, "Dumbbell silicene: a strain-induced room temperature quantum spin Hall insulator," *New Journal of Physics* **18**, 043001 (2016).

- [208] L. S. Peak, "Notes on ultra-high-energy interaction processes," *Il Nuovo Cimento A* **12**, 533 (1972).
- [209] E. C. Franklin, "THE AMMONO CARBONIC ACIDS," *Journal of the American Chemical Society* **44**, 486 (1922).
- [210] S. Cao and J. Yu, "g-C₃N₄-based photocatalysts for hydrogen generation," *The journal of physical chemistry letters* **5**, 2101 (2014).
- [211] M. Wu, Q. Wang, Q. Sun, and P. Jena, "Functionalized Graphitic Carbon Nitride for Efficient Energy Storage," *The Journal of Physical Chemistry C* **117**, 6055 (2013).
- [212] Z. Zhao, Y. Sun, and F. Dong, "Graphitic carbon nitride based nanocomposites: a review," *Nanoscale* **7**, 15 (2015).
- [213] B. Xu, H. Xiang, Q. Wei, J. Q. Liu, Y. D. Xia, J. Yin, and Z. G. Liu, "Two-dimensional graphene-like C₂N: an experimentally available porous membrane for hydrogen purification," *Physical Chemistry Chemical Physics* **17**, 15115 (2015).
- [214] Y. Qu, F. Li, H. Zhou, and M. Zhao, "Highly Efficient Quantum Sieving in Porous Graphene-like Carbon Nitride for Light Isotopes Separation," *Scientific Reports* **6**, 19952 (2016).
- [215] Y. Yang, W. Li, H. Zhou, X. Zhang, and M. Zhao, "Tunable C₂N Membrane for High Efficient Water Desalination," *Scientific Reports* **6**, 29218 (2016).
- [216] A. Wang, X. Zhang, and M. Zhao, "Topological insulator states in a honeycomb lattice of s-triazines," *Nanoscale* **6**, 11157 (2014).
- [217] X. Zhang, A. Wang, and M. Zhao, "Spin-gapless semiconducting graphitic carbon nitrides: A theoretical design from first principles," *Carbon* **84**, 1 (2015).
- [218] X. Zhang and M. Zhao, "Prediction of quantum anomalous Hall effect on graphene nanomesh," *RSC Advances* **5**, 9875 (2015).
- [219] X. Zhang, M. Zhao, A. Wang, X. Wang, and A. Du, "Spin-polarization and ferromagnetism of graphitic carbon nitride materials," *Journal of Materials Chemistry C* **1**, 6265 (2013).
- [220] A. Du, S. Sanvito, and S. C. Smith, "First-Principles Prediction of Metal-Free Magnetism and Intrinsic Half-Metallicity in Graphitic Carbon Nitride," *Physical Review Letters* **108**, 197207 (2012).
- [221] T. Hom, W. Kiszewski, and B. Post, "Accurate lattice constants from multiple reflection measurements. II. Lattice constants of germanium silicon, and diamond," *Journal of Applied Crystallography* **8**, 457 (1975).

- [222] X. Zhao, L. Li, and M. Zhao, "Lattice match and lattice mismatch models of graphene on hexagonal boron nitride from first principles," *Journal of Physics: Condensed Matter* **26**, 095002 (2014).
- [223] S. Zhang, J. Zhou, Q. Wang, and P. Jena, "Beyond Graphitic Carbon Nitride: Nitrogen-Rich Penta-CN₂ Sheet," *The Journal of Physical Chemistry C* **120**, 3993 (2016).
- [224] B. Yang, H. Zhou, X. Zhang, and M. Zhao, "Electron spin-polarization and band gap engineering in carbon-modified graphitic carbon nitrides," *Journal of Materials Chemistry C* **3**, 10886 (2015).
- [225] C. Ataca, E. Aktürk, H. Şahin, and S. Ciraci, "Adsorption of carbon adatoms to graphene and its nanoribbons," *Journal of Applied Physics* **109**, 013704 (2011).
- [226] J. C. Meyer, C. O. Girit, M. F. Crommie, and A. Zettl, "Imaging and dynamics of light atoms and molecules on graphene," *Nature* **454**, 319 (2008).
- [227] U. Bangert, M. H. Gass, A. L. Bleloch, R. R. Nair, and J. Eccles, "Nanotopography of graphene," *physica status solidi (a)* **206**, 2115 (2009).
- [228] K. S. Novoselov, "Electric Field Effect in Atomically Thin Carbon Films," *Science* **306**, 666 (2004).
- [229] A. Du, S. Sanvito, Z. Li, D. Wang, Y. Jiao, T. Liao, Q. Sun, Y. H. Ng, Z. Zhu, R. Amal, *et al.*, "Hybrid graphene and graphitic carbon nitride nanocomposite: gap opening, electron-hole puddle, interfacial charge transfer, and enhanced visible light response," *Journal of the American Chemical Society* **134**, 4393 (2012).
- [230] A. Lopez-Bezanilla, "Strain-Mediated Modification of Phagraphene Dirac Cones," *The Journal of Physical Chemistry C* **120**, 17101 (2016).
- [231] L. Li, X. Zhang, X. Chen, and M. Zhao, "Giant Topological Nontrivial Band Gaps in Chloridized Gallium Bismuthide," *Nano Letters* **15**, 1296 (2015).
- [232] Y. Ma, L. Kou, X. Li, Y. Dai, and T. Heine, "Two-dimensional transition metal dichalcogenides with a hexagonal lattice: Room-temperature quantum spin Hall insulators," *Physical Review B* **93**, 035442 (2016).
- [233] J. B. Oostinga, H. B. Heersche, X. Liu, A. F. Morpurgo, and L. M. K. Vandersypen, "Gate-induced insulating state in bilayer graphene devices," *Nature Materials* **7**, 151 (2008).
- [234] L. Li and M. Zhao, "First-principles identifications of superstructures of germanene on Ag(111) surface and h-BN substrate," *Physical Chemistry Chemical Physics* **15**, 16853 (2013).
- [235] N. Marzari and D. Vanderbilt, "Maximally localized generalized Wannier functions for composite energy bands," *Physical Review B* **56**, 12847 (1997).

- [236] A. A. Mostofi, J. R. Yates, Y.-S. Lee, I. Souza, D. Vanderbilt, and N. Marzari, “wannier90: A tool for obtaining maximally-localised Wannier functions,” *Computer Physics Communications* **178**, 685 (2008).
- [237] G. Dong, K. Zhao, and L. Zhang, “Carbon self-doping induced high electronic conductivity and photoreactivity of g-C₃N₄,” *Chemical Communications* **48**, 6178 (2012).
- [238] A. Lourenço, N. Wellock, R. Thomas, M. Homer, H. Bouchard, T. Kanai, N. MacDougall, G. Royle, and H. Palmans, “Theoretical and experimental characterization of novel water-equivalent plastics in clinical high-energy carbon-ion beams,” *Physics in Medicine and Biology* **61**, 7623 (2016).
- [239] F. Ma, Y. Jiao, G. Gao, Y. Gu, A. Bilic, Z. Chen, and A. Du, “Graphene-like Two-Dimensional Ionic Boron with Double Dirac Cones at Ambient Condition,” *Nano Letters* **16**, 3022 (2016).
- [240] R. Balog, B. Jørgensen, L. Nilsson, M. Andersen, E. Rienks, M. Bianchi, M. Fanetti, E. Lægsgaard, A. Baraldi, S. Lizzit, Z. Sljivancanin, F. Besenbacher, B. Hammer, T. G. Pedersen, P. Hofmann, and L. Hornekær, “Bandgap opening in graphene induced by patterned hydrogen adsorption,” *Nature Materials* **9**, 315 (2010).
- [241] G. Gao, Y. Jiao, E. R. Waclawik, and A. Du, “Single Atom (Pd/Pt) Supported on Graphitic Carbon Nitride as an Efficient Photocatalyst for Visible-Light Reduction of Carbon Dioxide,” *Journal of the American Chemical Society* **138**, 6292 (2016).
- [242] G. G. Guzmán-Verri and L. C. Lew Yan Voon, “Electronic structure of silicon-based nanostructures,” *Physical Review B* **76**, 075131 (2007).
- [243] H. Jamgotchian, Y. Colignon, N. Hamzaoui, B. Ealet, J. Y. Hoarau, B. Aufray, and J. P. Bibérian, “Growth of silicene layers on Ag(111): unexpected effect of the substrate temperature,” *Journal of Physics: Condensed Matter* **24**, 172001 (2012).
- [244] B. Lalmi, H. Oughaddou, H. Enriquez, A. Kara, S. Vizzini, B. Ealet, and B. Aufray, “Epitaxial growth of a silicene sheet,” *Applied Physics Letters* **97**, 223109 (2010).
- [245] C.-L. Lin, R. Arafune, K. Kawahara, N. Tsukahara, E. Minamitani, Y. Kim, N. Takagi, and M. Kawai, “Structure of Silicene Grown on Ag(111),” *Applied Physics Express* **5**, 045802 (2012).
- [246] R. Arafune, C.-L. Lin, K. Kawahara, N. Tsukahara, E. Minamitani, Y. Kim, N. Takagi, and M. Kawai, “Structural transition of silicene on Ag(111),” *Surface Science* **608**, 297 (2013).
- [247] B. Feng, H. Li, C.-C. Liu, T.-N. Shao, P. Cheng, Y. Yao, S. Meng, L. Chen, and K. Wu, “Observation of Dirac Cone Warping and Chirality Effects in Silicene,” *ACS Nano* **7**, 9049 (2013).

- [248] A. Fleurence, R. Friedlein, T. Ozaki, H. Kawai, Y. Wang, and Y. Yamada-Takamura, "Experimental Evidence for Epitaxial Silicene on Diboride Thin Films," *Physical Review Letters* **108**, 245501 (2012).
- [249] M. E. Dávila, L. Xian, S. Cahangirov, A. Rubio, and G. Le Lay, "Germanene: a novel two-dimensional germanium allotrope akin to graphene and silicene," *New Journal of Physics* **16**, 095002 (2014).
- [250] E. Bianco, S. Butler, S. Jiang, O. D. Restrepo, W. Windl, and J. E. Goldberger, "Stability and Exfoliation of Germanane: A Germanium Graphane Analogue," *ACS Nano* **7**, 4414 (2013).
- [251] S. Jiang, S. Butler, E. Bianco, O. D. Restrepo, W. Windl, and J. E. Goldberger, "Improving the stability and optical properties of germanane via one-step covalent methyl-termination," *Nature Communications* **5**, 3389 (2014).
- [252] B. Radisavljevic, A. Radenovic, J. Brivio, V. Giacometti, and A. Kis, "Single-layer MoS₂ transistors," *Nature Nanotechnology* **6**, 147 (2011).
- [253] K. F. Mak, C. Lee, J. Hone, J. Shan, and T. F. Heinz, "Atomically Thin MoS₂: A New Direct-Gap Semiconductor," *Physical Review Letters* **105**, 136805 (2010).
- [254] Y. Zhang, Y. Zhang, Q. Ji, J. Ju, H. Yuan, J. Shi, T. Gao, D. Ma, M. Liu, Y. Chen, X. Song, H. Y. Hwang, Y. Cui, and Z. Liu, "Controlled Growth of High-Quality Monolayer WS₂ Layers on Sapphire and Imaging Its Grain Boundary," *ACS Nano* **7**, 8963 (2013).
- [255] H. Zhou, M. Zhao, X. Zhang, W. Dong, X. Wang, H. Bu, and A. Wang, "First-principles prediction of a new Dirac-fermion material: silicon germanide monolayer," *Journal of Physics: Condensed Matter* **25**, 395501 (2013).
- [256] J. Li, C. He, L. Meng, H. Xiao, C. Tang, X. Wei, J. Kim, N. Kioussis, G. Malcolm Stocks, and J. Zhong, "Two-dimensional topological insulators with tunable band gaps: Single-layer HgTe and HgSe," *Scientific Reports* **5**, 14115 (2015).
- [257] F.-C. Chuang, L.-Z. Yao, Z.-Q. Huang, Y.-T. Liu, C.-H. Hsu, T. Das, H. Lin, and A. Bansil, "Prediction of Large-Gap Two-Dimensional Topological Insulators Consisting of Bilayers of Group III Elements with Bi," *Nano Letters* **14**, 2505 (2014).
- [258] Z. F. Wang, N. Su, and F. Liu, "Prediction of a Two-Dimensional Organic Topological Insulator," *Nano Letters* **13**, 2842 (2013).
- [259] Z. Wang, Z. Liu, and F. Liu, "Organic topological insulators in organometallic lattices," *Nature Communications* **4**, 1471 (2013).
- [260] Z. F. Wang, Z. Liu, and F. Liu, "Quantum Anomalous Hall Effect in 2D Organic Topological Insulators," *Physical Review Letters* **110**, 196801 (2013).

- [261] Z. Liu, Z.-F. Wang, J.-W. Mei, Y.-S. Wu, and F. Liu, "Flat Chern Band in a Two-Dimensional Organometallic Framework," *Physical Review Letters* **110**, 106804 (2013).
- [262] X.-L. Qi and S.-C. Zhang, "Topological insulators and superconductors," *Reviews of Modern Physics* **83**, 1057 (2011).
- [263] M. Z. Hasan and C. L. Kane, "Colloquium : Topological insulators," *Reviews of Modern Physics* **82**, 3045 (2010).
- [264] B. A. Bernevig, T. L. Hughes, and S.-C. Zhang, "Quantum Spin Hall Effect and Topological Phase Transition in HgTe Quantum Wells," *Science* **314**, 1757 (2006).
- [265] I. Knez, R.-R. Du, and G. Sullivan, "Evidence for Helical Edge Modes in Inverted InAs/GaSb Quantum Wells," *Physical Review Letters* **107**, 136603 (2011).
- [266] A. Takayama, T. Sato, S. Souma, T. Oguchi, and T. Takahashi, "One-Dimensional Edge States with Giant Spin Splitting in a Bismuth Thin Film," *Physical Review Letters* **114**, 066402 (2015).
- [267] I. K. Drozdov, A. Alexandradinata, S. Jeon, S. Nadj-Perge, H. Ji, R. J. Cava, B. Andrei Bernevig, and A. Yazdani, "One-dimensional topological edge states of bismuth bilayers," *Nature Physics* **10**, 664 (2014).
- [268] C. L. Kane and E. J. Mele, "Quantum Spin Hall Effect in Graphene," *Physical Review Letters* **95**, 226801 (2005).
- [269] L. Kou, B. Yan, F. Hu, S.-c. Wu, T. O. Wehling, C. Felser, C. Chen, and T. Frauenheim, "Graphene-Based Topological Insulator with an Intrinsic Bulk Band Gap above Room Temperature," *Nano Letters* **13**, 6251 (2013).
- [270] L. Kou, S.-C. Wu, C. Felser, T. Frauenheim, C. Chen, and B. Yan, "Robust 2D Topological Insulators in van der Waals Heterostructures," *ACS Nano* **8**, 10448 (2014).
- [271] X. Chen, L. Li, and M. Zhao, "Hydrogenation-induced large-gap quantum-spin-Hall insulator states in a germanium–tin dumbbell structure," *RSC Advances* **5**, 72462 (2015).
- [272] S. M. Nie, Z. Song, H. Weng, and Z. Fang, "Quantum spin Hall effect in two-dimensional transition-metal dichalcogenide haeckelites," *Physical Review B* **91**, 235434 (2015).
- [273] W. Li, M. Guo, G. Zhang, and Y.-W. Zhang, "Gapless MoS₂ allotrope possessing both massless Dirac and heavy fermions," *Physical Review B* **89**, 205402 (2014).
- [274] Y. Ma, L. Kou, X. Li, Y. Dai, S. C. Smith, and T. Heine, "Quantum spin Hall effect and topological phase transition in two-dimensional square transition-metal dichalcogenides," *Physical Review B* **92**, 085427 (2015).

- [275] Y. Sun, C. Felser, and B. Yan, "Graphene-like Dirac states and quantum spin Hall insulators in square-octagonal MX_2 ($M = \text{Mo}, \text{W}; X = \text{S}, \text{Se}, \text{Te}$)," *Physical Review B* **92**, 165421 (2015).
- [276] P.-F. Liu, L. Zhou, T. Frauenheim, and L.-M. Wu, "New quantum spin Hall insulator in two-dimensional MoS_2 with periodically distributed pores," *Nanoscale* **8**, 4915 (2016).
- [277] X. Qian, J. Liu, L. Fu, and J. Li, "Quantum spin Hall effect in two-dimensional transition metal dichalcogenides," *Science* **346**, 1344 (2014).
- [278] X. Li, Y. Dai, Y. Ma, W. Wei, L. Yu, and B. Huang, "Prediction of large-gap quantum spin hall insulator and Rashba-Dresselhaus effect in two-dimensional g-TIA ($A = \text{N}, \text{P}, \text{As}, \text{and Sb}$) monolayer films," *Nano Research* **8**, 2954 (2015).
- [279] L. Zhou, L. Kou, Y. Sun, C. Felser, F. Hu, G. Shan, S. C. Smith, B. Yan, and T. Frauenheim, "New Family of Quantum Spin Hall Insulators in Two-dimensional Transition-Metal Halide with Large Nontrivial Band Gaps," *Nano Letters* **15**, 7867 (2015).
- [280] Z. Liu, C.-X. Liu, Y.-S. Wu, W.-H. Duan, F. Liu, and J. Wu, "Stable Nontrivial Z_2 Topology in Ultrathin Bi (111) Films: A First-Principles Study," *Physical Review Letters* **107**, 136805 (2011).
- [281] H. Weng, X. Dai, and Z. Fang, "Transition-Metal Pentatelluride ZrTe_5 and HfTe_5 : A paradigm for large-gap quantum spin Hall insulators," *Physical Review X* **4**, 011002 (2014).
- [282] L. Kou, Y. Ma, B. Yan, X. Tan, C. Chen, and S. C. Smith, "Encapsulated Silicene: A Robust Large-Gap Topological Insulator," *ACS Applied Materials & Interfaces* **7**, 19226 (2015).
- [283] Q. Liu, X. Zhang, L. B. Abdalla, A. Fazzio, and A. Zunger, "Switching a Normal Insulator into a Topological Insulator via Electric Field with Application to Phosphorene," *Nano Letters* **15**, 1222 (2015).
- [284] Z. Song, C.-C. Liu, J. Yang, J. Han, M. Ye, B. Fu, Y. Yang, Q. Niu, J. Lu, and Y. Yao, "Quantum spin Hall insulators and quantum valley Hall insulators of BiX/SbX ($X = \text{H}, \text{F}, \text{Cl}$ and Br) monolayers with a record bulk band gap," *NPG Asia Materials* **6**, e147 (2014).
- [285] C.-C. Liu, S. Guan, Z. Song, S. A. Yang, J. Yang, and Y. Yao, "Low-energy effective Hamiltonian for giant-gap quantum spin Hall insulators in honeycomb X -hydride/halide ($X = \text{N-Bi}$) monolayers," *Physical Review B* **90**, 085431 (2014).
- [286] Y. Xu, B. Yan, H.-J. Zhang, J. Wang, G. Xu, P. Tang, W. Duan, and S.-C. Zhang, "Large-Gap Quantum Spin Hall Insulators in Tin Films," *Physical Review Letters* **111**, 136804 (2013).

- [287] C. Si, J. Liu, Y. Xu, J. Wu, B.-L. Gu, and W. Duan, "Functionalized germanene as a prototype of large-gap two-dimensional topological insulators," *Physical Review B* **89**, 115429 (2014).
- [288] J.-J. Zhou, W. Feng, C.-C. Liu, S. Guan, and Y. Yao, "Large-Gap Quantum Spin Hall Insulator in Single Layer Bismuth Monobromide Bi_4Br_4 ," *Nano Letters* **14**, 4767 (2014).
- [289] W. Luo and H. Xiang, "Room Temperature Quantum Spin Hall Insulators with a Buckled Square Lattice," *Nano Letters* **15**, 3230 (2015).
- [290] Y. Ma, Y. Dai, L. Kou, T. Frauenheim, and T. Heine, "Robust Two-Dimensional Topological Insulators in Methyl-Functionalized Bismuth, Antimony, and Lead Bilayer Films," *Nano Letters* **15**, 1083 (2015).
- [291] Y.-p. Wang, W.-x. Ji, C.-w. Zhang, P. Li, F. Li, M.-j. Ren, X.-L. Chen, M. Yuan, and P.-j. Wang, "Controllable band structure and topological phase transition in two-dimensional hydrogenated arsenene," *Scientific Reports* **6**, 20342 (2016).
- [292] H. Zhao, C.-w. Zhang, W.-x. Ji, R.-w. Zhang, S.-s. Li, S.-s. Yan, B.-m. Zhang, P. Li, and P.-j. Wang, "Unexpected Giant-Gap Quantum Spin Hall Insulator in Chemically Decorated Plumbene Monolayer," *Scientific Reports* **6**, 20152 (2016).
- [293] R.-w. Zhang, C.-w. Zhang, W.-x. Ji, S.-s. Li, S.-s. Yan, S.-j. Hu, P. Li, P.-j. Wang, and F. Li, "Room Temperature Quantum Spin Hall Insulator in Ethynyl-Derivative Functionalized Stanene Films," *Scientific Reports* **6**, 18879 (2016).
- [294] W.-x. Ji, C.-w. Zhang, M. Ding, P. Li, F. Li, M.-j. Ren, P.-j. Wang, S.-j. Hu, and S.-s. Yan, "Stanene cyanide: a novel candidate of Quantum Spin Hall insulator at high temperature," *Scientific Reports* **5**, 18604 (2016).
- [295] Y. Ma, Y. Dai, W. Wei, B. Huang, and M.-H. Whangbo, "Strain-induced quantum spin Hall effect in methyl-substituted germanene GeCH_3 ," *Scientific Reports* **4**, 7297 (2015).
- [296] C. P. Crisostomo, L.-Z. Yao, Z.-Q. Huang, C.-H. Hsu, F.-C. Chuang, H. Lin, M. A. Albao, and A. Bansil, "Robust Large Gap Two-Dimensional Topological Insulators in Hydrogenated III-V Buckled Honeycombs," *Nano Letters* **15**, 6568 (2015).
- [297] R. R. Q. Freitas, R. Rivelino, F. de Brito Mota, C. M. C. de Castilho, A. Kakanakova-Georgieva, and G. K. Gueorguiev, "Topological Insulating Phases in Two-Dimensional Bismuth-Containing Single Layers Preserved by Hydrogenation," *The Journal of Physical Chemistry C* **119**, 23599 (2015).
- [298] Y. Ma, X. Li, L. Kou, B. Yan, C. Niu, Y. Dai, and T. Heine, "Two-dimensional inversion-asymmetric topological insulators in functionalized III-Bi bilayers," *Physical Review B* **91**, 235306 (2015).

- [299] R. R. Q. Freitas, F. de Brito Mota, R. Rivelino, C. M. C. de Castilho, A. Kakanakova-Georgieva, and G. K. Gueorguiev, "Tuning band inversion symmetry of buckled III-Bi sheets by halogenation," *Nanotechnology* **27**, 055704 (2016).
- [300] S.-s. Li, W.-x. Ji, C.-w. Zhang, S.-j. Hu, P. Li, P.-j. Wang, B.-m. Zhang, and C.-l. Cao, "Robust Room-Temperature Quantum Spin Hall Effect in Methyl-functionalized InBi honeycomb film," *Scientific Reports* **6**, 23242 (2016).
- [301] R.-w. Zhang, C.-w. Zhang, W.-x. Ji, S.-s. Li, S.-s. Yan, P. Li, and P.-j. Wang, "Functionalized Thallium Antimony Films as Excellent Candidates for Large-Gap Quantum Spin Hall Insulator," *Scientific Reports* **6**, 21351 (2016).
- [302] M. Zhao, X. Chen, L. Li, and X. Zhang, "Driving a GaAs film to a large-gap topological insulator by tensile strain," *Scientific Reports* **5**, 8441 (2015).
- [303] K. Parlinski, Z. Q. Li, and Y. Kawazoe, "First-Principles Determination of the Soft Mode in Cubic ZrO_2 ," *Physical Review Letters* **78**, 4063 (1997).
- [304] L. Fu and C. L. Kane, "Time reversal polarization and a Z_2 adiabatic spin pump," *Physical Review B* **74**, 195312 (2006).
- [305] M. Henini, J. Ibáñez, M. Schmidbauer, M. Shafi, S. V. Novikov, L. Turyanska, S. I. Molina, D. L. Sales, M. F. Chisholm, and J. Misiewicz, "Molecular beam epitaxy of GaBiAs on (311)B GaAs substrates," *Applied Physics Letters* **91**, 251909 (2007).
- [306] S. Francoeur, M.-J. Seong, A. Mascarenhas, S. Tixier, M. Adamczyk, and T. Tiedje, "Band gap of $GaAs_{1-x}Bi_x$, $0 < x < 3.6\%$," *Applied Physics Letters* **82**, 3874 (2003).
- [307] N. Denisov, A. Alekseev, O. Utas, S. Azatyan, A. Zotov, and A. Saranin, "Bismuth-Indium-Sodium two-dimensional compounds on Si(111) surface," *Surface Science* **666**, 64 (2017).
- [308] D. V. Gruznev, L. V. Bondarenko, A. V. Matetskiy, A. N. Mihalyuk, A. Y. Tupchaya, O. A. Utas, S. V. Ereemeev, C.-R. Hsing, J.-P. Chou, C.-M. Wei, A. V. Zotov, and A. A. Saranin, "Synthesis of two-dimensional Tl_xBi_{1-x} compounds and Archimedean encoding of their atomic structure," *Scientific Reports* **6**, 19446 (2016).
- [309] F. Ma, M. Zhou, Y. Jiao, G. Gao, Y. Gu, A. Bilic, Z. Chen, and A. Du, "Single Layer Bismuth Iodide: Computational Exploration of Structural, Electrical, Mechanical and Optical Properties," *Scientific Reports* **5**, 17558 (2015).
- [310] J. Trotter and T. Zobel, "The crystal structure of SbI_3 and BiI_3 ," *Zeitschrift für Kristallographie-Crystalline Materials* **123**, 67 (1966).

- [311] Y. Morino, T. Ukaji, and T. Ito, "Molecular structure determination by gas electron diffraction at high temperatures. II. Arsenic triiodide and gallium triiodide," *Bulletin of the Chemical Society of Japan* **39**, 71 (1966).
- [312] M. C. Drake and G. M. Rosenblatt, "Raman spectroscopy of gaseous GaCl₃ and GaI₃," *The Journal of Chemical Physics* **65**, 4067 (1976).
- [313] M.-L. Saboungi, M. Howe, and D. Price, "Structure and dynamics of molten aluminium and gallium trihalides," *Molecular Physics* **79**, 847 (1993).
- [314] L. Zhou, W. Shi, Y. Sun, B. Shao, C. Felser, B. Yan, and T. Frauenheim, "Two-dimensional rectangular tantalum carbide halides TaCX (X = Cl, Br, I): novel large-gap quantum spin Hall insulators," *2D Materials* **3**, 035018 (2016).
- [315] S. Giglberger, L. E. Golub, V. V. Bel'kov, S. N. Danilov, D. Schuh, C. Gerl, F. Rohlfiing, J. Stahl, W. Wegscheider, D. Weiss, W. Prettl, and S. D. Ganichev, "Rashba and Dresselhaus spin splittings in semiconductor quantum wells measured by spin photocurrents," *Physical Review B* **75**, 035327 (2007).
- [316] Y. A. Bychkov and É. I. Rashba, "Properties of a 2d electron gas with lifted spectral degeneracy," *JETP lett* **39**, 78 (1984).
- [317] G. Lommer, F. Malcher, and U. Rössler, "Reduced g factor of subband Landau levels in AlGaAs/GaAs heterostructures," *Physical Review B* **32**, 6965 (1985).
- [318] I. Žutić, J. Fabian, and S. Das Sarma, "Spintronics: Fundamentals and applications," *Reviews of Modern Physics* **76**, 323 (2004).
- [319] W. Ming, Z. F. Wang, M. Zhou, M. Yoon, and F. Liu, "Formation of Ideal Rashba States on Layered Semiconductor Surfaces Steered by Strain Engineering," *Nano Letters* **16**, 404 (2016).
- [320] L. Kou, X. Tan, Y. Ma, H. Tahini, L. Zhou, Z. Sun, D. Aijun, C. Chen, and S. C. Smith, "Tetragonal bismuth bilayer: a stable and robust quantum spin hall insulator," *2D Materials* **2**, 045010 (2015).
- [321] B. Huang, K.-H. Jin, H. L. Zhuang, L. Zhang, and F. Liu, "Interface orbital engineering of large-gap topological states: Decorating gold on a Si(111) surface," *Physical Review B* **93**, 115117 (2016).
- [322] M. Wang, L. Liu, C.-C. Liu, and Y. Yao, "van der Waals heterostructures of germanene, stanene, and silicene with hexagonal boron nitride and their topological domain walls," *Physical Review B* **93**, 155412 (2016).
- [323] S. J. Kim, K. Choi, B. Lee, Y. Kim, and B. H. Hong, "Materials for Flexible, Stretchable Electronics: Graphene and 2D Materials," *Annual Review of Materials Research* **45**, 63 (2015).

- [324] P. Vogt, P. De Padova, C. Quaresima, J. Avila, E. Frantzeskakis, M. C. Asensio, A. Resta, B. Ealet, and G. Le Lay, "Silicene: Compelling Experimental Evidence for Graphenelike Two-Dimensional Silicon," *Physical Review Letters* **108**, 155501 (2012).
- [325] D. Chiappe, C. Grazianetti, G. Tallarida, M. Fanciulli, and A. Molle, "Local Electronic Properties of Corrugated Silicene Phases," *Advanced Materials* **24**, 5088 (2012).
- [326] E. Bianco, S. Butler, S. Jiang, O. D. Restrepo, W. Windl, and J. E. Goldberger, "Stability and Exfoliation of Germanane: A Germanium Graphane Analogue," *ACS Nano* **7**, 4414 (2013).
- [327] M. Derivaz, D. Dentel, R. Stephan, M.-C. Hanf, A. Mehdaoui, P. Sonnet, and C. Pirri, "Continuous Germanene Layer on Al(111)," (2015).
- [328] F.-f. Zhu, W.-j. Chen, Y. Xu, C.-l. Gao, D.-d. Guan, C.-h. Liu, D. Qian, S.-C. Zhang, and J.-f. Jia, "Epitaxial growth of two-dimensional stanene," *Nature materials* **14**, 1020 (2015).
- [329] S. Zhang, M. Xie, F. Li, Z. Yan, Y. Li, E. Kan, W. Liu, Z. Chen, and H. Zeng, "Semiconducting Group 15 Monolayers: A Broad Range of Band Gaps and High Carrier Mobilities," *Angewandte Chemie International Edition* **55**, 1666 (2016).
- [330] X. Li, H. Liu, H. Jiang, F. Wang, and J. Feng, "Edge engineering of a topological Bi(111) bilayer," *Physical Review B* **90**, 165412 (2014).
- [331] Z. Liu, C.-X. Liu, Y.-S. Wu, W.-H. Duan, F. Liu, and J. Wu, "Stable Nontrivial Z_2 Topology in Ultrathin Bi (111) Films: A First-Principles Study," *Physical Review Letters* **107**, 136805 (2011).
- [332] F. Yang, L. Miao, Z. F. Wang, M.-Y. Yao, F. Zhu, Y. R. Song, M.-X. Wang, J.-P. Xu, A. V. Fedorov, Z. Sun, G. B. Zhang, C. Liu, F. Liu, D. Qian, C. L. Gao, and J.-F. Jia, "Spatial and Energy Distribution of Topological Edge States in Single Bi(111) Bilayer," *Physical Review Letters* **109**, 016801 (2012).
- [333] T. Hirahara, G. Bihlmayer, Y. Sakamoto, M. Yamada, H. Miyazaki, S.-i. Kimura, S. Blügel, and S. Hasegawa, "Interfacing 2D and 3D Topological Insulators: Bi(111) Bilayer on Bi₂Se₃," *Physical Review Letters* **107**, 166801 (2011).
- [334] T. Hirahara, N. Fukui, T. Shirasawa, M. Yamada, M. Aitani, H. Miyazaki, M. Matsumami, S. Kimura, T. Takahashi, S. Hasegawa, and K. Kobayashi, "Atomic and Electronic Structure of Ultrathin Bi(111) Films Grown on Bi₂Te₃(111) substrates: Evidence for a Strain-Induced Topological Phase Transition," *Physical Review Letters* **109**, 227401 (2012).
- [335] J. L. Zhang, S. Zhao, C. Han, Z. Wang, S. Zhong, S. Sun, R. Guo, X. Zhou, C. D. Gu, K. D. Yuan, Z. Li, and W. Chen, "Epitaxial Growth of Single Layer Blue

- Phosphorus: A New Phase of Two-Dimensional Phosphorus,” *Nano Letters* **16**, 4903 (2016).
- [336] Y. Liu, G. Wang, Q. Huang, L. Guo, and X. Chen, “Structural and Electronic Properties of *T* Graphene: A Two-Dimensional Carbon Allotrope with Tetrarings,” *Physical Review Letters* **108**, 225505 (2012).
- [337] B. G. Kim and H. J. Choi, “Graphyne: Hexagonal network of carbon with versatile Dirac cones,” *Physical Review B* **86**, 115435 (2012).
- [338] L. Kou, X. Tan, Y. Ma, H. Tahini, L. Zhou, Z. Sun, D. Aijun, C. Chen, and S. C. Smith, “Tetragonal bismuth bilayer: a stable and robust quantum spin hall insulator,” *2D Materials* **2**, 045010 (2015).
- [339] P. Li and W. Luo, “A new structure of two-dimensional allotropes of group V elements,” *Scientific Reports* **6**, 25423 (2016).
- [340] X.-L. Qi and S.-C. Zhang, “Topological insulators and superconductors,” *Reviews of Modern Physics* **83**, 1057 (2011).
- [341] C. L. Kane and E. J. Mele, “Quantum Spin Hall Effect in Graphene,” *Physical Review Letters* **95**, 226801 (2005).
- [342] Y. Yao, F. Ye, X.-L. Qi, S.-C. Zhang, and Z. Fang, “Spin-orbit gap of graphene: First-principles calculations,” *Physical Review B* **75**, 041401 (2007).
- [343] B. A. Bernevig, T. L. Hughes, and S.-C. Zhang, “Quantum spin Hall effect and topological phase transition in HgTe quantum wells,” *Science* **314**, 1757 (2006).
- [344] I. Knez, R.-R. Du, and G. Sullivan, “Evidence for Helical Edge Modes in Inverted InAs/GaSb Quantum Wells,” *Physical Review Letters* **107**, 136603 (2011).
- [345] M. Konig, S. Wiedmann, C. Brune, A. Roth, H. Buhmann, L. W. Molenkamp, X.-L. Qi, and S.-C. Zhang, “Quantum Spin Hall Insulator State in HgTe Quantum Wells,” *Science* **318**, 766 (2007).
- [346] X. Chen, L. Li, and M. Zhao, “Dumbbell stanane: a large-gap quantum spin hall insulator,” *Physical Chemistry Chemical Physics* **17**, 16624 (2015).
- [347] M. Zhao, X. Zhang, and L. Li, “Strain-driven band inversion and topological aspects in Antimonene,” *Scientific Reports* **5**, 16108 (2015).
- [348] A. A. Mostofi, J. R. Yates, G. Pizzi, Y.-S. Lee, I. Souza, D. Vanderbilt, and N. Marzari, “An updated version of wannier90: A tool for obtaining maximally-localised Wannier functions,” *Computer Physics Communications* **185**, 2309 (2014).
- [349] M. Sancho and J. Sancho, “Highly convergent schemes for the calculation of bulk and surface Green functions,” *Journal of Physics F: Metal Physics* **851** (2000).

- [350] Q. Wu, S. Zhang, H.-F. Song, M. Troyer, and A. A. Soluyanov, “WannierTools: An open-source software package for novel topological materials,” *Computer Physics Communications* **224**, 405 (2018).
- [351] E. Aktürk, O. Ü. Aktürk, and S. Ciraci, “Single and bilayer bismuthene: Stability at high temperature and mechanical and electronic properties,” *Physical Review B* **94**, 014115 (2016).
- [352] L. Li, O. Leenaerts, X. Kong, X. Chen, M. Zhao, and F. M. Peeters, “Gallium bismuth halide GaBi-X₂ (X = I, Br, Cl) monolayers with distorted hexagonal framework: Novel room-temperature quantum spin Hall insulators,” *Nano Research* **10**, 2168 (2017).
- [353] L. Chen, Z. F. Wang, and F. Liu, “Robustness of two-dimensional topological insulator states in bilayer bismuth against strain and electrical field,” *Physical Review B* **87**, 235420 (2013).
- [354] K. V. Klitzing, G. Dorda, and M. Pepper, “New Method for High-Accuracy Determination of the Fine-Structure Constant Based on Quantized Hall Resistance,” *Physical Review Letters* **45**, 494 (1980).
- [355] D. J. Thouless, M. Kohmoto, M. P. Nightingale, and M. den Nijs, “Quantized Hall Conductance in a Two-Dimensional Periodic Potential,” *Physical Review Letters* **49**, 405 (1982).
- [356] X.-L. Qi, Y.-S. Wu, and S.-C. Zhang, “Topological quantization of the spin Hall effect in two-dimensional paramagnetic semiconductors,” *Physical Review B* **74**, 085308 (2006).
- [357] H. Weng, R. Yu, X. Hu, X. Dai, and Z. Fang, “Quantum anomalous Hall effect and related topological electronic states,” *Advances in Physics* **64**, 227 (2015).
- [358] J. Zhang, B. Zhao, T. Zhou, and Z. Yang, “Quantum anomalous Hall effect in real materials,” *Chinese Physics B* **25**, 117308 (2016).
- [359] C.-X. Liu, X.-L. Qi, X. Dai, Z. Fang, and S.-C. Zhang, “Quantum Anomalous Hall Effect in Hg_{1-y}Mn_yTe Quantum Wells,” *Physical Review Letters* **101**, 146802 (2008).
- [360] H. Zhang, C. Lazo, S. Blügel, S. Heinze, and Y. Mokrousov, “Electrically Tunable Quantum Anomalous Hall Effect in Graphene Decorated by 5d Transition-Metal Adatoms,” *Physical Review Letters* **108**, 056802 (2012).
- [361] C. M. Acosta, M. P. Lima, R. H. Miwa, A. J. R. da Silva, and A. Fazzio, “Topological phases in triangular lattices of Ru adsorbed on graphene: Ab initio calculations,” *Physical Review B* **89**, 155438 (2014).

- [362] J. Hu, Z. Zhu, and R. Wu, "Chern Half Metals: A New Class of Topological Materials to Realize the Quantum Anomalous Hall Effect," *Nano Letters* **15**, 2074 (2015).
- [363] M. Ezawa, "Valley-Polarized Metals and Quantum Anomalous Hall Effect in Silicene," *Physical Review Letters* **109**, 055502 (2012).
- [364] H. Zhang, F. Freimuth, G. Bihlmayer, S. Blügel, and Y. Mokrousov, "Topological phases of Bi(111) bilayer in an external exchange field," *Physical Review B* **86**, 035104 (2012).
- [365] H. Zhang, F. Freimuth, G. Bihlmayer, M. Ležaić, S. Blügel, and Y. Mokrousov, "Engineering quantum anomalous Hall phases with orbital and spin degrees of freedom," *Physical Review B* **87**, 205132 (2013).
- [366] S.-M. Huang, S.-T. Lee, and C.-Y. Mou, "Ferromagnetism and quantum anomalous Hall effect in one-side-saturated buckled honeycomb lattices," *Physical Review B* **89**, 195444 (2014).
- [367] S.-C. Wu, G. Shan, and B. Yan, "Prediction of Near-Room-Temperature Quantum Anomalous Hall Effect on Honeycomb Materials," *Physical Review Letters* **113**, 256401 (2014).
- [368] K. F. Garrity and D. Vanderbilt, "Chern Insulators from Heavy Atoms on Magnetic Substrates," *Physical Review Letters* **110**, 116802 (2013).
- [369] T. Cai, X. Li, F. Wang, S. Ju, J. Feng, and C.-D. Gong, "Single-Spin Dirac Fermion and Chern Insulator Based on Simple Oxides," *Nano Letters* **15**, 6434 (2015).
- [370] M. Zhou, Z. Liu, W. Ming, Z. Wang, and F. Liu, " sd^2 Graphene: Kagome Band in a Hexagonal Lattice," *Physical Review Letters* **113**, 236802 (2014).
- [371] C. Wu, "Orbital Analogue of the Quantum Anomalous Hall Effect in p -Band Systems," *Physical Review Letters* **101**, 186807 (2008).
- [372] X.-J. Liu, X. Liu, C. Wu, and J. Sinova, "Quantum anomalous Hall effect with cold atoms trapped in a square lattice," *Physical Review A* **81**, 033622 (2010).
- [373] R. Yu, W. Zhang, H.-J. Zhang, S.-C. Zhang, X. Dai, and Z. Fang, "Quantized anomalous Hall effect in magnetic topological insulators," *Science* **329**, 61 (2010).
- [374] C.-Z. Chang, J. Zhang, X. Feng, J. Shen, Z. Zhang, M. Guo, K. Li, Y. Ou, P. Wei, L.-L. Wang, Z.-Q. Ji, Y. Feng, S. Ji, X. Chen, J. Jia, X. Dai, Z. Fang, S.-C. Zhang, K. He, Y. Wang, L. Lu, X.-C. Ma, and Q.-K. Xue, "Experimental Observation of the Quantum Anomalous Hall Effect in a Magnetic Topological Insulator," *Science* **340**, 167 (2013).

- [375] G. Jotzu, M. Messer, R. Desbuquois, M. Lebrat, T. Uehlinger, D. Greif, and T. Esslinger, "Experimental realization of the topological Haldane model with ultracold fermions," *Nature* **515**, 237 (2014).
- [376] Z. Wu, L. Zhang, W. Sun, X.-T. Xu, B.-Z. Wang, S.-C. Ji, Y. Deng, S. Chen, X.-J. Liu, and J.-W. Pan, "Realization of two-dimensional spin-orbit coupling for Bose-Einstein condensates," *Science* **354**, 83 (2016).
- [377] J. Wu, J. Liu, and X.-J. Liu, "Topological Spin Texture in a Quantum Anomalous Hall Insulator," *Physical Review Letters* **113**, 136403 (2014).
- [378] X.-L. Qi, T. L. Hughes, and S.-C. Zhang, "Chiral topological superconductor from the quantum Hall state," *Physical Review B* **82**, 184516 (2010).
- [379] X.-J. Liu, K. T. Law, and T. K. Ng, "Realization of 2D Spin-Orbit Interaction and Exotic Topological Orders in Cold Atoms," *Physical Review Letters* **112**, 086401 (2014).
- [380] Q. L. He, L. Pan, A. L. Stern, E. C. Burks, X. Che, G. Yin, J. Wang, B. Lian, Q. Zhou, E. S. Choi, K. Murata, X. Kou, Z. Chen, T. Nie, Q. Shao, Y. Fan, S.-C. Zhang, K. Liu, J. Xia, and K. L. Wang, "Chiral Majorana fermion modes in a quantum anomalous Hall insulator–superconductor structure," *Science* **357**, 294 (2017).
- [381] A. D. McNaught and A. D. McNaught, *Compendium of chemical terminology*, Vol. 1669 (Blackwell Science Oxford, 1997).
- [382] M. Chhowalla, Z. Liu, and H. Zhang, "Two-dimensional transition metal dichalcogenide (TMD) nanosheets," *Chemical Society Reviews* **44**, 2584 (2015).
- [383] G.-B. Liu, D. Xiao, Y. Yao, X. Xu, and W. Yao, "Electronic structures and theoretical modelling of two-dimensional group-VIB transition metal dichalcogenides," *Chemical Society Reviews* **44**, 2643 (2015).
- [384] H. Marvi, C. Gong, N. Gravish, H. Astley, M. Travers, R. L. Hatton, J. R. Mendelson, H. Choset, D. L. Hu, and D. I. Goldman, "Sidewinding with minimal slip: Snake and robot ascent of sandy slopes," *Science* **346**, 224 (2014).
- [385] Y. Wang, L. Li, W. Yao, S. Song, J. T. Sun, J. Pan, X. Ren, C. Li, E. Okunishi, Y.-Q. Wang, E. Wang, Y. Shao, Y. Y. Zhang, H.-t. Yang, E. F. Schwier, H. Iwasawa, K. Shimada, M. Taniguchi, Z. Cheng, S. Zhou, S. Du, S. J. Pennycook, S. T. Pantelides, and H.-J. Gao, "Monolayer PtSe₂, a New Semiconducting Transition-Metal-Dichalcogenide, Epitaxially Grown by Direct Selenization of Pt," *Nano Letters* **15**, 4013 (2015).
- [386] Y. Ma, Y. Dai, M. Guo, C. Niu, Y. Zhu, and B. Huang, "Evidence of the Existence of Magnetism in Pristine VX₂ Monolayers (X = S, Se) and Their Strain-Induced Tunable Magnetic Properties," *ACS Nano* **6**, 1695 (2012).

- [387] F. Zheng, C. Cai, S. Ge, X. Zhang, X. Liu, H. Lu, Y. Zhang, J. Qiu, T. Taniguchi, K. Watanabe, S. Jia, J. Qi, J.-H. Chen, D. Sun, and J. Feng, "On the Quantum Spin Hall Gap of Monolayer 1T-WTe₂," *Advanced Materials* **28**, 4845 (2016).
- [388] S. Wang, H. Ge, S. Sun, J. Zhang, F. Liu, X. Wen, X. Yu, L. Wang, Y. Zhang, H. Xu, J. C. Neufeind, Z. Qin, C. Chen, C. Jin, Y. Li, D. He, and Y. Zhao, "A New Molybdenum Nitride Catalyst with Rhombohedral MoS₂ Structure for Hydrogenation Applications," *Journal of the American Chemical Society* **137**, 4815 (2015).
- [389] F. Wu, C. Huang, H. Wu, C. Lee, K. Deng, E. Kan, and P. Jena, "Atomically Thin Transition-Metal Dinitrides: High-Temperature Ferromagnetism and Half-Metallicity," *Nano Letters* **15**, 8277 (2015).
- [390] H. Wu, Y. Qian, R. Lu, and W. Tan, "A theoretical study on the electronic property of a new two-dimensional material molybdenum dinitride," *Physics Letters A* **380**, 768 (2016).
- [391] Y. Wang and Y. Ding, "The hydrogen-induced structural stability and promising electronic properties of molybdenum and tungsten dinitride nanosheets: a first-principles study," *Journal of Materials Chemistry C* **4**, 7485 (2016).
- [392] Z. Liu, J. Liu, and J. Zhao, "YN₂ monolayer: Novel p-state Dirac half metal for high-speed spintronics," *Nano Research* **10**, 1972 (2017).
- [393] X. L. Wang, "Proposal for a New Class of Materials: Spin Gapless Semiconductors," *Physical Review Letters* **100**, 156404 (2008).
- [394] X.-L. Wang, "Dirac spin-gapless semiconductors: promising platforms for massless and dissipationless spintronics and new (quantum) anomalous spin Hall effects," *National Science Review* **4**, 252 (2017).
- [395] M. Sancho and J. Sancho, "Highly convergent schemes for the calculation of bulk and surface Green functions," *Journal of Physics F: Metal Physics* **851** (2000).
- [396] M. S. Dresselhaus, G. Dresselhaus, and A. Jorio, *Group theory: application to the physics of condensed matter* (Springer Science & Business Media, 2007).
- [397] R. Winkler, *Spin-orbit coupling effects in two-dimensional electron and hole systems*, Vol. 191 (Springer Science & Business Media, 2003).
- [398] L. Zhou, W. Shi, Y. Sun, B. Shao, C. Felser, B. Yan, and T. Frauenheim, "Two-dimensional rectangular tantalum carbide halides TaCX (X = Cl, Br, I): novel large-gap quantum spin Hall insulators," *2D Materials* **3**, 035018 (2016).
- [399] L. Li, O. Leenaerts, X. Kong, X. Chen, M. Zhao, and F. M. Peeters, "Gallium bismuth halide GaBi-X₂ (X = I, Br, Cl) monolayers with distorted hexagonal framework: Novel room-temperature quantum spin Hall insulators," *Nano Research* **10**, 2168 (2017).

- [400] P. Hu, Z. Wen, L. Wang, P. Tan, and K. Xiao, "Synthesis of Few-Layer GaSe Nanosheets for High Performance Photodetectors," *ACS Nano* **6**, 5988 (2012).
- [401] L. Li and M. Zhao, "First-principles identifications of superstructures of germanene on Ag(111) surface and h-BN substrate," *Physical Chemistry Chemical Physics* **15**, 16853 (2013).
- [402] S. Wu, V. Fatemi, Quinn, D. Gibson, K. Watanabe, T. Taniguchi, R. J. Cava, and P. Jarillo-Herrero, "Observation of the quantum spin Hall effect up to 100 kelvin in a monolayer crystal Downloaded from," *Science* **359**, 76 (2018).
- [403] Y. Ren, Z. Qiao, and Q. Niu, "Topological phases in two-dimensional materials: a review," *Reports on Progress in Physics* **79**, 066501 (2016).
- [404] C. Niu, G. Bihlmayer, H. Zhang, D. Wortmann, S. Blügel, and Y. Mokrousov, "Functionalized bismuth films: Giant gap quantum spin Hall and valley-polarized quantum anomalous Hall states," *Physical Review B* **91**, 041303 (2015).
- [405] C.-C. Liu, J.-J. Zhou, and Y. Yao, "Valley-polarized quantum anomalous Hall phases and tunable topological phase transitions in half-hydrogenated Bi honeycomb monolayers," *Physical Review B* **91**, 165430 (2015).
- [406] X.-L. Sheng and B. K. Nikolić, "Monolayer of the 5*d* transition metal trichloride OsCl₃: A playground for two-dimensional magnetism, room-temperature quantum anomalous Hall effect, and topological phase transitions," *Physical Review B* **95**, 201402 (2017).

Appendix A

Curriculum Vitae

Curriculum Vitae

Personal Information

Name: Linyang Li

Gender: Male

Date of birth: 07/1988

Nationality: Chinese

E-mail: linyang.li@uantwerpen.be

Address: Campus Groenenborger, Groenenborgerlaan 171,
Antwerp, Belgium



Education Background

- PhD (09/2015-06/2019), University of Antwerp, Belgium
Condensed Matter Theory (CMT), Department of Physics
Supervisor: Prof. Dr. François M. Peeters
- MS (09/2012-06/2015), Shandong University, China
Master of Science
Condensed Matter Physics, School of Physics
Supervisor: Prof. Dr. Mingwen Zhao
- BS (09/2008-06/2012), Shandong University, China
Bachelor of Science
Physics, School of Physics

Publications (PhD, UA, 09/2015-06/2019)

1. **L. Li**, O. Leenaerts, X. Kong, X. Chen, M. Zhao, and F. M. Peeters, "Gallium bismuth halide GaBi-X₂ (X = I, Br, Cl) monolayers with distorted hexagonal framework: Novel room-temperature quantum spin Hall insulators," *Nano Research* **10**, 2168 (2017). (IF = 7.994)
2. X. Kong, **L. Li**, O. Leenaerts, W. Wang, X.-J. Liu, and F. M. Peeters, "Quantum anomalous Hall effect in stable 1T-YN₂ monolayer with a large nontrivial band gap and high Chern number," *Nanoscale* **10**, 8153 (2018). (IF = 7.233)
3. **L. Li**, X. Kong, O. Leenaerts, X. Chen, B. Sanyal, and F. M. Peeters, "Carbon-rich carbon nitride monolayers with Dirac cones: Dumbbell C₄N," *Carbon* **118**, 285 (2017). (IF = 7.082)
4. **L. Li**, X. Kong, and F. M. Peeters, "New nanoporous graphyne monolayer as

- nodal line semimetal: Double Dirac points with an ultrahigh Fermi velocity,” *Carbon* **141**, 712 (2019). (IF = 7.082)
5. X. Kong, **L. Li**, O. Leenaerts, X.-J. Liu, and F. M. Peeters, “Group-V elemental bilayers: A tunable structure model with four-, six-, and eight-atom rings,” *Physical Review B* **96**, 035123 (2017). (IF = 3.813)
 6. X. Kong, **L. Li**, and F. M. Peeters, “Topological Dirac semimetal phase in Ge_xSn_y alloys,” *Applied Physics Letters* **112**, 251601 (2018). (IF = 3.495)
 7. X. Kong, **L. Li**, and F. M. Peeters, “Graphene-based heterostructures with moiré superlattice that preserve the Dirac cone: a first-principles study,” *Journal of Physics: Condensed Matter* **31**, 255302 (2019). (IF = 2.617)
 8. W. Wang, **L. Li**, X. Kong, B. V. Duppen, and F. M. Peeters, “ $\text{T}_{4,4,4}$ -graphyne: A 2D carbon allotrope with an intrinsic direct bandgap,” *Solid State Communications* **293**, 23 (2019). (IF = 1.549)

Publications (MS, SDU, 09/2012-06/2015)

1. **L. Li**, X. Zhang, X. Chen, and M. Zhao, “Giant topological nontrivial band gaps in chloridized gallium bismuthide,” *Nano Letters* **15**, 1296 (2015). (IF = 12.080)
2. **L. Li**, and M. Zhao, “Structures, energetics, and electronic properties of multifarious stacking patterns for high-buckled and low-buckled silicene on the MoS_2 substrate,” *The Journal Physical Chemistry C* **118**, 19129 (2014). (IF = 4.484)
3. **L. Li**, and M. Zhao, “First-principles identifications of superstructures of germanene on Ag (111) surface and h-BN substrate,” *Physical Chemistry Chemical Physics* **15**, 16853 (2013). (IF = 3.906)
4. **L. Li**, X. Wang, X. Zhao, and M. Zhao, “Moiré superstructures of silicene on hexagonal boron nitride: a first-principles study,” *Physics Letters A* **377**, 2628 (2013). (IF = 1.863)
5. X. Zhao, **L. Li**, and M. Zhao, “Lattice match and lattice mismatch models of graphene on hexagonal boron nitride from first principles (Cover Article),” *Journal Physics: Condensed Matter* **26**, 095002 (2014). (IF = 2.617)
6. X. Chen, **L. Li**, and M. Zhao, “Dumbbell stanane: a large-gap quantum spin Hall insulator,” *Physical Chemistry Chemical Physics* **17**, 16624 (2015). (IF = 3.906)
7. X. Chen, **L. Li**, and M. Zhao, “Hydrogenation-induced large-gap quantum-spin-Hall insulator states in a germanium–tin dumbbell structure,” *Rsc Advances* **5**, 72462 (2015). (IF = 2.936)
8. A. Wang, **L. Li**, X. Wang, H. Bu, and M. Zhao, “Graphyne-based carbon

- allotropes with tunable properties: From Dirac fermion to semiconductor,” *Diamond and Related Materials* **41**, 65 (2014). (IF = 2.232)
9. M. Zhao, X. Chen, **L. Li**, and X. Zhang, “Driving a GaAs film to a large-gap topological insulator by tensile strain,” *Scientific Reports* **5**, 8441 (2015). (IF = 4.122)
 10. M. Zhao, X. Zhang, and **L. Li**, “Strain-driven band inversion and topological aspects in Antimonene,” *Scientific Reports* **5**, 16108 (2015). (IF = 4.122)

Conferences and Schools

- MAJORANA STATES IN CONDENSED MATTER: TOWARDS TOPOLOGICAL QUANTUM COMPUTATION
Spain, 14-20 May 2017, Poster
- BPS (Belgian Physical Society) 2018
Belgium, 11 April 2018, Poster
- Materials 4.0 - the digitally enabled atom to system revolution
German, 11-15 September 2017, Poster

Language

- English
- Chinese (Native)

Please note: “IF” is impact factor (release date: June 2018).